2009

Spectroscopic investigation of palladium-copper bimetallic systems for PEM fuel cell catalysts

Timo Hofmann
University of Nevada Las Vegas

Follow this and additional works at: https://digitalscholarship.unlv.edu/thesesdissertations

Part of the Metallurgy Commons, Nanoscience and Nanotechnology Commons, Physical Chemistry Commons, and the Power and Energy Commons

SPECTROSCOPIC INVESTIGATION OF Pd-Cu BIMETALLIC SYSTEMS FOR PEM

FUEL CELL CATALYSTS

by

Timo Hofmann

Diplom-Ingenieur Nanostrukturtechnik
Universität Würzburg, Würzburg, Germany
2005

A dissertation submitted in partial fulfillment
of the requirements for the

Doctor of Philosophy Degree in Chemistry
Department of Chemistry
College of Sciences

Graduate College
University of Nevada, Las Vegas
December 2009

THE GRADUATE COLLEGE

We recommend that the dissertation prepared under our supervision by

Timo Hofmann

entitled

Spectroscopic Investigation of Pd-Cu Bimetallic Systems for PEM Fuel Cell Catalysts

be accepted in partial fulfillment of the requirements for the degree of

Doctor of Philosophy
Chemistry

Clemens Heske, Committee Chair

Dennis Lindle, Committee Member

Dong-Chan Lee, Committee Member

Adam Simon, Graduate Faculty Representative

Ronald Smith, Ph. D., Vice President for Research and Graduate Studies
and Dean of the Graduate College

December 2009

ii

ABSTRACT

**Spectroscopic Investigation of Pd-Cu Bimetallic
Systems for PEM Fuel Cell Catalysts**

by

Timo Hofmann

Dr. Clemens Heske, Examination Committee Chair
Professor of Materials Chemistry
University of Nevada, Las Vegas

One of the main barriers to commercialization of polymer electrolyte membrane fuel cells systems is cost, which is largely due to the need of platinum (Pt)-containing catalysts. In this thesis we investigate bimetallic systems consisting of a base metal (copper) and a noble metal (palladium) that, as an alloy on the nanoscale, mimic the electronic properties that make Pt desirable as a catalyst.

We present a detailed investigation of the electronic structure of carbon-supported Pd/Cu nanoparticle catalysts, model bilayer thin film systems, alloys, and various metal reference samples. We have investigated the valence band structure of the catalysts using a combination of X-ray photoelectron spectroscopy (XPS) and UV photoelectron spectroscopy (UPS). We have studied the approach of modifying the d-band structure by fabricating and characterizing bilayer thin film systems (Cu/Pd and Pd/Cu). Furthermore, we have investigated carbon-supported bimetallic nanoparticles, fabricated at Argonne National Lab by colloidal and impregnation techniques.

Our experiments show that it is important to consider the entire d-band structure for describing the electronic structure of the catalyst and demonstrate how the alloy formation leads to new spectral contributions to the valence band density of states (as

compared to simple superpositions of Cu and Pd contributions). Furthermore, our results shed light on the degradation processes of the catalysts under highly acidic conditions (as in the real fuel cell environment).

The results provide fundamental insights into the tailoring of the electronic structure of Pd/Cu bimetallic systems and help to develop approaches to improve the performance of Pd/Cu-based nanoparticle catalysts in polymer electrolyte membrane fuel cells.

TABLE OF CONTENTS

LIST OF FIGURES

viii

x

LIST OF TABLES

ACKNOWLEDGMENTS

I would like to express my sincere gratitude to everyone that contributed to the success of this dissertation. My special thanks goes to Prof. Clemens Heske, who has not only given me the opportunity to do my dissertation research in his group but has also been a great mentor to me. We have been continuously working together since 2003. His support and guidance have shaped me in many ways and helped me grow both professionally and personally. Thank you for everything you did for me!

The post-doc gang, Yufeng Zhang, Stefan Krause, Asanga Ranasinghe, and the "ex-post-docs" and dear collaboration partners Lothar Weinhardt and Marcus Bär have always been of great assistance and a helpful source for suggestions, council, and constructive criticism. Especially Yufeng has been a major support in reviewing the first draft of this thesis, discussing data, and emptying the dish-washer at home when I was too tired to do so. I have learned a lot from his easy-going nature which has helped me balance my German strive for overly perfection.

Many thanks also to all of our group members. Coming from 10(!) different countries and therefore cultural areas, we have learned a lot from each other and work together in unison. Sujitra, thank you for your relentless efforts to minimize the entropy in our lab and for offering alternatives to sausages and carne asada at the group BBQs. Thanks also go to Roberto, who has become a great supporter of Bavarian traditions. While working all night long at UNLV or the ALS, we have always found the time to have a little bit of fun and laughter that kept us motivated. Kyle, thank you for sharing your experiences in life and reigniting my passion for martial arts.

The mechanical work shop led by Amo Sanchez and James Norton and the electronic work shop led by Leonard Rezac in the UNLV Physics Department have completed many jobs essential for this thesis over the past few years.

I would like to thank my group of close friends in the US, Germany, and around the world for being genuine friends that always support my goals, that understand when school leaves little personal time, and for the great and fun times we have when hanging out.

My special gratitude goes to my family in Germany and surrogate family in Las Vegas whose love and support have always encouraged me on my way.

CHAPTER I

INTRODUCTION

The ever-increasing energy prices along with ecological concerns drive the demand

for environmentally friendly alternative energy sources. Among the candidates for

electrical power production, the Polymer Electrolyte Membrane Fuel Cell (PEMFC) is

often favored, because it operates at near-ambient temperature, exhibits high power

density, and promises the possibility of mass production [1, 2]. Despite their vast

capabilities, PEMFCs are to date mainly used within the framework of demonstration

programs [3], since cost is one of the main barriers to commercialization of fuel cell

systems. Typically, the membrane-electrode assembly constitutes approximately 84% of

the total fuel cell stack cost, with the anode and cathode contributing almost 50% [4]. The

high cost is largely due to the use of platinum (Pt)-containing catalysts. Significant

advances in reducing the platinum metal loading of both the anode and cathode have been

made in the past decade. However, any further substantial cost reductions will require the

replacement of platinum with a less expensive catalytic material. In the 2008 DOE

Hydrogen Program Review, Directed Technologies Inc. showed that "Pt loading is the

key cost driver at high production rates" and that a "non-Pt catalyst would be a

breakthrough" [5] in terms of cost reduction.

The search for non-Pt catalysts for PEMFCs motivates this research project, which is

part of the DOE Hydrogen Program with is led by the Argonne National Laboratory

(ANL, Dr. D. Myers), in collaboration with the California Institute of Technology

(Caltech), the Oak Ridge National Lab (ORNL), the Los Alamos National Lab (LANL),

and the University of Illinois Chicago (UIC). The carbon-supported bimetallic nanoparticles studied in this research project are fabricated by ANL using colloidal and impregnation techniques. At Caltech, computational studies of modeling systems are carried out.

This dissertation is focused on the determination of the electronic structure of metal reference samples, commercial alloy foils, model thin-film systems and nanoparticle catalysts. In particular, bimetallic systems consisting of a low-cost base metal (copper) and a noble metal (palladium) were studied. If base and noble metal are alloyed on the nanoscale, it might be possible to mimic the electronic properties that make Pt desirable as a catalyst. This approach has potential to fulfill the premises of high catalytic activity, long-term stability, and low cost, which are indispensable for a major breakthrough in commercializing PEMFCs.

The context of this dissertation is briefly outlined in Chapter II. The basic principles of the experimental techniques used in this dissertation are described in Chapter III. Influences on the spectral information obtained by photoelectron spectroscopy are reviewed in terms of their impact on the valence band structure of the studied samples. Furthermore, spectral analysis methods, the experimental setup, and sample preparation procedures are described.

In Chapter IV the experimentally determined valence band structures of the investigated metals Pd, Cu, and Pt as a reference are reviewed and compared to the theoretical DOS of the respective metals. Commercially available Pd-Cu alloy foils are investigated in Chapter V. The electronic structure of alloy foils is determined and correlated to the catalytic activity (measured by our collaborators at ANL). The results

are compared to pure metals. Furthermore, the potential of annealing to induce surface segregation in order to form a protective layer on the nanoparticle catalysts and enhance the stability of the catalysts in an acidic environment in PEMFCs is studied.

In Chapter VI, studies of Pd thin-films deposited on Cu and vice versa are reported. The evolution of the valence band structure of the thin-film systems at room temperature is investigated by photoelectron spectroscopy. Furthermore, insights into the alloying process of Pd and Cu are discussed. The valence band of the Pd-Cu thin-film systems is correlated to the one of metal references, superpositions thereof, and alloy foils.

Chapter VII focuses on the investigation of nanoparticle catalysts synthesized by ANL. An improved understanding of the electronic structures of the nanoparticles is achieved by comparing to the well defined systems presented in Chapters IV-VI. Furthermore, the stability of the nanoparticle catalysts in acid, which is crucial for long-term performance, is investigated. The experimental results of this dissertation are summarized in Chapter VIII and an outlook of future experiments is given.

CHAPTER II

LITERATURE REVIEW

In this chapter an overview of the status of PEMFC catalysts is given and the basic concepts and guidelines of the research presented in this dissertation are reviewed. Section 2-1 briefly reviews the history of catalysis and describes the working principle of PEMFCs. In Section 2-2 a brief history of PEMFCs is given and reviews of the past and current developments in the field of catalysts for the oxygen reduction reaction (ORR) are presented. The theoretical guidelines and implications for the current dissertation will be discussed in Section 2-3.

Section 2-1

History of Catalysis and the Proton Exchange Membrane Fuel Cell

Without most people taking notice, our daily lives are governed by the phenomenon of catalysis. One of the first to report about substances that influence the progress of a chemical reaction without being consumed was Wolfgang Döbereiner. In July 1823 he reported "that finely divided platinum powder caused hydrogen gas to react with oxygen by mere contact to water whereby the platinum itself is not altered" [6]. Within three months, Döbereiner's discovery had been published in about a dozen European scientific journals [7]. In 1835, Jöns Jacob Berzelius named the phenomenon "catalysis" [8] and in

1902 Wilhelm Ostwald proposed: " A catalyst is a substance which affects the rate of a chemical reaction without being part of its end products" [7, 9].

In a chemical reaction, bonds between atoms are created and broken. This involves transformation of energy as depicted for the reaction of X + Y → Z in Fig. 2.1. The activation energy E_a is usually supplied by the thermal energy kT, where k is the Boltzmann constant and T is the temperature in Kelvin. In the presence of a catalyst the activation energy is lowered, which leads to an increase in the reaction rate. For the catalyst to take effect, it has to engage with the reaction. As indicated by the meandering red curve, the catalyzed reaction takes a different reaction pathway compared to the uncatalyzed reaction. Along the way, the catalyst forms intermediate compounds with the starting materials and is restored at the end.
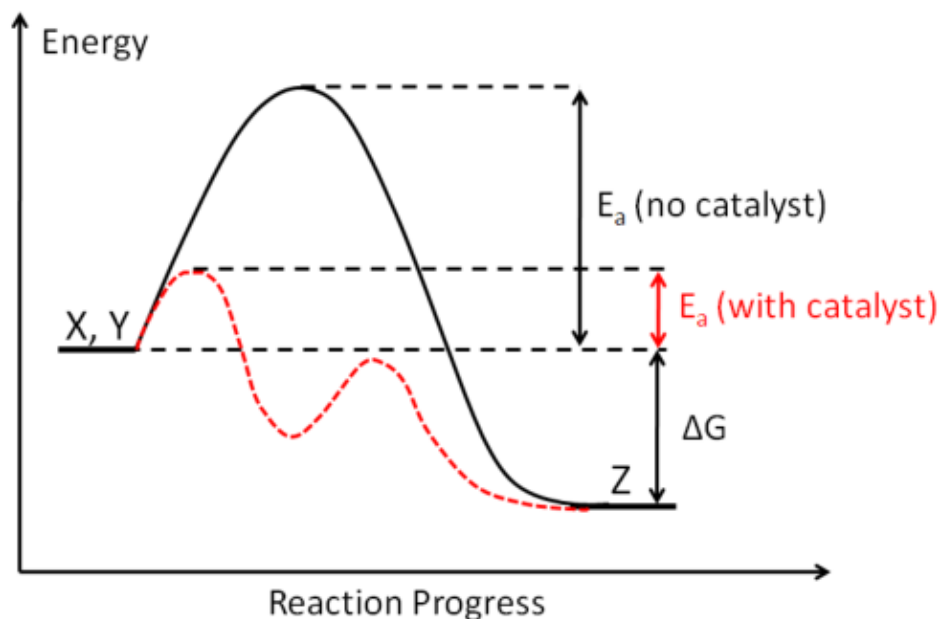
Fig. 2.1: Energy diagram of a chemical reaction between X and Y with and without a catalyst (adapted from [10]).

If the catalyst is in the same phase as the reactants, the effect is called homogeneous catalysis, whereas if catalyst and reactants are in different phases, the process is called

heterogeneous catalysis [10]. This is the case for all catalytic processes in a PEMFC, where the catalysts are in the solid phase while the reactants are gaseous. The PEMFC was developed in the early 1960th at General Electric by Willard Thomas Grubb and Lee Niedrach [11]. It was the first fuel cell technology known to be used operationally – as the onboard electrical power source for NASA's Gemini space flights in 1963-1965 [12, 13]. The main advantages of PEMFCs include the ability to operate at near ambient temperatures (50-100˚C) and high power densities, as well as the possibility of mass production [14]. Possible applications range from small mobile devices to large stationary installations. In Fig. 2.2 the basic layout of a PEMFC is shown. Hydrogen gas and oxygen from ambient air are delivered to the anode and cathode, respectively.

At the anode, hydrogen gas is split into protons and electrons by a platinum (Pt) catalyst: $H_2 \rightarrow 2H^+ + 2e^-$. The protons permeate through the PEM (typically, Nafion is used), while the electrons travel along an external circuit and can be used to perform electrical work. On the cathode side, the protons react with oxygen and the electrons from the external circuit to form water in the so-called oxygen reduction reaction (ORR):

$$4H^+ + 4e^- + O_2 \rightarrow 2\ H_2O\ [1, 2].$$
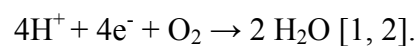
Despite their vast capabilities, PEMFCs are mainly used within the framework of demonstration programs [3]. Besides the low catalytic efficiency of the ORR on the cathode, cost is currently the main barrier to commercialization of PEMFCs. Typically, the membrane-electrode assembly constitutes approximately 84% of the total fuel cell stack cost, with the anode and cathode contributing almost 50% [4]. The high cost is largely due to the use of platinum (Pt)-containing catalysts.
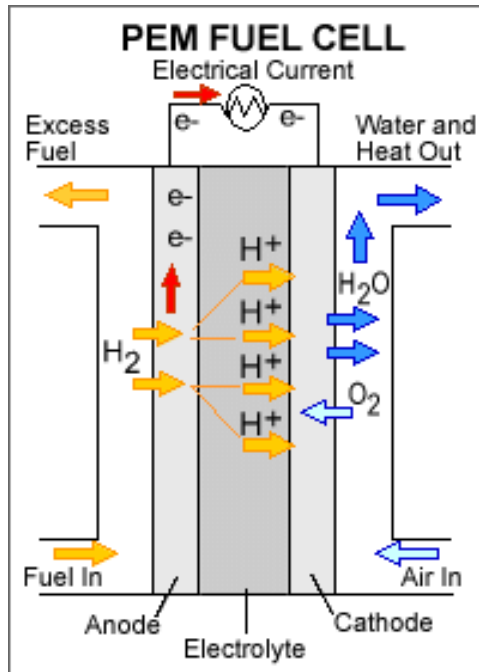
Fig. 2.2: Diagram of a polymer electrolyte membrane fuel cell (taken from [15]).

Pt and Pt alloys are the best catalysts, to date, for both hydrogen oxidation, taking place at the anode of the PEMFC, and the reduction of oxygen on the cathode. The overpotential associated with the latter reaction is considerably higher than for the former one [14]. Costamagna and Srinivasan specify the overpotential at the hydrogen electrode to be about 20 mV and the one on the oxygen electrode to be about 400 mV for a PEMFC operating at current densities of 1 A cm^{-2} [13]. Thus, research efforts have mainly been focusing on improving the cathode catalyst that is responsible for the ORR.

Section 2-2

Catalysts for PEMFCs

Unsupported high-surface area platinum powder (4 mg cm^{-2}) was used in the first cells as the cathode catalyst [13, 16]. Due to the high cost (high catalyst loading) and the

instability of the polystyrene sulfonate ion exchange membrane (used in the cells at that time) under the electrochemical environments, the alkaline fuel cell was chosen over the PEMFC for the later Apollo program and space shuttle missions [16]. Research on PEMFCs, however, continued. Unsupported Pt particles were still used as catalysts, which resulted in high noble metal loading (4 mg cm^{-2}) [16]. The first breakthrough in the field of catalysts was the 10-fold reduction of Pt loading (from 4 mg cm^{-2} to about 0.4 mg cm^{-2}) in 1986 by using Pt supported on high surface area carbon (e.g., Vulcan XC72R) [13, 16, 17]. The reduction was possible because carbon supported catalysts exhibit a much higher surface area (particle size about 30 Å) compared to the previously used unsupported Pt catalysts (particle size about 100-200 Å) [13]. Additionally, the three-dimensional zone in the electrolyte is extended by impregnation of the electrolyte membrane, so that the utilization of the electrocatalyst becomes comparable to that in a fuel cell with a liquid proton conductor (e.g. phosphoric acid) [13]. In the mid/late 1990s the Pt loading was reduced even further. Loadings of 0.1 mg cm^{-2} were realized by deposition of thin Pt films on an uncatalyzed electrode or on the electrolyte [13, 18, 19]. At present, typical platinum group metal (PGM) catalyst loadings are on the order of 0.2-0.35 mg cm^{-2} [5]. The most active ORR catalyst thus far is Pt_3Co with a surface-segregated Pt skin [20]. In the following sections, the approach to quantify the ORR activity will be reviewed, along with the theoretical studies that guided this research.

Section 2-3

ORR Activity, Theory of d-Band Center, and Surface Segregation

The kinetics of the ORR, as described in Section 2-1, can be described by the following equation [21]:

$$i = nFKc_{O_2}(1 - \Theta_{ad})^x \exp\left(-\frac{\beta FE}{RT}\right)\exp\left(-\frac{\Delta G_\Theta^*}{RT}\right) \qquad (1)$$

where Θ_{ad} is the coverage and ΔG_Θ^* is the adsorption energy of the reaction intermediates O_2^- or OH. In the case of positive adsorption energies, the reaction kinetics are governed by the ΔG_Θ^* term, while the coverage term becomes significant at negative adsorption energies. Overall, the ORR kinetics exhibit a volcano-shaped dependence on the free energy ΔG of formation of the intermediates as displayed in Fig. 2.3.
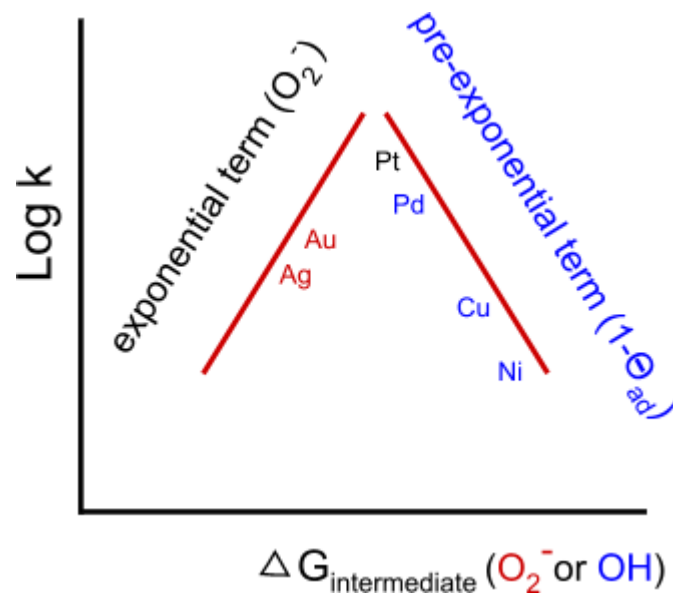
Fig. 2.3: Volcano-shaped dependence of ORR kinetics on the free energy of formation of the intermediate species, adapted from [21].

The observed trends in the ORR rate of transition metals are explained in literature by the impact of the metal's d-band center (i.e. the average energy of the d-states) on the

adsorption energy of the intermediate. The theoretical work by Nørskov and Hammer attempts to correlate the electronic configuration of the catalyst to the strength of the bond formed with oxygen [22]. They find that the d-band center at higher binding energies causes O_2 to bind less strongly to the metal surface. For instance, the d-band center of gold (Au) is situated at higher binding energies as compared to platinum (Pt), which decreases the overlap of Au d orbitals with the oxygen p orbitals, and therefore leads to lower ORR kinetics and a positive value for ΔG_Θ.

As mentioned earlier, platinum-cobalt (Pt-Co) is currently the most active catalyst for the ORR [23]. As can be seen from its position in Fig. 2.3, Pt binds oxygen slightly too strong. According to the Hammer-Nørskov theory, the addition of Co causes the d-band center of Pt to shift to higher binding energy [24], leading to a decrease in the strength of its bond with the ORR intermediates.

The above mentioned theoretical studies inspired the program lead at ANL (Dr. D. Myers) to develop non-Pt-based bimetallic catalysts with ORR activities comparable to that of Pt-Co, but with a significantly lower cost. The main idea is to modify the d-band center of the less-costly noble metal (e.g., Pd) and to alloy it with a base metal (e.g., Cu) to make the resulting bimetallic system "Pt-like" in terms of its electronic structure and bonding characteristics relevant to the ORR. In addition to the challenge of mimicking Pt, the bimetallic system has to be stable in the highly acidic PEMFC environment. Among the catalytically active metals that possess the highest stability in acid are the noble metals: rhodium, platinum, palladium, iridium, and gold [25]. Of these, Pt exhibits the highest activity for the ORR, with Pd coming in second [26]. As discussed earlier, the electronic properties of metals can possibly be tailored by alloying them with metals that

shift their d-band centers. For metals on the rising edge of the volcano curve (see Fig. 2.3) that bind intermediates too weakly, the model predicts that the d-band center needs to be shifted to higher binding energies, for metals on the falling edge that bind intermediates too strongly a shift to lower binding energies is expected to be beneficial to improve their ORR activity. Nørskov et al. calculated the expected shift in the d-band center of an "impurity" metal on the surface of a bulk comprised of another metal using density functional theory (DFT) [27]. The guidance provided by these calculations was used to pick those metals that are likely to provoke the necessary shift of the d-band center of the alloyed noble metal to become more Pt-like.

Furthermore the bimetallic systems need to be chosen in such a way that stability in acid is ensured. Although the formation of an alloy partially stabilizes the non-noble metal in a noble metal-base metal alloy, the base metal is expected to be removed over time, due to the acidic fuel cell environment. Hence, it is desirable to only expose the stable noble metal to the acidic environment. The ideal structure is thus one where the noble metal forms a protective skin on the surface of the alloy particle. Surface segregation energies calculated by Ruban et al. [28] were consulted for the choice of noble metal-base metal combinations that showed a propensity of the noble metal in the alloy to segregate to the surface of the bulk alloy.

The desired d-band center of the non-platinum electrocatalysts was modeled after the d-band center of Pt_3Co, which has the highest ORR activity. The Pt d-band center is calculated to be at 2.25 eV [22]. For Pt_3Co with a Pt skin the d-band center is shifted down by 0.36 eV, resulting in a predicted d-band center at 2.6 eV [21]. This concept was used as a guide for choosing the base metals to be alloyed with the catalytically-active

noble metals palladium, rhodium, and iridium. Using the surface segregation energy calculations in [28] and the calculated shifts in the d-band center in [27], the Pd-Cu systems appear to be the most promising with a theoretical d-band center of 2.9 eV, i.e., in the vicinity of the one found for Pt_3Co.

An experimental study of the Pt_3M system (with M = Ti, V, Cr, Fe, Co, Ni) by Mun et al. [24] using UV photoemission spectroscopy shows qualitatively the same trend for d-band centers and widths of annealed alloy surfaces as predicted by density functional theory. However, as will be discussed in Chapter IV, the d-band center is a poorly defined quantity in a UV photoemission spectrum, and a direct correlation with actual ORR activities is rather challenging (and not attempted in [24]).

EXPERIMENTAL DETAILS AND CONSIDERATIONS

The experimental techniques employed in this dissertation are discussed and the instrumental setup is described in Section 3-1. To extract information from the measured spectra, many factors need to be considered. The evaluation approach to derive spectral information in this dissertation will be outlined in Section 3-2. Data analysis methods used in this dissertation are briefly outlined in Section 3-3, and details of sample preparation and measurements are given in Section 3-4.

Section 3-1

Techniques and Instrumentation

The experiments conducted within this dissertation use photoelectron spectroscopy (PES) to characterize the electronic structure and the chemical environment of samples. The results from PES are complemented by information on the sample morphology (e.g., size of nanoparticles), measured by atomic force microscopy (AFM) at UNLV and transmission electron microscopy at ORNL. Furthermore, the oxygen reduction reaction (ORR) activity of samples and their crystal structure was determined at Argonne National Lab (ANL) by electrochemical characterization methods [rotating disk electrode (RDE), cyclic voltammetry (CV)], and x-ray diffraction (XRD), respectively. A discussion of PES will be given in this Section. For more detailed information on the subject refer to the books of Hüfner [29] and Briggs and Seah [30]. Additionally, a short description of

the techniques listed above is given to provide a basic understanding of the methods, their information value for this dissertation, as well as their limitations.

3-1.1. Photoelectron Spectroscopy

PES is a powerful tool to extract elemental and chemical information from surfaces and interfaces of a large variety of materials. By irradiating the surface with photons in the x-ray or ultraviolet regime, electrons from the sample surface and surface-near layers can be freed by the photoelectric effect. The intensity of these so-called photoelectrons (photocurrent) is then measured in reference to their kinetic energy. The photocurrent produced in this way can be regarded as an excitation of electrons in an initial state $|\Psi_i>$ to a final state $< \Psi_f|$ by the effect of the incident photon field. The transition probability $w_{i\rightarrow f}$ between the two states can (in dipole approximation) be described by Fermi's Golden rule:

$$w_{i\rightarrow f} \propto \left|\langle\psi_f|r|\psi_i\rangle\right|^2\delta(E_f - E_i - h\upsilon) \qquad (1)$$

The delta function in Eq. (1) ensures the energy conservation of the overall process. The binding energy E_{bin} can be calculated from the kinetic energy E_{kin} of the photoelectrons and the photon energy $h\upsilon$, according to the following expression:

$$E_{bin} = h\upsilon - E_{kin} \qquad (2)$$

Another important aspect of Eq. (1) is that the photoemission process depends on both the initial $|\Psi_i>$ and final state $< \Psi_f|$. Thus, not only the initial density of states but also the final density of states needs to be considered in PES. As a consequence, PES becomes dependant on final state effects, such as "incomplete" sampling (averaging) of the band structure over the entire Brillouin zone when using small photon energies as in the case of ultraviolet photoelectron spectroscopy (UPS), or incomplete screening of the photo-

excited core-hole. Their impact on valence band spectra recorded by x-ray photoelectron spectroscopy (XPS) and UPS will be discussed in Section 3-2. The overall transition probability in Eq. (1) depends on the transition matrix element, which is directly related to the photoionization cross-section of the electrons and associated with the overlap of initial and final state wave functions. The cross-section depends on the particular element and atomic level [31, 32] and needs to be taken into account for quantitative analysis (as discussed in Chapter IV).

For XPS, Mg K_α ($hv = 1,253.6$ eV) was used as excitation source for results reported in Chapter IV, Section 4.1, and spectra were recorded using a SPECS PHOIBOS 150MCD electron spectrometer in the "Andere ESCA" system at UNLV. All other XPS spectra of this dissertation were recorded using a monochromatized x-ray source producing Al K_α radiation ($hv = 1,486.6$ eV) and recorded using a Scienta R4000 electron spectrometer in the "Scienta" system at UNLV. UPS experiments were also conducted in the "Andere ESCA", using a He gas discharge lamp, which produces He I ($hv = 21.2$ eV) and He II ($hv = 40.8$ eV) ultraviolet radiation. The low-energy photons used in UPS exhibit a larger cross-section for valence levels than high-energy photons applied in XPS. However, XPS is far less susceptible to final state dispersion effects, as will be discussed in Section 3-2.

3-1.2. Atomic Force Microscopy (AFM)

The main principle of AFM is based on the interaction between a physical nanoscale probe (tip on a cantilever) and the sample surface. The sample surface is mechanically scanned by the probe in a line-by-line fashion, recording the atomic-scale force that is exerted on the tip. Through this procedure, a morphological image of the sample surface

with a resolution on the nanoscale can be obtained. Detailed information on AFM and scanning probe microscopy can be found in the books of Birdi [33] and Meyer et al. [34]. The image shown in this dissertation was recorded by Dr. Asanga Ranasinghe in a Park Systems XE-70 scanning probe microscope at UNLV.

3-1.3. Cyclic Voltammetry (CV)

In CV, the potential of an electrode, which is immersed in an unstirred solution, is cycled and the resulting current is measured. Through potential cycling, CV provides the possibility to generate a new oxidation state during the forward scan and then probing its reduction on the reverse scan [35]. The current is the response signal to the potential excitation signal and is directly related to the amount of electrons transferred in the electrode reaction. The current in CV is normalized to the diffusion-limited region in which there is no potential dependence for the current [14]. When plotting the observed current over the applied voltage, the potential at which the current reaches half of its peak value $E_{p/2}$ (half wave potential) provides a qualitative measure of the ORR activity of the foils [14]: the higher the value of $E_{p/2}$, the higher the activity for the ORR [14]. All CV data shown and discussed in this dissertation was taken by our project partners at ANL.

3-1.4. Rotating Ring Disk Electrode (RRDE)

The thin-film rotating ring disk electrode (RRDE) technique has been used by ANL to measure the ORR activity of catalysts reported in Chapter VII. If performed using the correct geometry and electrode thicknesses, kinetic data obtained using the RRDE technique can be directly translated to the performance of the catalyst in a PEMFC [2, 36]. This technique allows the determination of the reaction kinetic parameters (exchange current density and transfer coefficient), independent of mass-transfer effects at the disk

electrode, and detection of the presence of reaction intermediates (e.g., H_2O_2) at the ring electrode [2]. The current measured at 0.8 V, using the RRDE technique, when normalized to the catalyst weight (mass activity) or active surface area (area activity), is used to compare the activity of the catalysts investigated in Chapter VII. A detailed discussion of the RRDE technique can be found in [2].

3-1.5. Calculations using Density Functional Theory (DFT)

The theoretical density of state (DOS) for various metals and alloys was calculated by our collaborators at Caltech using the SeqQuest software, a general-purpose electronic structure code developed by the Sandia National Lab. For the DFT calculations, a Gaussian basis set, the Perdew-Burke-Ernzerhof (PBE) generalized gradient approximation, and periodic boundary conditions (modeling the electron wave functions as plane waves) were used.

Section 3-2

Evaluating the Spectral Information

PES spectra and their information content are influenced by many factors, such as the inelastic mean free path (IMFP) of the emitted photoelectrons, the photoionization cross section σ, final state effects, and many more. The influences of those factors relevant to the discussion of the electronic structures presented in this dissertation will be outlined in the following.

3-2.1 Influence of the Excitation Energy

In this section, the influence of the excitation energy on the valence band structure (VBS) will be discussed exemplarily for the VBS of polycrystalline copper. In a typical

lab-based environment, as in the case at UNLV, the experiment is restricted to a limited number of excitation energies. The here presented data was recorded using the following excitation sources: He I (21.2 eV), He II (40.8 eV), Mg K_α (1,253.6 eV), and Al K_α (1,486.6 eV). Fig 3.1 shows the VBS of a polycrystalline Cu foil. For the discussion, the range of excitation energies available at UNLV was extended using data from a PES study by D. A. Shirley et al., where synchrotron radiation was used as the excitation source [37]. The spectra on the top and the bottom were measured for a sputter-cleaned Cu foil at UNLV using Al K_α and He I radiation, respectively.
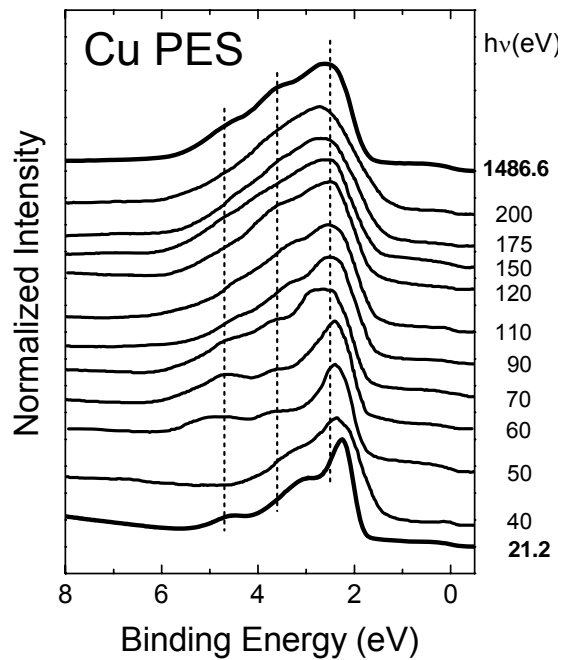
Fig 3.1: Valence band structure of polycrystalline copper as a function of excitation energy. The top and bottom spectra were measured by UPS and XPS, all other spectra were taken from reference [37].

All other spectra [37] were taken from Cu evaporated in-situ on a stainless-steel substrate. In both cases, the Cu samples are of polycrystalline nature. The VBS clearly

changes with the excitation energy. This finding entails the question of which excitation energy is the most appropriate to study the electronic structure of catalysts, in particular to quantify the d-band center position.

In order to answer this important question, the spectral information obtained from UPS and XPS will be reviewed and the "excitation energy gap" between the two photon sources will be filled by the interpretations gained from the synchrotron study of Shirley et al.

In the UPS regime (photon energies smaller than 100 eV) the VBS is often discussed in terms of final-state effects which are responsible for the observed line positions and intensities determined by transition-matrix-element modulations [38]. Due to the relatively low excitation energy in this regime, transitions can only occur at special $\vec{k}$ points of the Brillouin zone (BZ), i.e., only if a suitable final state for the excited electron can be found (note that the photon does not contribute a significant amount of momentum, so that the transition has to be vertical in k-space). This dominance of direct transitions can be exploited to map the band structure experimentally when using angle-resolved PES (ARPES).

As discussed, it is generally thought that the ORR activity of a transition metal catalyst can be linked to its d band [22, 27]. Therefore, it is important to obtain the "true" initial DOS of the metal. As is evident from Fig. 3.1, variations as a function of excitation energy affect both the line positions (indicated by the dashed vertical lines for the 1486.6 eV spectrum) as well as the peak intensities.. The latter vary significantly with excitation energy because of both the angular and radial parts of the transition matrix element [39]. This makes it challenging to obtain information about the initial DOS from such spectra.

Hence, the unique and powerful property of selectivity in crystal momentum of PES measurements performed at photon energies below ~100 eV is not favorable for the studies in this dissertation.

In the case of XPS (photon energies of 1253.6 eV or 1486.6 eV), the kinetic energy and thus momentum of the photoelectrons is so large that the experiment probes the entire BZ in the final state, since transitions can no longer be regarded as vertical in $\vec{k}$ space [29]. Therefore, XPS is generally acknowledged to be a superior probe for the *initial* DOS [37, 39, 40]. Therefore, it is the better option for the studies performed in this dissertation. It is important to note that other influences, like the electron escape depths, energy-loss mechanism, and surface-state phenomena, also affect the VBS.

As shown by the synchrotron-based PES study of Cu by Shirley et al. in Fig 3.1, the VBS varies for excitation energies as high as 175 and 200 eV. Apparently, a photon energy of well above 200 eV is needed for the VBS to approach the XPS VBS, i.e., for a "quasi-continuum" of final states to exist such that all initial states can be excited and other final state effects are minimized.

Besides these "band-structure-type" cross-section effects, Shirley et al. discovered "atomic-type" cross-section effects in silver (Ag) [37, 41]. They found a sharp decrease in intensity for the Ag 4d spectral intensity in the range $100 < h\nu < 140$ eV with a minimum at 140 eV that leads to inversion of the relative heights of the two prominent VB peaks in that region. They linked the observed minimum to "Cooper minima" that had been postulated by Cooper and Fano for initial-state wave functions with a radial node [42, 43]. In such a case the cross-section can vary largely over a small energy range. Wehner, Shirley, et al. point out that "if our spectra had been taken with photon energies

extending only up to 90 eV, the reversal of intensities would have been overlooked; if to 110 eV, an incorrect density of state might have been inferred" [41]. They conclude that similar behavior may be expected in other 4d-group and 5d-group elements (such as the here investigated Pd) and that PES studies of 4d-group elements need to be carried to the $h\nu > 150$ eV range.

In conclusion, VBSs recorded below the XPS "limit" sensitively depend on both the initial state (valence band) and final state (conduction band) energies and wave functions. For elements that exhibit radial nodes, the VBS can change greatly due to fluctuations in the photoionization cross-section. Thus, an investigation using XPS, albeit involving an excitation, is the closest approximation to the initial DOS and was hence favored for the determination of VBSs in this dissertation.

3-2.1 Influence of Cross-Sections

The atomic cross-sections in the XPS and UPS regime are generally very different. This can be easily seen in Fig. 3.2, which shows the atomic photoionization cross-sections σ for the valence levels of Pt, Pd, and Cu, as determined by Yeh and Lindau [44]. The cross-section is significantly larger for UPS as compared to XPS. However, the value in the UPS region also varies more strongly between Pt, Pd, and Cu as compared to XPS. In either case, this variation needs to be taken into account when establishing the respective contribution to the VB of one metal versus another, as performed in Chapters V, VI, and VII. Furthermore, UPS exhibits a large cross section for small molecules [45] like carbon monoxide, which, when adsorbed on the surface, can strongly influence the VBS, as will be discussed in Chapter IV.
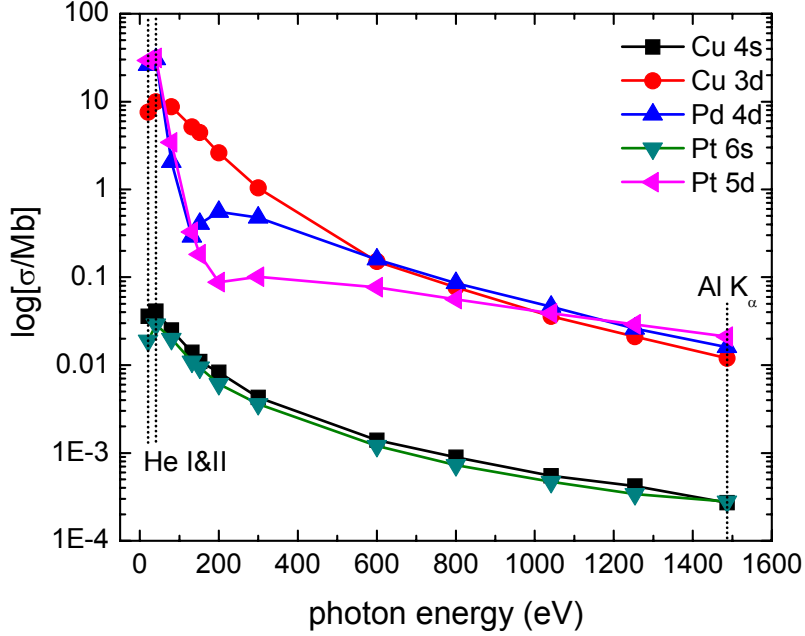
Fig. 3.2: Atomic photoionization cross-section σ of the Pt, Pd, and Cu valence levels as a function of photon energy.

3-2.1 Inelastic Mean Free Path of Electrons

Electrons have a finite length in matter that they can travel without being inelastically scattered. In a PES spectrum, only those electrons contribute to the peak structure that have not suffered an inelastic scattering process on their way to the surface. Electrons that encounter a random inelastic scattering process thus contribute to the background of a spectrum. The inelastic mean free path λ of electrons can be estimated by the so-called universal curve displayed in Fig. 3.3 [30]. While still commonly in use, a better quantitative description is found using the Quases-IMFP-TPP2M software based on a formula by Tanuma, Powell, and Penn [34]. For kinetic energies above 50 eV, λ is roughly proportional to $\sqrt{E_{kin}}$, while below 50 eV, λ is roughly proportional to E^{-2}. In general, the value of λ also depends on the specific material under investigation as indicated by the spread of the data points in Fig. 3.3. The inserted markers indicate the

IMFPs of electrons from a state with a binding energy of 5 eV, photo-emitted with different excitation energies (UPS, XPS, and soft x-ray synchrotron). From the intersection with the y-axis, it can be seen that the IMFP is on the order of 5 monolayers (~1 nm) for VBs measured by UPS and about 10 monolayers (approx. 2 nm) for the Al K_α source used for our XPS spectra. Thus, a variation of excitation energy also corresponds to a variation of probing depth. In the case of XPS, for example, a more "bulk-like" spectrum is obtained, reducing the spectral contributions of surface contaminants compared to the UPS or soft x-ray synchrotron case.
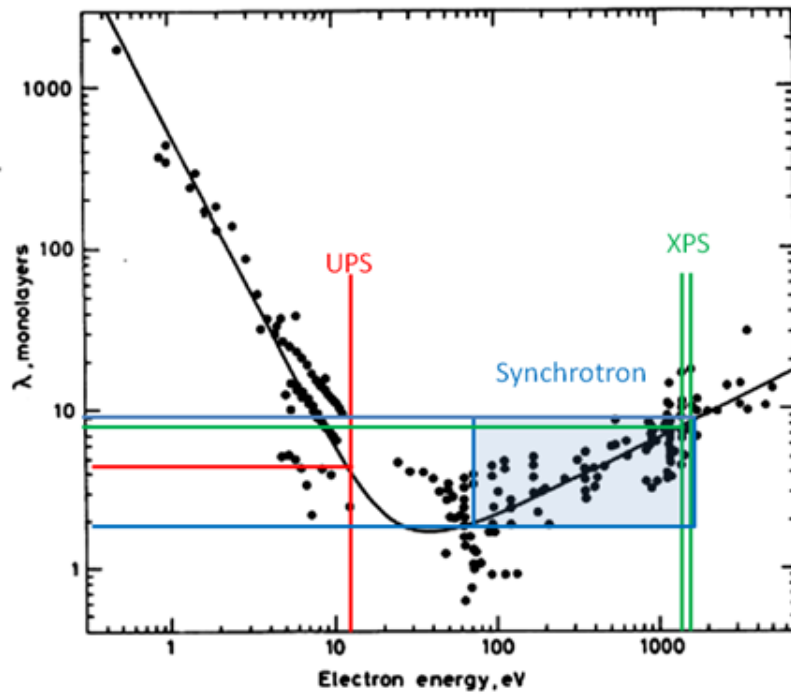
Fig. 3.3: Inelastic mean free path of electrons in matter (adapted from [30]).

The value of λ determines the attenuation of the photoelectron intensity as a function of depth. Statistically speaking, the number of electrons retaining their original kinetic

energy is reduced to 1/e of its original number (via inelastic scattering) after travelling the distance of the IMFP. More quantitatively, the intensity is given by $I_0 \cdot \exp(-d/\lambda)$, d being the distance that the electrons travel and I_0 being the initial intensity (number of electrons). For the overall photoemission intensity, one has to integrate over this formula as a function of depth (d).

Section 3-3

Spectroscopic Data Analysis Methods

This section describes the techniques used to analyze photoemission spectra in order to extract information about the electronic structure of the sample surface, the formation of thin-film layers, and the background due to inelastically scattered electrons.

In a typical XPS investigation, a survey spectrum, covering a wide energy range (e.g., 100-1500 eV kinetic energy) with a relatively large step size (e.g., 0.5 eV) and pass energy (e.g., 200 eV for the Scienta R4000 analyzer), is measured first. All detectable elements in the survey spectrum are identified by their binding energy position. Subsequently, a high resolution spectrum (detail spectrum) of each region of interest is measured. This provides information on the chemical and electronic structure of specific elements and a basis to perform a quantitative analysis. Integration, peak-fitting procedures, and difference-spectra techniques are employed for quantitative analysis of the detail spectra.

3-3.1. Compositional Analysis

The intensity I of a core level line depends on various parameters. First of all it is a function of the probability for a photoemission process, as described in Eq. (1). The

intensity is therefore proportional to $\sum_f |\langle \Psi_f | r | \Psi_i \rangle|$, which is proportional to the photoionization cross-section σ(Z,a,hν). The photoionization cross-section in turn depends on the element (nuclear charge) Z, the initial and final state (designated as the photoemission line a) and the excitation energy hν. Besides electrons from the topmost atomic layer, unscattered electrons stemming from deeper layers are also detected. Their intensities are attenuated according to their IMFP $\lambda(E_{kin})$ (see 3-2.1). For sufficiently thick samples (thickness >> 10 nm), the line intensity is directly proportional to $\lambda(E_{kin})$. I is further a function of the transmission function of the analyzer $T(E_{kin})$, which changes with kinetic energy of the electrons. Finally, I is proportional to the concentration distribution of the element. In summary, the intensity of a photoemission line from a sufficiently thick sample is proportional to:

$$I \propto \sigma(Z, a, h\nu) \cdot c(Z) \cdot \lambda(E_{kin}) \cdot T(E_{kin}) \quad (3)$$

Concentration quantification can therefore be performed by integrating the area of a characteristic line and normalizing to σ(Z,a,hν), $\lambda(E_{kin})$, and $T(E_{kin})$. For all compositional analysis within this dissertation, the tabulated values of σ(Z,a,hν) in [33] were used. The IMFP was approximated by $\lambda \propto \sqrt{E_{kin}}$ (see 3-2.1) for all quantitative analyses performed in this dissertation. This approximation constitutes a very rough approximation due to the wide spread of data points in Fig.3.3. Thus, *absolute* concentrations determined with XPS are rather imprecise, while *relative* changes can be monitored very precisely.

The transmission function of the Scienta R4000 analyzer used in this dissertation was determined by alignment to a reference spectrum, for which the transmission function of the analyzer was corrected in a detailed procedure [46]. Fig. 3.4 shows our measured Au

spectrum (thin line), adjusted to fit the background shape of the transmission-corrected Au reference spectrum in [46]. As can be seen, the adjusted spectrum fits well with the reference over most of the energy range. The transmission function of the R4000 analyzer was determined to $T(E_{kin}) = -0.16592 - 0.1657 \cdot \log(E_{kin})$. In this dissertation, the above-described procedures were used in all quantitative analyses to estimate the elemental concentration.
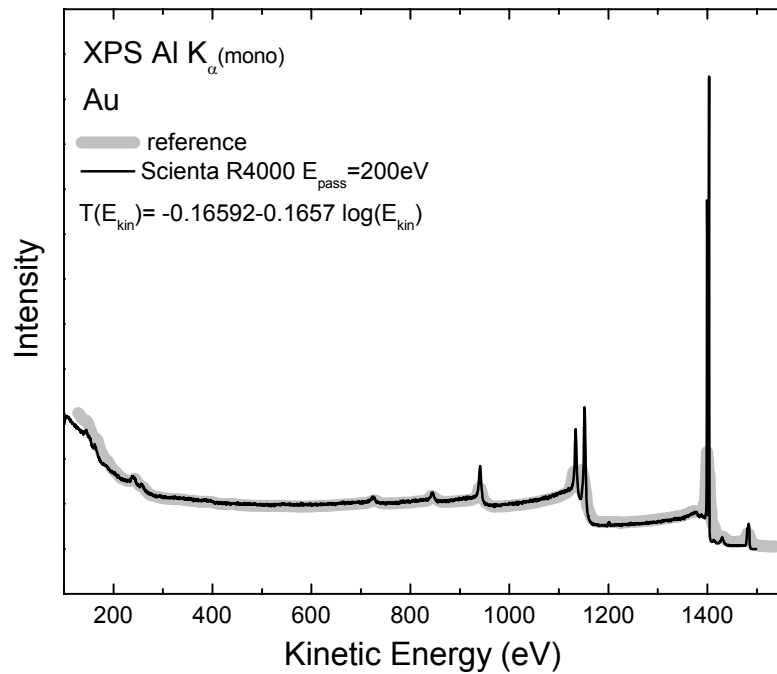
Fig. 3.4: Gold reference spectra from [46] and adjusted Au spectrum of the R4000 analyzer used in this dissertation.

3-3.2. Deposition Thickness Analysis

The deposition of thin films (as studied in Chapter VI) on the surface of substrates leads to attenuation of the PES signals from the substrate.

When a uniformly deposited film is formed on the sample surface, its thickness can be estimated from the attenuation of the substrate signal, following [29, 30]:

$$I = I_0 \exp(-\frac{d}{\lambda}), \quad (4)$$

where I_0 and I is the intensity of the substrate signal before and after deposition, respectively, λ is the inelastic mean-free path (IMFP) of the photoelectron, and d is the thickness of the deposited overlayer. As mentioned above, the λ value is best calculated using the QUASES-IMFP-TPP2M software, which uses the Tanuma, Powell, and Penn formula reported in [32]. For nonuniform films, e.g., in the case of island formation, this procedure derives an average (effective) film thickness.

3-3.3. Background Subtraction

The accurate removal of the background contribution to a PES spectrum requires great care since, if not done properly. it may distort the spectral information significantly. Thus, a detailed knowledge of the origin of the photoemission background, in particular of the mechanisms of inelastic scattering processes, is required. Due to this complexity, background subtraction was only carried out where required, and the procedure used is clearly indicated throughout this dissertation. Three types of background have been used. The first is a linear background, the second an integral background based on the Shirley method [47], and the third is the background of the carbon support used for the nanoparticle catalysts reported of in Chapter VII.

For integration of peaks, the linear background was removed by drawing a straight line between the first and last few points in a spectrum and subtracting the line intensity from the spectrum. This method was consistently used to subtract the background from detail spectra used for quantitative analysis. In general, a linear background should be

used to describe materials with a band gap, i.e., those where infinitesimal energy losses due to excitation of electrons just across the Fermi energy are not possible. In a peak fit, the linear background parameters need to be included as fit parameters.

The Shirley background is a non-linear background that takes into account the background step found mostly in metals spectra, mainly stemming from inelastically scattered electrons. Since the method is approximative [48] and, strictly speaking, only valid for pure metals it was only used to remove the background for the calculation of the d-band centers reported in Chapter IV.

Lastly, for some of the VB spectra reported in Chapter VII, the background of the carbon support, which was determined by measuring the support in the as-received state (i.e., without metal nanocatalysts), was subtracted to allow a determination of the VB contribution stemming from the metallic nanocatalysts. The subtraction was performed only in those cases where the metal content of the sample was very low, such that the contribution of the support became significant in the VB spectra. As an example, this was the case for the acid-treated Pd-Cu 1:3 catalyst depicted in Fig. 3.5. In order to extract the metal VB, a weighted contribution of the support VB was subtracted from the original data (see. Fig. 3.5). This weight was chosen such that the intensity at a binding energy of 10 eV was close to zero after the subtraction procedure. Due to the small contribution of the support VB up to 4 eV, this procedure does not significantly alter the VBS in this region. At higher binding energies, however, the uncertainty in the correct weight of the carbon support contribution makes spectral features below a binding energy of 4 eV of the difference spectrum less reliable.
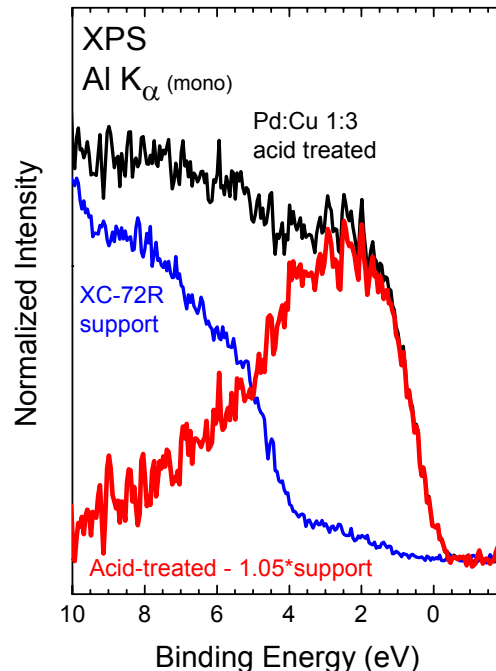
Fig. 3.5: Subtraction procedure used to separate the experimental VB (black curve) into contributions from the support (blue curve) and the metal nanocatalysts (red curve).

Section 3-4

Sample Preparation and Temperature Calibration

3-4.1 Sample Cleaning

All metal reference foils analyzed in this dissertation were cleaned by Ar^+ ion sputtering using a VG EX05 ion gun. In this technique, a beam of argon ions is rastered on the sample surface. Through collisions, atoms on the sample surface (e.g., adsorbate species) can be removed. Ion energies between 2 keV and 5 keV were used, with sputtering currents of about 1.5 mA (2 keV) and 15 mA (5 keV). Surface cleanliness was verified by taking detail spectra of the C 1s and O 1s energy region. Sputtering was conducted until no or only trace amounts of carbon and oxygen could be detected on the sample surface.

The alloy foil samples investigated in Chapter IV were mechanically cleaned with 400grade sand paper under dry nitrogen atmosphere prior to introduction into UHV. Sample cleaning by Ar^+-ion sputtering was avoided in this case because one of the alloying element (Cu) has been found to be sputtered preferentially (as compared to Pd) [49, 50], which would artificially modify the surface composition of the sample.

The nanocatalyst samples synthesized by ANL were packed and shipped according to the standard packing procedure of the UNLV group, in which the samples are packed under inert atmosphere and in two sealed bags, one evacuated and sealed with a food saver, and one filled with dry nitrogen and a desiccant. Through this procedure, contaminations due to ambient air can be minimized.

3-4.2 Sample Mounting and Preparation

All samples were mounted onto sample holders in a glove box under inert conditions (the glove box is filled with N_2 gas from a liquid nitrogen dewar) and introduced into UHV in the as-received state (unless otherwise denoted). The powder-like nanoparticle samples were mounted on vacuum-compatible sticky carbon tape.

Pd and Cu thin-film deposition was performed using an Omicron EFM3 UHV e-beam evaporator equipped with an integrated flux monitor, which was calibrated via an ion current measurement [51]. The film thickness was controlled via the evaporation time and flux, and calibrated by the attenuation of substrate signal in XPS. The individual deposition times and flux of the deposited Pd and Cu thin-films are presented in Chapter VI.

3-4.3 Calibration of the Temperature Scale

During the annealing studies presented in Chapter VI, the thermocouple mounted on the manipulator was located ca. 10 mm away from the sample, with inferior heat contact to the heating element, which resulted in a lower temperature reading at the thermocouple compared to the sample surface. This problem was corrected by using a pyrometer (Raytek Marathon MM1ML) for temperatures over 450°C (the minimal temperature of the pyrometer readout) and extrapolating to lower temperatures. All sample temperatures listed in Chapter VI represent the values after the correction. The linear fit used to determine the temperature correction is presented in Fig. 3.6. Error bars are thus ±30 °C for temperatures above 450 °C, and ±50 °C for temperatures below 450 °C.
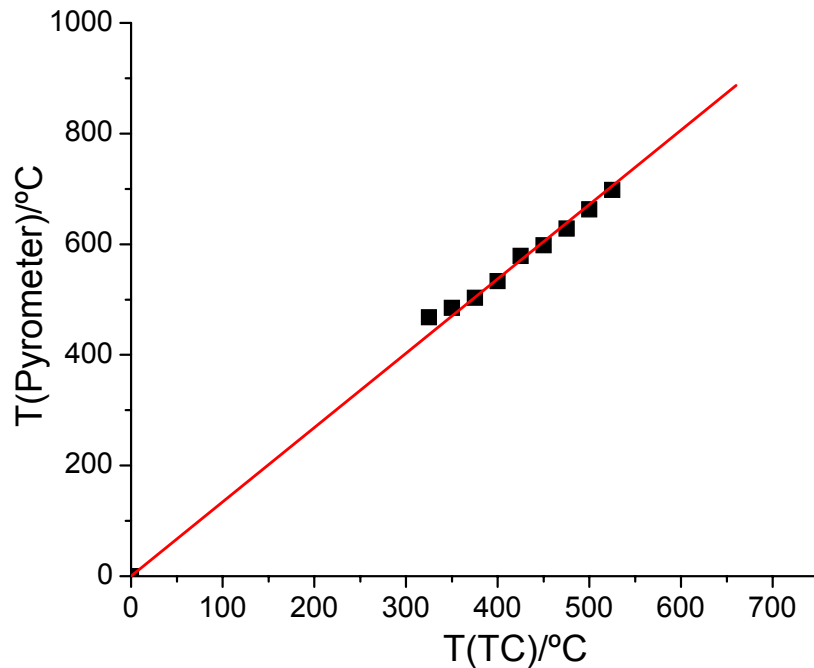
Fig. 3.6: Linear fit of the Pyrometer temperature scale to the one of the thermocouple.

CHAPTER IV

EXPERIMENTS ON METAL REFERENCES

To deliberately mimic the electronic structure of Pt and to gain insight into the catalysis process of the oxygen reduction reaction (ORR) requires a substantiated knowledge of the basic systems. As mentioned in the Introduction, we are approaching this challenge by investigating the electronic structures of (a) the pure constituent metals (i.e., Pd and Cu), (b) commercial alloy foils, (c) in-situ-prepared thin film systems, and (d) chemically synthesized nanocatalysts. In this chapter, we report on the results obtained from pure metal references.

Photoemission experiments were performed on clean reference metal foils of high purity (99.9% pure or higher). The valence band structure (VBS), containing the weakly bound electronic states that can partake in chemical bonding and reactions (such as, e.g., the ORR), was investigated by UPS and XPS for Pd, Cu, and metals commonly found in catalysts. Section 4.1 presents the results of a UPS valence band (VB) study of Pt, Pd, Co, Cu, Fe, and Ni using He I and He II excitation. The interaction and effects of adsorbates on the VBS will be discussed in detail. In Section 4.2, the XPS VB of Pt (as a reference) along with the VBs of the here investigated noble/base metal combination Pd/Cu will be described and compared to the theoretical DOS as calculated by our project partners at Caltech. With reference to literature studies we briefly point out the relevance of the d states with t_{2g} symmetry for catalysis in Section 4.3. Finally, Section 4.4 summarizes the results of our UPS and XPS experiments on metal references and the insights provided by the calculations. Later in this dissertation the obtained reference

spectra will be used for comparison with valence band structures of alloys (Chapter V),

thin film bimetallic samples (Chapter VI), and finally nanoparticle catalysts (Chapter

VII).

Section 4-1

Metal Valence Bands measured by UPS and the Influence of Adsorbates

In an initial study, the VBS of clean metal foils (Pt, Pd, Co, Cu, Fe, Ni) of high purity

were determined by Mg K_α XPS and UPS at the "Andere ESCA" photoemission system.

Samples were cleaned by Ar^+-ion sputtering (see Chapter III for details of the cleaning

procedure and right hand side of Fig. 4.1 for treatment time) until no appreciable carbon

or oxygen signal could be detected. Fig. 4.1 shows the XPS survey spectra of the clean

metal reference foils.
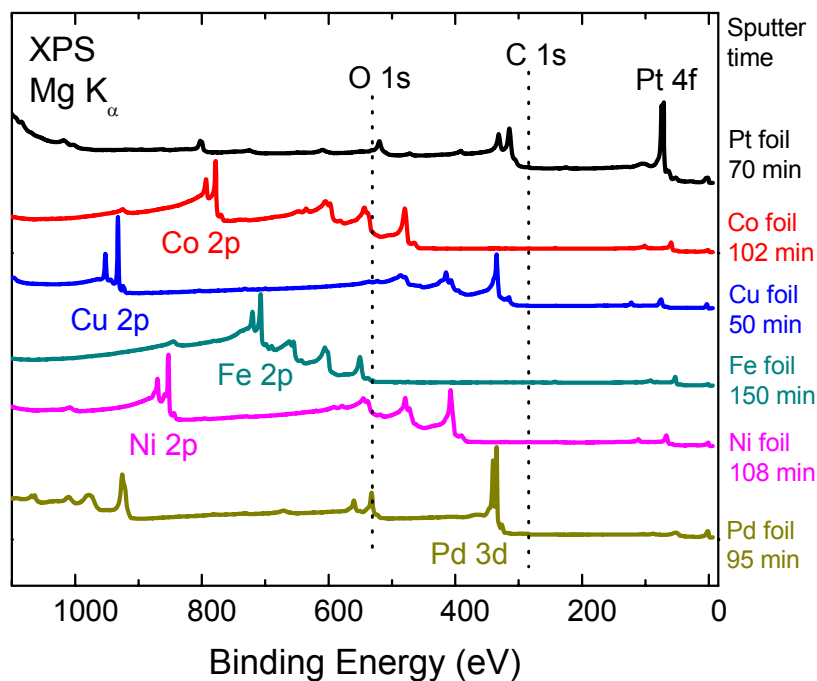
Fig. 4.1: XPS survey spectra of Ar^+-sputtered high purity metal reference samples.

The dotted lines in the graph mark the common binding energy of O 1s and C 1s, respectively. The absence of appreciable spectral intensity along these lines suggests that the samples were successfully cleaned of surface adsorbates from the viewpoint of XPS. Note that a careful look at XPS detail spectra of the C 1s and O 1s region indicates very minor residual carbon and oxygen contributions in all cases except for Cu, which will be further discussed below.
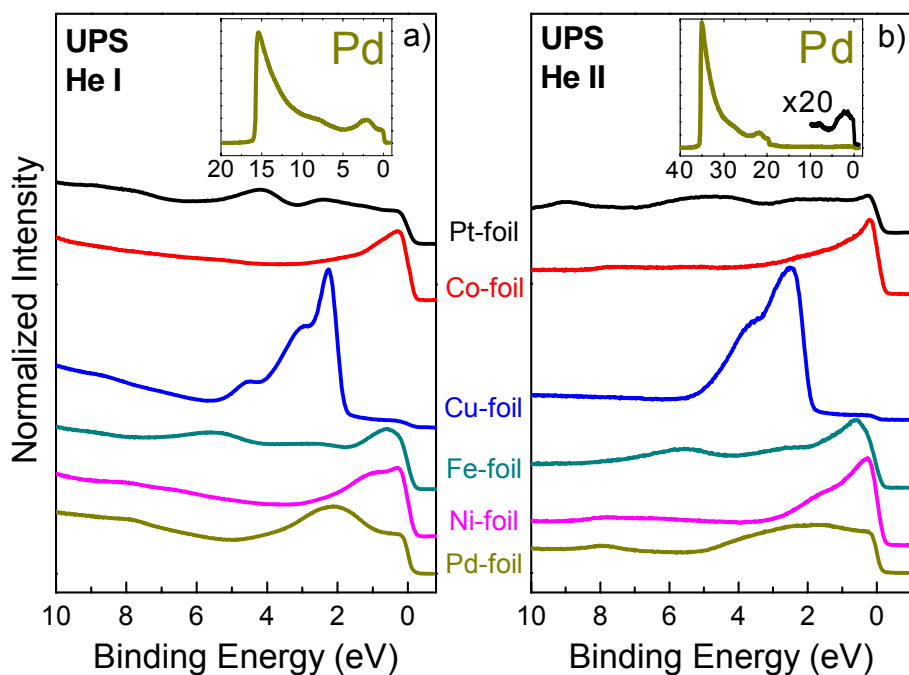
Fig 4.2: UPS spectra of metal reference foils recorded a) with He I excitation and b) He II excitation. The insets show survey spectra of Pd recorded with He I and He II, respectively.

To study the VBS, non-monochromatized Mg K_α XPS is not suitable due to the overlap of spectral features with additional structures due to the Mg $K_{\alpha,3,4}$ satellites. We have thus employed He I and He II UPS to gain insight into the VBS. Fig. 4.2a shows the VB of the metal foils as measured by UPS using the He I emission line at 21.22 eV. As

expected for metals, all spectra show a pronounced Fermi edge. For Cu, whose d-band is fully occupied, the Fermi edge is less pronounced because it is mainly made up of s-electrons with contributions from the d- and p-bands (see DOS of Cu in Fig. 4.6).

The characteristic VBS peaks of each metal are found within the first 6 eV. Noticeable for all He I-excited spectra is the strong influence of the background. The region of interest, i.e., the catalytically active states is superimposed with the slope of the secondary electron peak. This can most easily be seen by the inset graph in Fig. 4.2a, which exemplarily shows the UPS survey spectra of the Pd foil. In the case of He II excitation (40.8 eV), the background from secondary electrons interferes far less than that of He I, as can be seen from the survey spectra inset in Fig. 4.2b and when comparing the slope of the backgrounds between spectra measured by He I and He II. Apart from the differences in background, the spectral shapes obtained from He I and He II appear quite similar at first glance. A closer look, however, reveals pronounced and subtle changes in intensity for all samples. Since all foils studied are of polycrystalline nature, no predominant crystal orientation is expected. If present, such an orientation could lead to significant variations in the VBS, because transitions become dependent on the band structure (in particular the availability of a suitable final state) along the respective crystal orientation [37].

Such changes can be ascribed to final state effects, variations of the photoionization cross section, influences of the background, modification of the electron inelastic mean free path (IMFP) (as discussed in Chapter III), and/or adsorption of residual gas molecules on the sample surfaces. The latter effect will be discussed in the following.

As mentioned, all metal references (with the exception of Cu) in this series showed minor residual carbon and oxygen amounts on the surface. To analyze this further, we have investigated the He II UPS spectra in more detail. They exhibit small peaks around 8 and 11 eV, which may be derived from the 5σ- and 1π-orbitals of adsorbed carbon monoxide [52-54]. From the associated (very small) difference in work function between our measurement (5.4 ± 0.1 eV) and the literature value of 5.22 eV [55] we estimate an upper bound for a potential coverage of CO on our Pd sample to be below 0.2 monolayers (ML). We point out that this residual C and O contamination could be due to both, residuals from surface cleaning and/or readsorption in the UHV environment. Consequently, great care was taken for the further experiments to optimize the cleaning procedures and to minimize the time between sputtering and experiment. Furthermore, we decided to solely rely on valence band structures derived from Al K_α XPS measurements. As discussed earlier, these probe the VBS with a substantially higher IMFP, and thus are much less susceptible to possible surface adsorbates in the sub-monolayer regime.

After the initial Mg K_α XPS core-level and UPS VBS studies at the "Andere ESCA" system and the identification of critical parameters that influence the spectral information (as discussed here and in the preceding chapter), further studies were performed in the "Scienta" system. Besides being most comparable to a DOS measurement (as discussed in Chapter III), Al K_α XPS is also less sensitive to small amounts of residual gases on the sample surface (compared to He II UPS) because of the vanishing cross section for molecular levels at elevated electron energies [45] and the larger information depth. Furthermore, our system includes a *monochromatized* Al K_α source, which allows the

compilation of VB spectra without the interference of satellites from the excitation source (and with substantially improved spectral resolution).

In the following section, the VBS of Pt, Pd, and Cu as measured with monochromatized Al K_α will be discussed. Particular emphasis lies on testing the underlying assumptions of the d-band center concept, and the comparison of the XPS VBS with the theoretical DOS computed by our collaborators at Caltech. Especially the contribution of the various electronic levels to the VBS will be discussed and adjusted to fit the experimental VBS in order to gain a deeper understanding of our XPS results and their correlation to the DOS.

Section 4-2

Metal Valence Band Structures determined by XPS and Computational Methods

In order to test the prediction that the d-band center is correlated with the calculated trends in ORR activity [56], we have investigated the valence band of various transition metals by monochromatized Al K_α XPS and determined the d-band center position as the weighted average of the occupied valence band states, as described by Mun et al. in [24]. The energy range is arbitrarily limited to 10 eV binding energy and a Shirley background is subtracted from the measured spectrum to account for the background produced by inelastically scattered electrons [24].

Fig. 4.3a shows VB spectra for a variety of metal references. All d-band centers marked in Fig. 4.3a and listed in Table 4.1 were determined in the above-described fashion. When comparing the d-band center positions with the trends in ORR activity plotted in Fig. 4.3b (adapted from [57]), it becomes obvious that there is no correlation as

predicted theoretically. In particular, Pt and Cu exhibit similar d-band centers, while the respective ORR activity and the DOS in the valence band differs significantly. This shows that it is not sufficient to only use the d-band center as representative for the overall valence band structure and the interaction of the metal with oxygen. While the d-band center approach might be feasible to be used as an indicator of the ORR activity for a constant host system with minor alloying variations, such as Pt$_3$-M (M=Fe, Co, Ni) (as reported in [24]), it can clearly not be used to compare systems with substantially different electronic structures (such as Pt and Cu). Hence, it is necessary for the spectral distribution to be analyzed experimentally in order to determine if a catalyst has a "Pt-like" electronic structure.
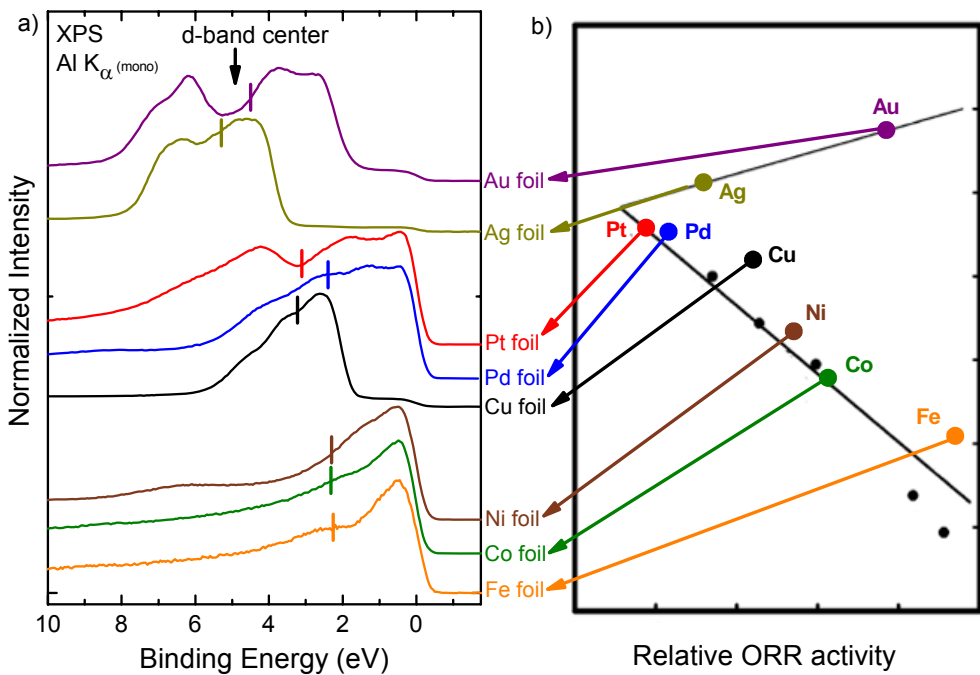
Fig. 4.3: a) Al K$_\alpha$ XPS spectra of a variety of reference metals, together with their d-band center positions indicated by vertical lines; b) calculated trends in oxygen reduction reaction activity (adapted from [57]).

Table 4.1: Experimentally determined d-band centers of transition metals

Element	Ag	Au	Cu	Pt	Pd	Co	Fe	Ni
d-band center/eV	5.3±0.1	4.5±0.1	3.2±0.1	3.1±0.1	2.4±0.1	2.3±0.1	2.3±0.1	2.3±0.1

In addition to the lack of correlation of the experimental d-band center position to the theoretically predicted trends in ORR activity, the absolute value of the experimental d-band center is also highly dependent on the photon energy used, as discussed in Chapter III. Note, however, that the here employed Al K_α excitation gives spectra with highest resemblance of the actual (initial-state) DOS (as also discussed in Chapter III). Thus, since the d-band center was found to exhibit no direct correlation to the ORR activity, it was not further used for the valence band investigations reported in this dissertation.

Having demonstrated the importance of investigating the entire valence band structure of candidate metals or alloys for fuel cell catalysts, it is important to have a substantiated knowledge of the intrinsic electronic levels of Pt and the metals intended to substitute it with – Pd and Cu. We will discuss the origin of the electronic structures of Pt, Pd, and Cu that make up the valence band by comparison to theoretical studies performed by our partners at Caltech.

For the experimental VBS of platinum ("XPS") we find six characteristic features, marked with an encircled number in Fig. 4.4a: (1) a peak at 0.4 eV, (2) a valley at 1.1 eV, (3) a broad peak at 1.7 eV, (4) a second valley at 3.2 eV, (5) a broad peak at 4.2 eV, and lastly a pronounced shoulder at 6.2 eV (6). Also shown in Fig. 4.4a are the symmetry-resolved theoretical contributions to the Pt DOS, as well as the theoretical total DOS (TDOS). All of these curves were calculated at Caltech and will be discussed in detail in the following. Fig. 4.4b shows the calculated Pt TDOS (gray) and compares it to

published theoretical results by Santarossa et al. [58], Kokalj and Causa [59], Shirley et al. [37], and the experimental spectrum (bottom to top). While the overall DOS peak structures look similar (in particular among some of the theoretical results), the intensities and energetic positions reveal significant differences between theory and experiment that demonstrate the complexity to describe the Pt DOS correctly (note that DFT is commonly known to underestimate band widths in most systems (see [60, 61] and references therein).
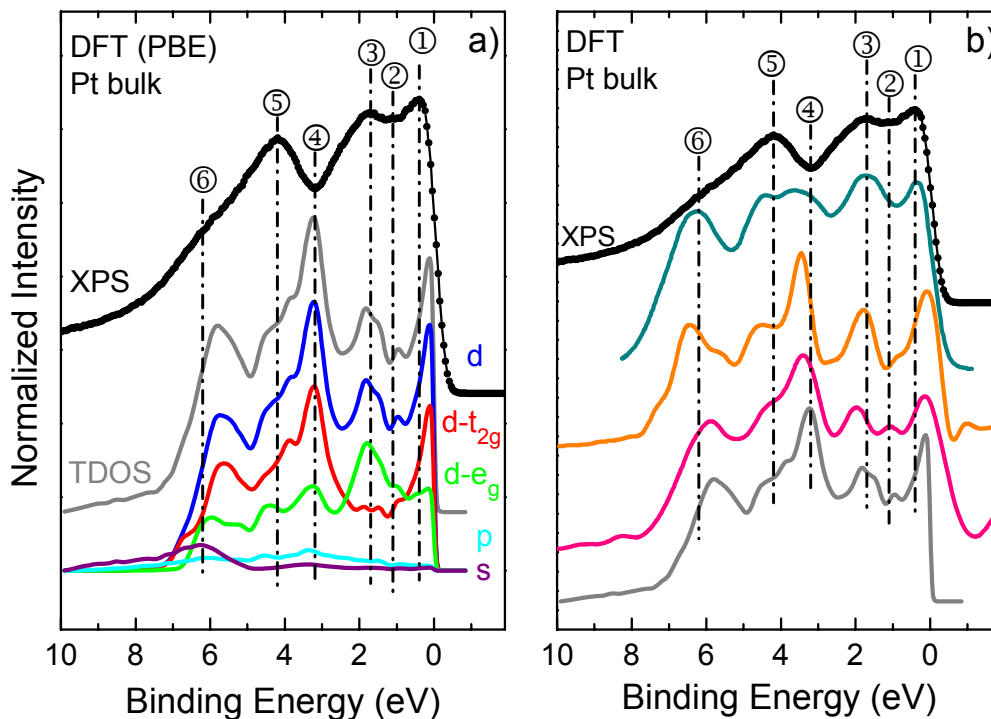
Fig. 4.4: a) Symmetry-resolved (broadened) theoretical DOS, total theoretical DOS ("TDOS"), and experimental Al K_α XPS spectrum of Pt. The encircled numbers denote characteristic peaks and valleys in the XPS spectrum. b) Pt bulk DOS curve calculated at Caltech (gray, bottom, equivalent to "TDOS" in a)), in comparison to Pt DOS curves from Santarossa et al.([58], red), Kokalj and Causa ([59], orange), Shirley et al. ([37], dark green), and the experimental XPS valence band spectrum of Pt.

The most striking feature of the VBS of Pt is certainly the broad valley (4) that seems to divide the spectra into two parts and is often interpreted as a splitting of the d-band in Pt [62-64]. Its origin is controversial and has been discussed extensively in literature.

The spatial extent of the d-states is much smaller compared to other valence states (of s and p character), and decreases rapidly in intensity with increasing distance from the nucleus. As a result, d-states are not strongly perturbed by the crystal potential and overlap only slightly with the atomic states of neighboring atoms. It is this peculiar character of the d-bands that makes computational studies and their interpretation challenging, as neither a localized atomic orbital picture nor a description using the molecular orbital approach yield a satisfactory explanation [63]. Besides Pt, pronounced dips in the VB of Ir, Au, Rh, and Ag have been observed experimentally (see also Fig. 4.3a for Au, Ag, [62, 65] for Ir, [66] for Rh) and predicted theoretically (e.g., [65, 67, 68]). The origin of the dips has been linked to spin-orbit splitting in the above cases. In a theoretical study, Christensen found that the spin-orbit parameter for Ag, Pt, and Au are comparable to the d bandwidth and therefore responsible for the splitting of the DOS observed theoretically and experimentally [67]. This view is further supported by results published by the Shirley group [65], Mattheiss et al. [69], Andersen et al. [70], and MacDonald et al. [71]. MacDonald et al. found that the spin-orbit splitting increases in magnitude as one goes from the bottom to the top of the band because the wave functions at the top of the band penetrate closer to the nucleus. For Pt the splitting at the top of the band becomes a significant fraction of the d-band width and can thus be regarded as the origin of the partial separation of the $d_{3/2}$ and $d_{5/2}$ bands observed in the Pt VB (see feature 4 in Fig. 4.4).

For all theoretical curves of the computational DOS shown in this chapter, the contributions from the individual wave functions (s, p, d) were broadened by convolution with Gaussian peaks of 300 meV width (solid lines in Fig. 4.4) to account for experimental broadening in the experiment. The resolution of the experiment (Al K_α excitation source and electron analyzer), e.g., the full width at half maximum (FWHM) of a Fermi-function fit to the Fermi edge, was determined exemplarily for a gold foil. Using the procedure described by L. Weinhardt in [72], the resolution (FWHM) was calculated to 477 meV for the spectrometer settings employed in this dissertation. The best combined resolution of the Scienta system (i.e., of the Al K_α excitation source and the electron spectrometer), obtained for very low pass energies, is 289 meV.

In order to account for the larger FWHM of the experiment (477 meV), the spectra in the following parts of this dissertation have been convoluted with a 500 meV Gaussian function (instead of the 300 meV mentioned above). The theoretical DOS (that describes the electron distribution at 0 K) was furthermore adjusted to reflect the occupation of states at room temperature through multiplication with the Fermi function at 300 K.

Comparison of the wave functions for Pt in Fig. 4.4a shows that the total density of states (TDOS) is almost entirely made up of the d-bands, except for some contribution to the TDOS by s-states at higher binding energies (which might point to a hybridization with the d-bands). The p-band share of the TDOS is very low, but present throughout the entire d-band, which agrees well with the findings of Kokalj and Causa [59]. If a sufficiently good agreement between experiment and theory is achieved, then the wave functions and energy regions involved in the ORR can ideally be identified. In Section 4-3 we outline some results from published literature that hint towards an involvement of d-

42

orbitals with t_{2g}-symmetry in catalytic processes. While the features 1-3 of the XPS spectrum in Fig. 4.4 are in adequate agreement with the theoretical DOS, features 4-6 do not agree well with the experiment in terms of energy position and/or intensity. We will address this issue at the end of this section and demonstrate how the agreement between experiment and theory can be improved significantly (keeping in mind that DFT generally understimates band widths).

Having established a basic understanding of the Pt VBS, we will now discuss in detail the VBs of Pd and Cu. A detailed knowledge of the individual Pd and Cu electronic structures is crucial, as it forms the foundation for the understanding of the Pd-Cu alloys, thin-film systems, and nanoparticle catalysts that will be discussed in the following chapters. The VB of Pd as measured by Al K_α XPS at RT is shown in Fig. 4.5a. Characteristic peaks are found at 0.45 eV (1), 1.2 eV (2), 2.4 eV (3), 4.2 eV (4), and 8.0 eV (5) (see encircled numbers in Fig. 4.5a), in very good agreement with previously published results [68, 73-75]. The peak at around 8.0 eV is a satellite peak resulting from a two-hole final state [75, 76].

As in the case of the theoretical DOS of Pt, the ones reported for bulk Pd are also quite similar to each other [67, 68, 71, 77, 78] and to the DOS calculated at Caltech (see Fig. 4.5b). Furthermore, the experimental peaks in the XPS VB at 1.2 eV, 2.4 eV, and 4.2 eV (denoted 2-4 in Fig. 4.5a) coincide closely with features in the theoretical DOS. The first XPS peak at 0.45 eV is found closer to the Fermi energy in the DOS, most likely due to the broader Fermi distribution in the experiment (477 meV in the experiment vs. 300 meV Gaussian broadening of the calculations). Similar to Pt, the VBS is dominated by the d-states.
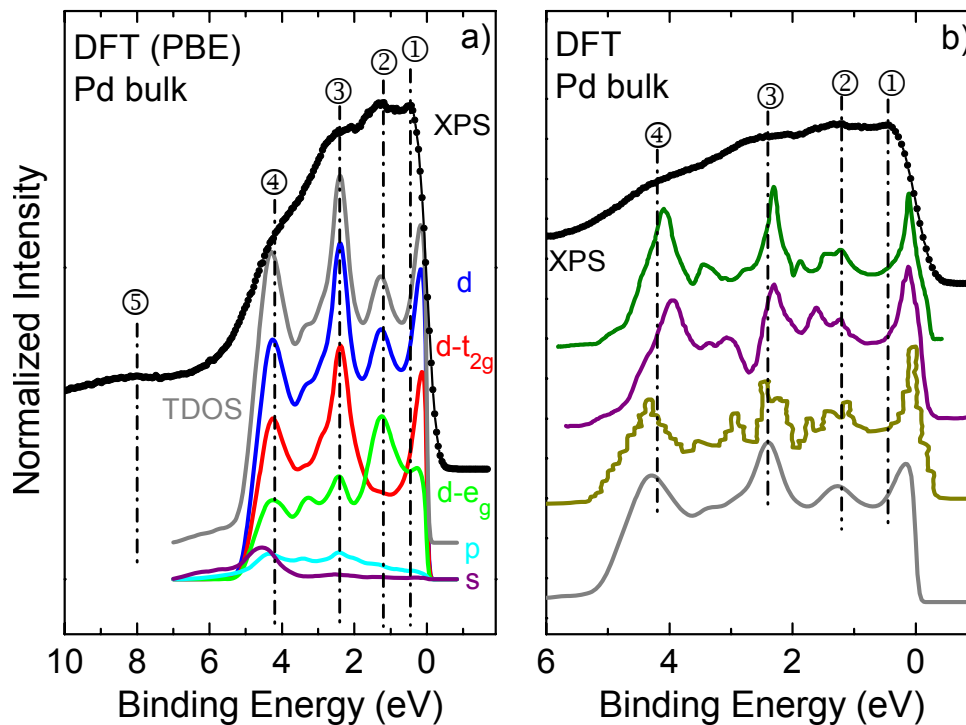
Fig. 4.5: a) Theoretical DOS (broadened) of bulk Pd in comparison to the XPS valence band of Pd. The encircled numbers denote characteristic peaks in the XPS spectrum. b) Pd DOS curve calculated at Caltech (gray, "TDOS" in a)) in comparison to results from Smith et al. (dark yellow,[68]), Nemoshkalenko (purple,[79]), Janak (green,[77]), and the XPS valence band of Pd.

The contribution of the p-bands is present throughout the VB, but small. The influence of the s-band is negligible with the exception of some intensity emerging around 4.6 eV. In this region, hybridization of s- with d-states would be possible, but is predicted by Andersen et al. to be less important than in the case of Pt [70], while Hüfner et al. state that the d-band of Pd is strongly hybridized with the s-band [73]. Close to E_F (1) and around 2.4 eV (3), the DOS is dominated by the d-t_{2g} sub-band, while the most indicative contribution for the d-e_g band is the peak around 1.2 eV (2).

We will now turn our attention to the electronic structure of Cu. The VBS of the Ar$^+$-ion cleaned Cu foil is shown in Fig. 4.6a. Compared to the VBS of Pt and Pd, the narrow d-band width of Cu stands out. Due to the filled 3d shell in Cu, the DOS close to E_F is

fairly low. We find the observed VB to be in excellent agreement with published calculations (e.g., [37, 40, 79]). Four characteristic features (labeled 1 − 4 in Fig. 4.6) can be distinguished: a peak at 2.5 eV (1), a shoulder at 2.8 eV (2), a pronounced shoulder at 3.5 eV (3), and a third shoulder at around 4.5 eV (4).
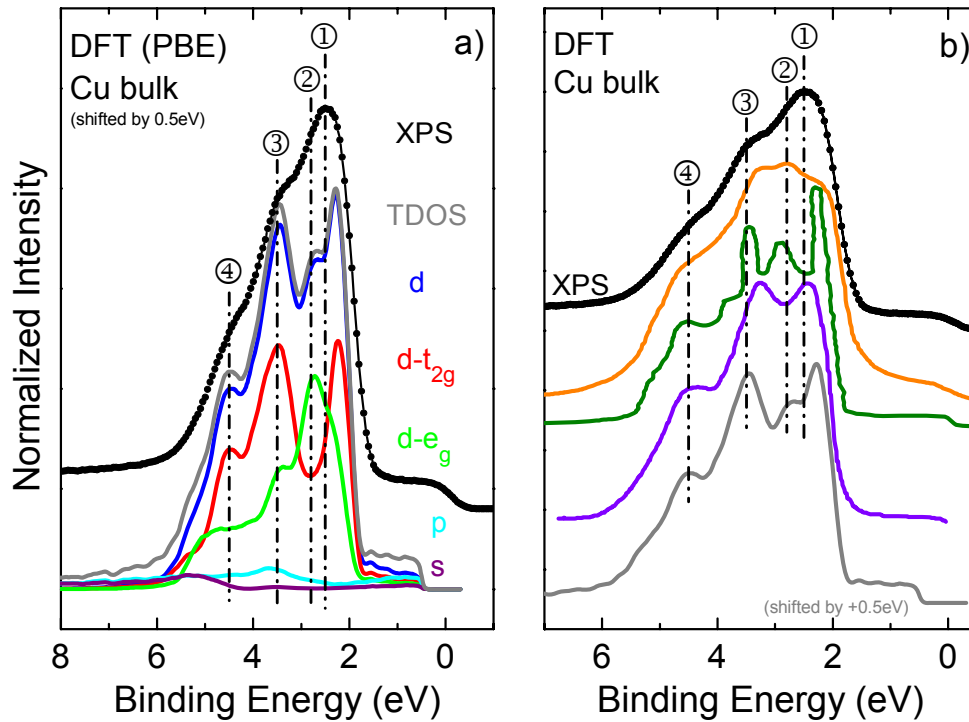
Fig. 4.6: a) Theoretical DOS (shifted by 0.5 eV) (solid lines) of bulk Cu, in comparison to the XPS valence band of Cu. b) Cu DOS curve calculated at Caltech (gray), in comparison to results from Shirley et al. (purple,[37]), Wertheim et al. (green,[40]), Hüfner et al. (orange,[80]), and the XPS valence band of Pd.

In order to shed light on the contributions of the individual wave functions to the DOS of Cu we have plotted in the theoretical DOS of Cu Fig. 4.6a along with the experimental XPS VB. To achieve a better agreement, the theoretical DOS curves were broadened by a convolution with a 500 meV FWHM Gaussian function and shifted linearly by +0.5 eV (with respect to the experimental spectrum) to align the position of

the d-bands, which is predicted inaccurately (too high) by theory. Note that this shift leads to the fact that the Fermi edge in the theory curves is now found at a binding energy of 0.5 eV (and not at 0.0 eV). Fig. 4.6b presents the Cu DOS reported by Shirley et al. [37], Wertheim et al. [40], and Hüfner et al. [79]. Overall, there is a good qualitative agreement between all DOS spectra. Peak intensities and positions, however, differ. After the linear shift of the DOS calculated at Caltech (0.5 eV, grey lines), the XPS features 2-4 in Fig. 4.6a almost coincide with their theoretical counterparts and the overall DOS fits better to the published results (Fig. 4.6b). A closer look at feature 1 in Fig. 4.6a shows that it results from the superposition of the first two peaks in the d-DOS, rather than stemming from one single peak in the DOS. Although the filled d-band suggests that the DOS in the vicinity of E_F ($0 - 1.8$ eV) should be made up of mainly s- and p-states, the calculations predict that all three bands contribute to the DOS in this region. Apart from that, the DOS of the p-band and s-band are only significant around 3.6 eV and 5.2 eV, respectively. The VBS consists, similar to our findings for Pt and Pd, almost entirely of d-states. Close to the major onset of the DOS around 2.2 eV, states with t_{2g}-symmetry dominate.

To improve the agreement between experiment and theory (in particular the band width), the calculated DOS for Pt, Pd, and Cu were adjusted further. The corrections to the respective DOS were performed in such way as to yield the best visual agreement between experiment and calculation. As a starting point, the TDOS was broadened with a 500 meV Gaussian function, as mentioned above. In a second step, the energy axis of the DOS spectra was stretched to reconcile the position of features on the binding energy axis. This is a commonly used approach to correct the above-mentioned shortcoming of

DFT to underestimate band widths (and band gaps) [60, 61]. Next, we focus on the photoionization cross section. Due to its dominance, only the d-band, consisting of d-t_{2g} and d-e_g symmetry, was considered. When comparing the overall intensity between theory and experiment of all metals studied, it is noticeable that the lowest band in the VBS has higher intensity in the calculations that in the XPS experiment. This finding has been reported for numerous transition metals and has been linked to variations of the photoionization cross-section across the d-band [68, 80-83]. While Smith et al. [68] suggest mixing of d states with s- and p-states to be responsible, Shevchik et al. argue that the charge-density overlap between d orbitals on adjacent sites leads to a cross section which depends on the initial-state energy [81]. When charge density overlap is taken into account, the photoionization cross section σ becomes proportional to an energy-dependent renormalization term. The variation of σ can then, in first order, be accounted for by multiplying the intensity by a renormalization term $(1 + \lambda E_i)^{-1}$, where E_i is the energy with respect to the center of the DOS (i.e., the d-band center) and λ is an adjustable parameter (λ is defined negative in Ref. [81] since the binding energy is denoted negatively as well; as we use positive binding energies throughout this dissertation, λ is a positive parameter in our case). Moreover, Nemoshkalenko et al. found that electrons with e_g symmetry have higher transition probability than those with t_{2g} symmetry [83].

Therefore, in total, the d-DOS spectrum was corrected by assuming decreasing cross-sections towards higher binding energies for both symmetries and variation of the e_g to t_{2g} ratio in order to achieve the best visual agreement between experiment and theory. The various parameters used to adjust the theoretical DOS are outlined in Table 4.1. The

experimental data was also corrected for the background created by inelastically scattered electrons by subtracting a Shirley background. Fig. 4.7a shows the modified d-DOS of Pt, Pd, and Cu, together with the two symmetry contributions and the experimental spectra. The agreement is significantly improved, as can be seen by comparison to the uncorrected DOS curves (and experimental spectra) in Fig. 4.7b. For Pt, the features 1-5 are now very similar in energy position and intensity. The main discrepancy is the missing feature 6 at 6.2 eV in the DOS and the non-existence of the broad peak around 7.3 eV that is present in the DOS but not in the XPS spectra. Since the latter is present in both the d-e_g and d-t_{2g} sub-band (and also to a lesser extent in the s-DOS), one would expect to find a shoulder in the XPS spectrum.

Table 4.1: Correction parameters used to adjust the theoretical DOS

element	E_i (d-band center)/eV	λ	e_g:t_{2g} ratio	E axis
Pt	4.15	0.08	2.8:1	stretched by 1.25
Pd	2.47	0.12	2.4:1	unchanged
Cu	3.52	0.06	2.1:1	shifted by +0.5 eV

It is possible that the stretching applied to the energy axis worsened the agreement in this case, as the agreement between XPS and DOS for feature 6 was previously far better (see Fig. 4.4). According to Hodges et al., the lower d-bands hybridize most strongly with s- and p-bands [68, 84]. This could lead to a shifting of the DOS and also to a lowering of the photoionization cross-section (s and p states have a significantly lower cross-section at XPS energies as compared to d states), thus potentially causing the peak to "disappear" in the experimental spectra.

After the adjustments to the theoretical DOS of Pd, the agreement is visibly improved. The most striking deviation is the intensity variation for the peak at 4.2 eV (4) between experiment and theory, similar to peak (6) in the Pt case. Once again, this could possibly be due to a shift or a lowering of intensity due to hybridization of the d-band with the s- and p-bands.
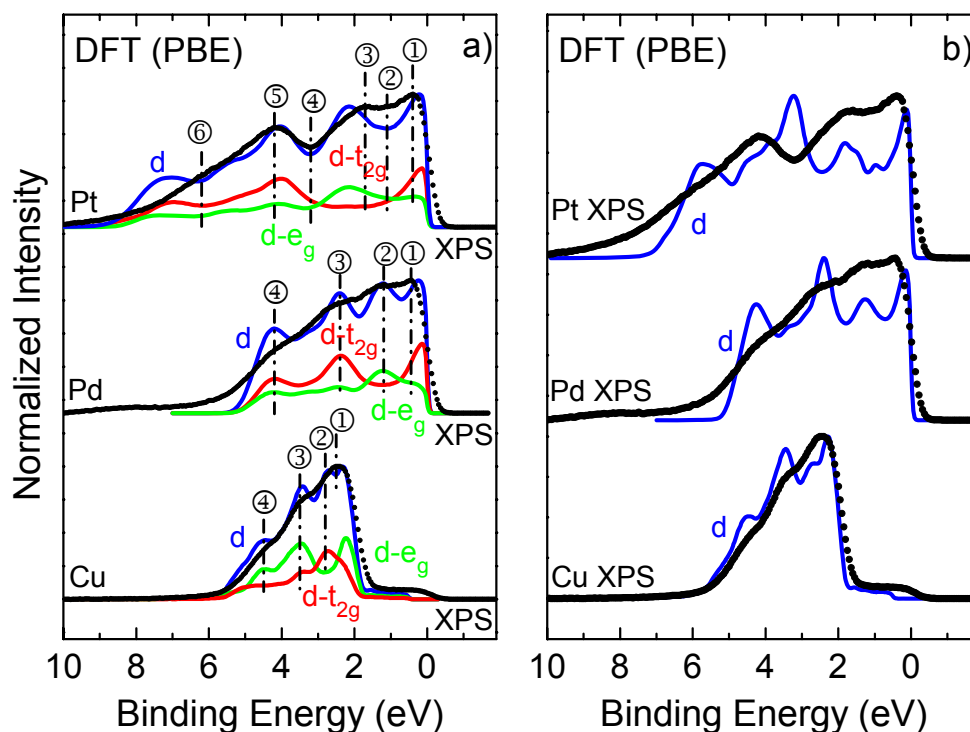
Fig. 4.7: a) Theoretical density of states (solid lines) of Pt, Pd, and Cu adjusted for variations of photoionization cross-section and e_g to t_{2g} transition probability. For comparison the experimental XPS spectra are shown (black lines). b) Density of states (solid lines) of Pt, Pd, and Cu before corrections have been applied in comparison to the experimental XPS spectra.

For the modified d-DOS of Cu as presented in Fig. 4.7 the energy axis of the DOS was shifted linearly by 0.5 eV to match the experimental axis. No additional stretching or contraction was applied, even though the 0.5 eV shift creates a significant discrepancy at the Fermi energy. After the corrections, the agreement of intensities in the d-band region

is significantly improved. All features (1 – 4) show good agreement in terms of energy position. The intensities of (3) and (4) are somewhat less pronounced in the XPS spectrum, even after correcting the DOS for the lower photo-ionization cross-sections experienced in XPS. The appearance of s- and p-states close to (3) and (4) offers hybridization effects as a possible explanation. Another hypothesis is offered by the study of Hüfner et al. on a Cu (001) single crystal. The authors found that, while the second layer is already quite representative of the bulk, the surface layer DOS of Cu(001) is narrowed and peaks at the top of the d-band [85]. Thus, the intensity contribution from the first layer might additionally contribute to the mismatch of theory and experiment.

Section 4-3

Relevance to Catalytic Properties

In the following, we briefly discuss the contributions to the VB that have been identified in published literature to be catalytically active.

In general, the density of states at the Fermi energy is most important in determining the physical properties (e.g., transport properties, specific heat, ferromagnetism,…) of a metal [84]. Likewise, the uppermost valence electrons are those generally expected to take part in chemical interactions. Shirley et al. found that, when CO chemisorbs on the (111) face of Pt, the VB peak close to the Fermi energy always decreases in intensity relative to the other peaks in the UPS-derived Pt VB [37]. This suggests that the states close to the Fermi energy donate electrons to the CO molecule as it chemisorbs [37]. Likewise, a lowering of the intensity close to the Fermi energy for Pt(100) has been observed upon CO adsorption (using XPS) [64]. As most of the DOS in this region is of

t_{2g} symmetry (see Fig. 4.4, [37, 64]), this d-sub band seems to be most involved in chemisorption of CO and could potentially also play a crucial role for the interaction with O_2. As mentioned earlier, the spin-orbit splitting becomes significant at the top of the d-band. Thus, wave functions in this chemically active region are much more localized than at the bottom of the band and as compared to 4d and 3d metals. This is an important find, because the degree of localization/mixing of wave functions will certainly influence the overlap with adsorbate states and therefore be crucial for the catalytic activity.

Studies that examine the influence of gases (CO, O_2, H_2) on the Pd VBS unanimously show that, upon chemisorption, the intensity close to E_F decreases and new states appear at higher binding energies [53, 75, 86]. Thus, as in the case of Pt, the top of the band (consisting of mainly t_{2g} character), seems to be involved in forming bonds to adsorbed molecules and is therefore critical for catalysis. This makes Pd a good candidate to mimic Pt, as it, too, exhibits a high DOS with d-t_{2g} symmetry at E_F. When oxygen is adsorbed on Cu, two new resonance levels at 5.5 eV and 1.5 eV are formed [87]. The Cu VB, furthermore, experiences a sharp loss in intensity near the top half of the d-band ($2-3$ eV below E_F) [87]. It is therefore likely that t_{2g} states are involved in forming bonds to the adsorbed molecules. In summary, thus, it appears likely that the t_{2g} states play a crucial role in determining whether a custom-tailored electronic structure (e.g., of Pd-Cu nanoparticle alloys) mimics that of Pt or not. This is an important concept, since it advances significantly beyond the previously adopted d-band center approach. All experimental spectra presented in the remainder of this dissertation will need to be judged from this viewpoint – does the tailored electronic structure (of, e.g., a bilayer system, an alloy, or a nanoparticle catalyst) mimic the DOS of Pt near the Fermi energy or not?

Section 4-4

Summary

The valence band structure of various metal references was determined experimentally (by UPS and XPS) and compared to the theoretical DOS of the respective metals. It was found that numerous experimental considerations make UPS an inferior choice to study the DOS of catalytically active systems. In contrast, XPS valence bands recorded with monochromatized Al K_α radiation promise to be most closely comparable to the ground state properties and thus comparable to theoretical calculations. The VBs of platinum, palladium, and copper derived by XPS were compared to calculated DOSs. We could show that the variation of photoionization cross-section with energy, differences in the transition matrix-elements for various wave function symmetries, hybridization and spin-orbit splitting need to be considered to achieve a good theoretical description of the XPS valence band spectra based on the calculated DOS. From previous publications that examine the interaction of gas molecules with metal surfaces, it appears that bands with d-t_{2g} symmetry are involved in the interaction with gas molecules in all cases (Pt, Pd, and Cu), and our spectra and theoretical interpretation clearly show that these states are primarily found close to the Fermi energy. This allows the derivation of guidelines to optimally taylor the electronic structure of alloys, bilayer systems, and nanocatalysts to mimic that of the most successful Pt-based catalyst systems.

CHAPTER V

ALLOYS

As early as 5000 BC, metallic alloys started to play a major technological role, because it was recognized that many desired properties of a material could be created by deliberately melting together two or more metals, and allowing the mass to solidify. The change in chemical environment and configuration of metal atoms also alters the electronic properties of the material, as will be discussed in this chapter. Section 5-1 provides information about the crystal structure of the alloys under study, along with the results of their electrochemical characterization (both performed by our collaborators at ANL). Section 5-2 outlines the sample preparation and leads over to the discussion of the electronic structure of the alloys in Section 5-3. The alloy valence band structure (VBS) will be compared to that of the pure metals (as discussed in Chapter IV), calculated sums of the constituent metal valence bands (VBs), and the theoretical DOS as calculated by our project partners at Caltech. The effects of exposure of the alloy foils to the acidic environment during electrochemical testing will be discussed in detail in Section 5-4. Changes in electronic structure, in particular due to surface segregation, of the alloy foils upon annealing in UHV are presented in Section 5-5. Lastly, the results of this chapter are summarized in Section 5-6.

Section 5-1

Crystal Structure and Electrochemical Activity of the Pd-Cu Alloys

When an alloy is formed, the alloying element can be distributed over the crystal lattice sites of the host structure and yield a solid solution, or it can form different phases showing up as particles in a "matrix" [88]. Alloys can be classified into two categories: ordered alloys and disordered alloys. In the case of disordered alloys, atoms are distributed randomly over the atomic sites (see Fig. 5.1). This mixing of metals on the atomic scale is therefore referred to as a solid solution. For ordered alloys, the atoms show a preference to arrange themselves in an ordered fashion as can be seen in Fig. 5.1 for the ordered $L1_2$ (middle) and $L1_0$ (right) structure. The well-ordered configuration, e.g., the Cu atoms in the $L1_0$ structure, then forms a superlattice which itself gives rise to diffraction peaks in x-ray diffraction (XRD) measurements. The herein studied Pd-Cu alloy foils have been characterized by XRD at ANL. The lattice spacing of the Pd:Cu 1:1 alloy foil exhibited a value 3.757Å, which is close to the average lattice spacing of Pd (3.8902Å) and Cu (3.615Å) [55]. With a lattice constant of 3.618Å, the lattice of the Pd:Cu 1:3 alloy foil was even further contracted, almost reaching the value of pure Cu.
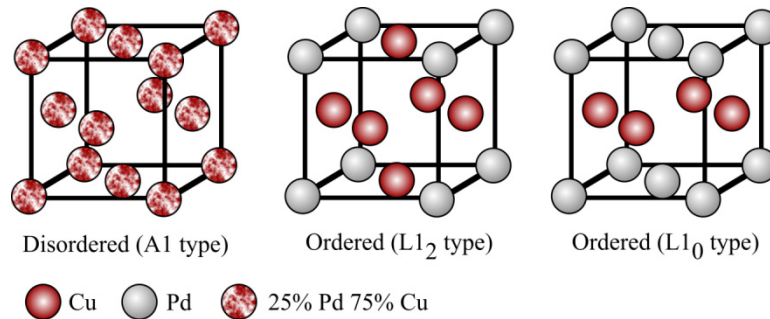
Fig. 5.1: Crystal structures of disordered and ordered Pd-Cu alloys, adapted from [89].

54

No signs of isolated Cu or Pd phases were found in XRD. Both foils showed a face-centered cubic (fcc) structure with no superlattice reflections in the XRD patterns, i.e., they are fcc solid solutions and not ordered alloys [14]. Computational results from our collaborators at Caltech were performed for ordered Pd-Cu alloy systems and favor the $L1_0$ structure for the 1:1 composition and the $L1_2$ structure for the 1:3 ratio.

In addition to the XRD analysis, the foils also underwent electrochemical characterization at ANL. Cyclic voltammetry (CV) in a quiescent oxygen-saturated 0.1M $HClO_4$ solution was used for a qualitative comparison of the ORR activity of the foils.
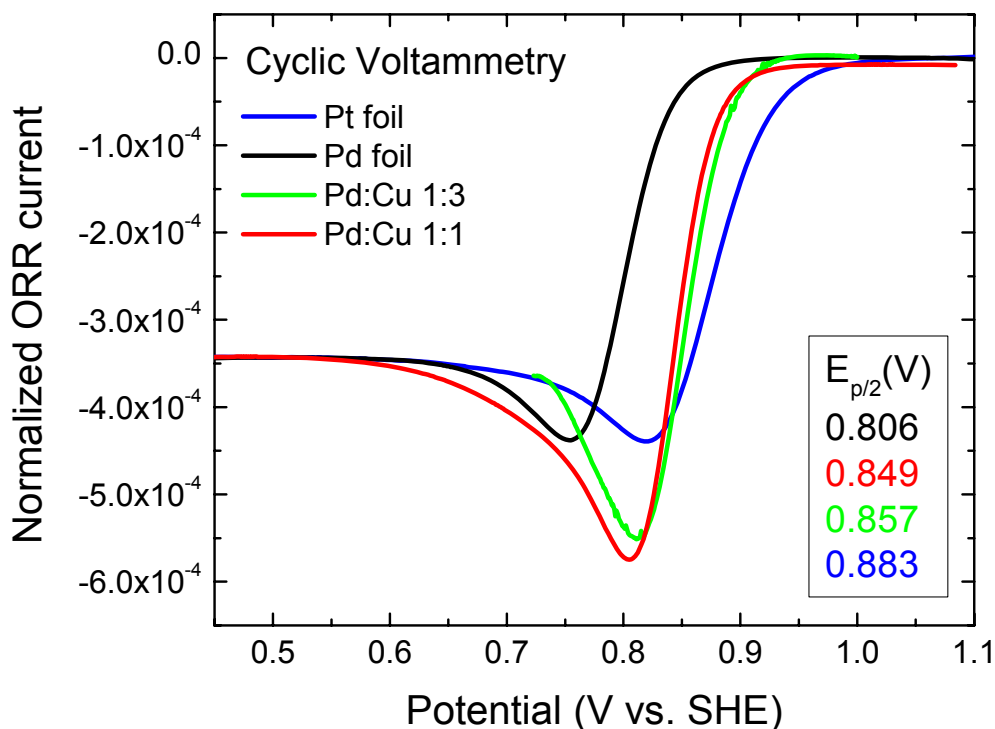
Fig. 5.2: Cyclic voltammograms of pure Pt and Pd foils, as well as two Pd:Cu alloy foils, to derive a qualitative measure of ORR activity. The lower right-hand box gives the half-wave potentials ($E_{p/2}$). It is seen that $E_{p/2}$ for the alloy foils is intermediate between that of Pd and Pt, indicating an enhanced ORR activity of the alloys compared to the pure Pd foil.

Fig. 5.2 shows the CV data, normalized to the diffusion-limited region, and the effective half-wave potentials ($E_{p/2}$) of the Pd:Cu 1:1 and 1:3 alloy foils in comparison with a pure Pd and Pt foil.

As discussed in Chapter III, $E_{p/2}$ provides a qualitative measure of the ORR activity of the foils: the higher $E_{p/2}$, the higher the ORR activity [14]. The higher $E_{p/2}$ value for the alloy foils as compared to the Pd foil is thus direct evidence of their superior ORR activity and indicates that alloy formation is beneficial for an enhanced, deliberately tailored activity.

In the following sections, the electronic structure of the alloy foils will be compared with reference data from pure metal foils and the calculated DOS in order to reveal the electronic changes induced by alloying Pd with Cu and their potential impact on the ORR activity.

Section 5-2

Sample Preparation

The Pd-Cu alloy foils were manufactured by ACI alloys, Inc., using an arc-melting technique [90]. Palladium of 99.95% purity and copper of 99.99+ % purity were used as base materials. XPS survey spectra of the foils in the as-received state not only showed the expected Pd and Cu lines, but also revealed that the surface of the samples was contaminated by carbon- and oxygen-species and to a minor degree by indium (In), zinc (Zn), and tellurium (Te), see Fig. 5.3.
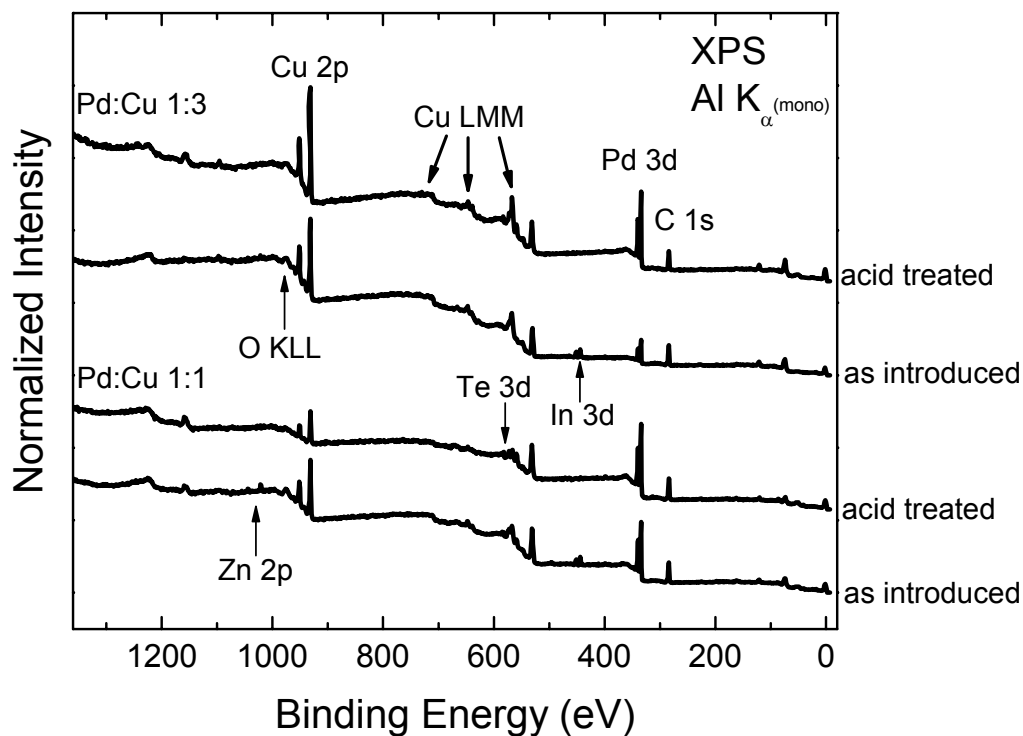
Fig. 5.3: XPS survey spectra of alloy foils before (as introduced) and after acid treatment.

It is most likely that In, Zn, and Te stem from the production and processing of the commercial foils, as these contaminants have not been detected on other samples within the UHV system. In order to measure the intrinsic VB of the alloy foils and not a superposition with contributions of the various contaminants, the alloy foil surfaces were mechanically cleaned with 400-grade sand paper under dry nitrogen atmosphere prior to introduction into UHV. Samples prepared in this way only exhibited a small amount of carbon and oxygen on the surface. Sample cleaning by Ar^+-ion sputtering was avoided because Cu has been found to be sputtered preferentially (compared to Pd) [49, 50], which would ultimately result in Cu depletion on the surface and thus obscure the determination of the pristine VBS.

Section 5-3

Electronic Structure of Pd-Cu Alloys

The VBs of the ground Pd-Cu alloy foils are shown in Fig. 5.4 (solid lines), along with the VB of Pd and Cu metal foils (dashed lines) and a calculated VB, created by the superposition of pure Pd and Cu foil VB spectra in the respective ratios (dotted lines). The VBs of the foils show distinct deviations from each other, the source material (Pd, Cu), and the calculated VB, but agree well with a previously published study on disordered Pd-Cu alloys [91]. They are also in qualitative agreement with the calculated DOS by Caltech that assumes ordered fcc structures and predicts a lower DOS near the Fermi energy for the 1:3 alloy as compared to the 1:1 alloy. Despite the observed differences, the most characteristic features of the alloy VBs coincide with features in the Pd and Cu VB. For the Pd-Cu 1:1 alloy foil, a shoulder at ~1.1 eV (1), a broad peak at ~2.6 eV (2), and a shoulder around 4.2 eV are observed. Most of the intensity at 1.1 eV (1) can be attributed to Pd-like states (most likely from orbitals similar to the d-e_g and d-t_{2g} orbitals in pure Pd, see Fig. 4.7), as the Cu VB has very low intensity close to the Fermi energy. It is noteworthy that the observed intensity close to E_F is much higher than one would expect from adding the Pd and Cu VB in a 1:1 ratio (dotted line). Evaluation of the Cu 2p and Pd 3d XPS line intensities and performance of a quantitative analysis yields a Cu rich surface composition (59% for Cu vs. 41% for Pd, see Table 5.1). The high Pd contribution to the VB, however, might nevertheless indicate a Pd enrichment of the surface layer(s) (keeping the variations in probing depth in mind) - photoelectrons associated with the core-level lines of Cu 2p and Pd 3d are more surface-sensitive (see IMFP curve in Fig. 3.3) due to their lower kinetic energy of ca. 554 eV and 1152 eV,

respectively, as compared to electrons from the VB region with energies around 1482 eV. Hence, it is possible that the VB is overall more Pd-rich than the core-level ratio would lead us to assume.
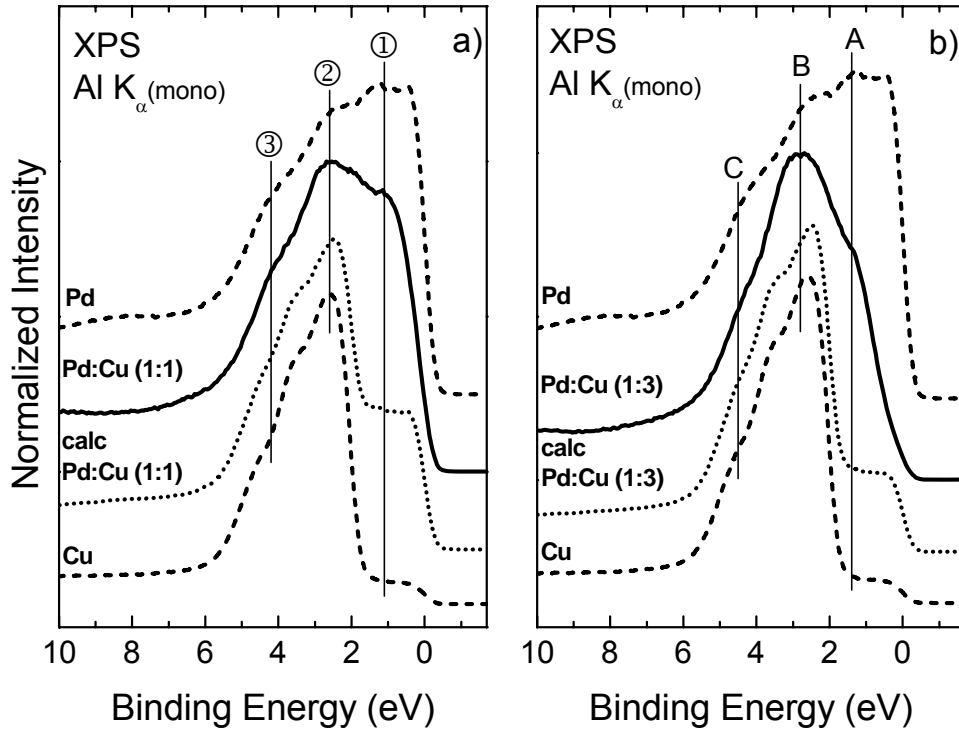
Fig. 5.4: Valence band of a) Pd-Cu (1:1) and b) Pd-Cu (1-3) alloy foils. For comparison, we show the VBs of Pd, Cu, and calculated by adding the pure Pd and Cu foil VBs in the respective ratios.

A quantitative analysis was performed to determine the elemental composition of the samples (the details of the procedure are outlined in detail in Section 3.3). This way, the varying amount of contamination of the acid-treated samples on the surface can be taken into account, which could result in a stronger attenuation of the metal (and all other) peaks under study. Table 5.1 shows the results from the compositional analysis of the four samples.

59

Due to the small amount of Te present on the acid-treated samples (2% or less), its influence on the VB can likely be neglected. Analysis of the Pd:Cu ratios reveals that the initial compositions are slightly Cu rich: 1:1.4 for the nominal Pd:Cu 1:1 foil and 1:4.5 for the nominal Pd:Cu 1:3 foil. After the acid-treatment, the Pd:Cu ratio changes in favor of Pd in both cases, which aids in the interpretation of the core-level shifts and changes in the VBs to be discussed below.

Table 5.1: Compositional analysis of Pd:Cu alloy samples (error bars are ±10%).

Sample	Pd	Cu	C	O	Te	Pd:Cu ratio
Pd:Cu 1:1 ground	30.4%	43.5%	23.6%	2.6%	none	1:1.4
Pd:Cu 1:1 acid treated	21.1%	10.4%	62.0%	4.6%	1.9%	1:0.5
Pd:Cu 1:3 ground	14.5%	65.3%	16.7%	3.5%	none	1:4.5
Pd:Cu 1:3 acid treated	17.1%	31.7%	46.0%	4.3%	0.9%	1:1.9

When comparing the characteristic features in the alloy VBs, one finds that the shoulder in Fig. 5.4 at 2.6 eV seems to arise from both the peak at 2.4 eV found in Pd and the peak in the Cu VB at 2.5 eV. The shoulder around 4.2 eV probably also results from the shoulders found at 4.2 eV in Pd and 4.5 eV in Cu. As one would expect, the VBS of the 1:3 alloy foil is far less intense near the Fermi energy as compared to the 1:1 foil, but still more pronounced than one would assume from the 1:3 VB calculation. As noted above, this might be an indication for Pd enrichment within the first few atomic layers. The characteristic features of the 1:3 VB are a shoulder at ~1.4 eV (A), a broad peak at ~2.8 eV (B), and a shoulder around 4.5 eV (C). The features of the 1:3 foil are similar to the same features in the Pd and Cu VB, as outlined for the 1:1 alloy foil. The main difference between the alloy foils lies in the energy region between E_F and ~2.5 eV, which can be attributed to the different Pd content. For comparison, Fig. 5.5 illustrates

the calculated DOS of an ordered $L1_0$ Pd-Cu 1:1 alloy a) and ordered $L1_2$ Pd-Cu 1:3 alloy

b), obtained from our collaboration partners at Caltech.
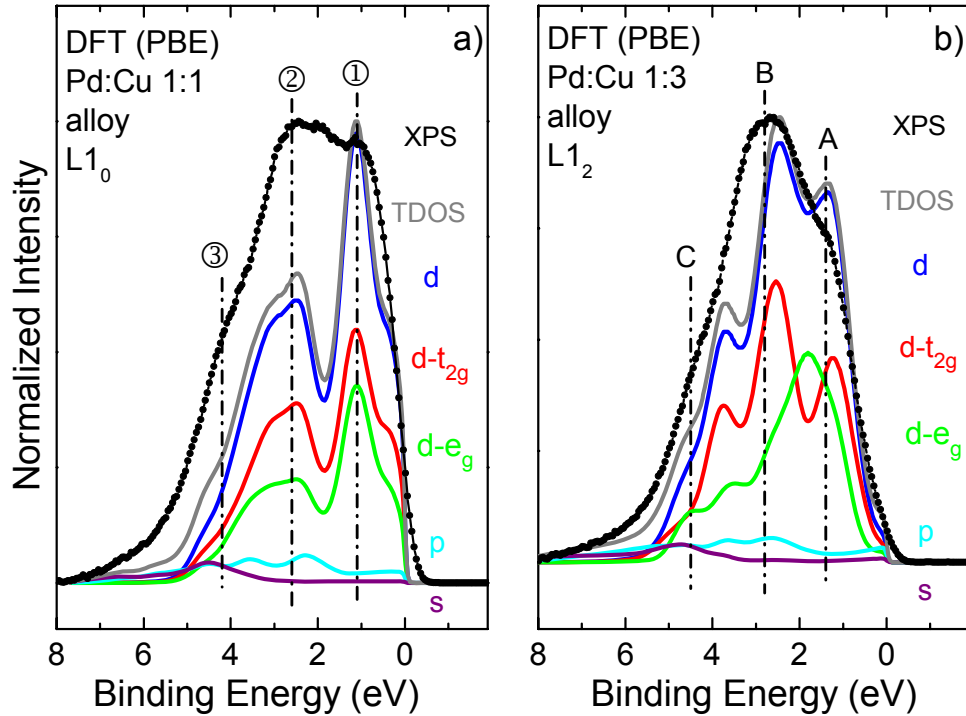
Fig. 5.5: a) Theoretical DOS (broadened) of ordered ($L1_0$) Pd-Cu (1:1) and b) ordered ($L1_2$) Pd-Cu (1-3), in comparison to the XPS valence bands of the disordered Pd-Cu (1:1) and (1:3) alloy foils.

Despite the fact that the theoretical studies assume ordered fcc structures, they are in qualitative agreement with the XPS VB spectra. They predict a lower DOS near the Fermi energy for the 1:3 alloy, as compared to the 1:1 alloy, and exhibit peaks that are in fair agreement with the peaks found in the XPS VBS. The DOS peak intensities are, however, rather different and are, in contrast to the DOS peaks of the pure metal foils, lower in intensity at higher binding energies than observed in XPS. According to a study by Lu et al., this is a common problem among calculations that assume a unique, unrelaxed single-bond length for Cu-Cu, Cu-Pd, and Pd-Pd [92]. When relaxation is

61

introduced, the intensity of the Pd local density of state (LDOS) from the top of the band is distributed toward lower energies near the bottom of the band. Furthermore, calculations by Winter et al. find strong hybridization between the Pd d-band and the Cu d-band, which introduces new states near the bottom of the alloy d-band [93]. Consistent with the results presented in Fig. 5.5, they find that the common d-band moves closer to E_F with increasing Pd concentration.

Section 5-4

Influence of Acid-Treatment on the Electronic Structure

Besides the initial activity of a catalyst, its longevity in the highly acidic Proton Exchange Membrane Fuel Cell (PEMFC) environment is of major importance. In order to gauge the impact of the acidic environment on the electronic structure and composition, the as-received alloy foils (described above) were immersed in a beaker containing 0.1M $HClO_4$ for 1h. The samples were removed from the beaker, rinsed with deionized water, and mounted onto the sample holder under inert conditions in a glove bag filled with dry nitrogen. Through this procedure, contamination due to ambient air was prevented.

As can be seen in Fig. 5.3, the chemical treatment efficiently removes the surface contaminants In and Zn, but fails to significantly reduce carbon and oxygen species (no major change in C 1s and O KLL intensity is found). On the contrary, the Te signal presented in Fig. 5.6 appears even stronger after the acid treatment, suggesting that it is not only present on the surface but also in the (surface-near) bulk of the alloys. This assumption is verified in the annealing study presented in Section 5.4. The Te 3d

lineshape suggests that the majority atoms are incorporated in the metal matrix, while a smaller number of Te atoms is bound in a tellurium oxide environment.
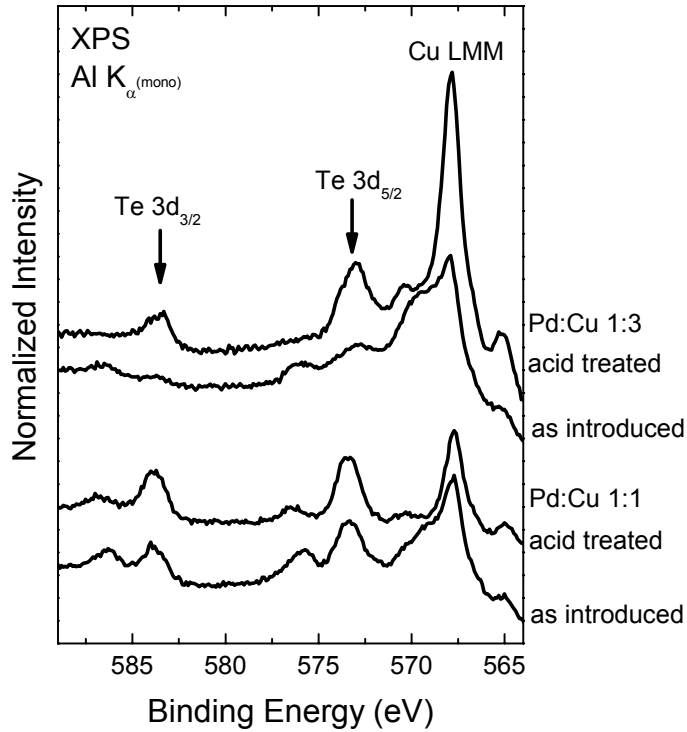
Fig. 5.6: Te 3d signal before and after acid treatment.

The initial Pd and Cu intensities and ratios are also altered by the acid treatment. The following analysis emphasizes the variations of the elemental composition (especially the Pd to Cu ratio) and their implications for the VBS of the alloy foils. In order to avoid the influences of the various (metal) contaminants found in the as-received samples, we compare a mechanically cleaned ("ground") alloy foil to an acid-treated foil (that was not cleaned before acid-treatment) to discuss the impact of the acid-treatment. As all alloy foils stem from the same batch, a similar Pd:Cu ratio throughout the foils can be

assumed. Summarized in Fig. 5.7 are the changes in intensity and chemical environment found for Pd.

Fig. 5.7: XPS detail spectra of the Pd 3d region of the alloy foils after mechanical cleaning and immersion in 0.1M $HClO_4$ for 1h. In graph a), variations of the peak shape can be monitored, while chemical shifts and intensity variations can be followed in b).

Fig. 5.7a focuses on comparing the various peak shapes of the Pd $3d_{3/2}$ peak of the acid-treated samples (dashed curve), ground (i.e., mechanically cleaned) samples (solid line), and pure Pd metal (dotted line). For all cases, pure Pd metal shows the strongest shoulder, which we ascribe to the increased DOS directly at the Fermi energy and the associated enhanced probability for inelastic scattering. When Pd is alloyed this asymmetry is strongly reduced, in parallel with the reduction of the DOS directly at the Fermi energy. While a slight asymmetry is still present for the 1:1 Pd-Cu foil, the Pd 3d peak is almost symmetric for the 1:3 ratio. These findings are in agreement with a study

by Sundaram et al. that also found the Pd peak shape changes from asymmetric to symmetric when Pd concentration(x) is about 0.4 in Pd_xCu_{1-x} alloys [49]. Hüfner et al. correctly ascribed the magnitude of the asymmetry to the DOS at the Fermi energy, because the asymmetry drastically decreases in sputtered Pd which also shows a much lower DOS at E_F [73, 94]. The same effect was reported in a study by Shevchik, where the asymmetry of Pt and Ni core-level lines disappears when they are diluted into cadmium [95]. Since the asymmetry is related to the DOS at the Fermi level, Sundaram et al. conclude that the discontinuity of the asymmetry at x~0.4 reflects the change from d to s electron screening, because the Pd d electrons at the site are localized and the Cu d band is full [49].

Having established the relationship between core-level asymmetry and DOS at the Fermi energy, we can now discuss the Pd 3d peak shape of the acid-treated samples in light of these findings. For both alloy foils, the high binding energy shoulder of Pd $3d_{3/2}$ increases after the acid bath. This could be due to additional chemical components created during the acid treatment or related to a change in Pd:Cu composition which would result in an increase of asymmetry in case of a ratio change in favor of Pd. When comparing the Pd 3d signal intensity before and after the test (Fig. 5.7b), it is found that the Pd intensity increases slightly for the Pd:Cu 1:3 alloy and significantly for the Pd:Cu 1:1 alloy. Likewise the VB structure of both alloys shows more intensity near the Fermi energy after the acid-treatment (see discussion of Fig. 5.9 below). Thus, the observed asymmetry can be interpreted as being due to the enrichment of Pd after the acid-treatment.

In addition to the mentioned intensity variations, Fig. 5.7b) also shows changes in peak position upon acid-treatment relative to the peak center of the "ground" sample. While the +0.05 eV shift in peak center of the acid-treated 1:1 foil (as compared to the peak center of the "ground" 1:1 alloy) lies well within the error of the measurement and is therefore not unambiguous, the shift in 1:3 alloy foil of about 0.1 eV towards lower binding energies is most likely a real effect related to the change in Pd composition during the course of the acid bath. Mårtensson et al. have shown that the Pd 3d peak shifts towards higher binding energies upon alloying with Cu [91]. This trend can also be seen in Fig. 5.7b for the ground alloy foils. The study by Mårtensson et al. found that the lesser the Pd content the higher the observed peak shift (up to 0.8 eV for ~7 atomic % Pd). Applied to our observation of a slightly negative peak shift for the 1:3 alloy after acid treatment, the peak shift indicates an increase in Pd content which agrees well with the increase of the Pd 3d intensity, its asymmetry, and the spectral changes in the VB (see Fig. 5.9 below). In contrast to Pd, the core level asymmetry of pure Cu is very low (as can be seen in Fig. 5.8 and [67]) and does not change perceivably for the "ground" or acid-treated alloy foils. Instead, we find a slight increase of intensity at the high binding energy shoulder of the Cu $2p_{3/2}$ peak (indicative of Cu(I)), and a broad satellite (indicative of Cu(II)) around ~11 eV after the acid treatment. Both point towards the formation of Cu compounds of higher oxidation states. Fig. 5.8b) reveals that the Cu signal of both alloy foils decreases strongly after exposure to the acidic environment.
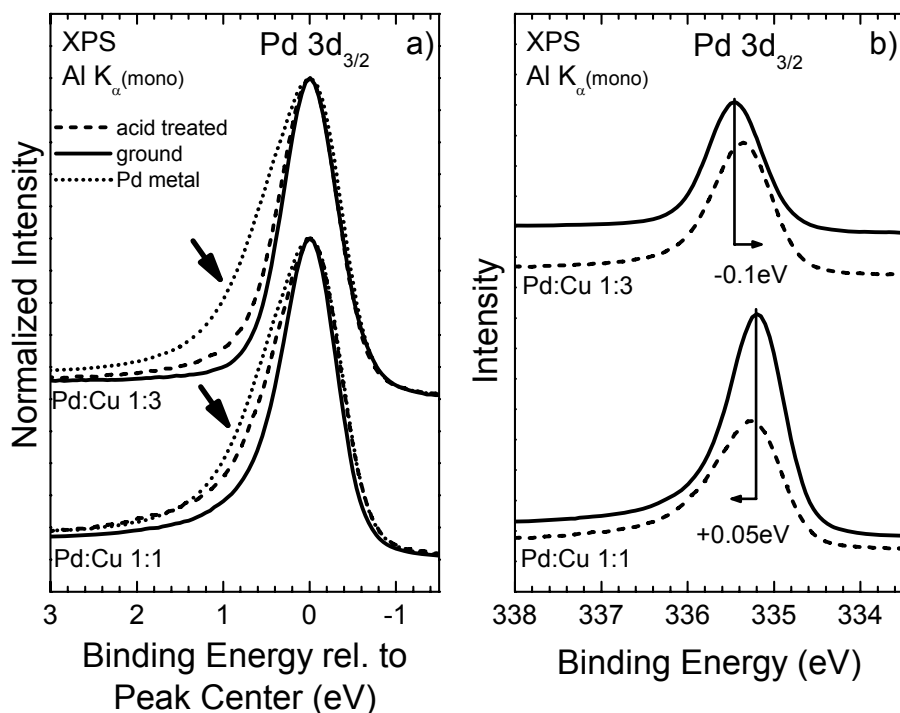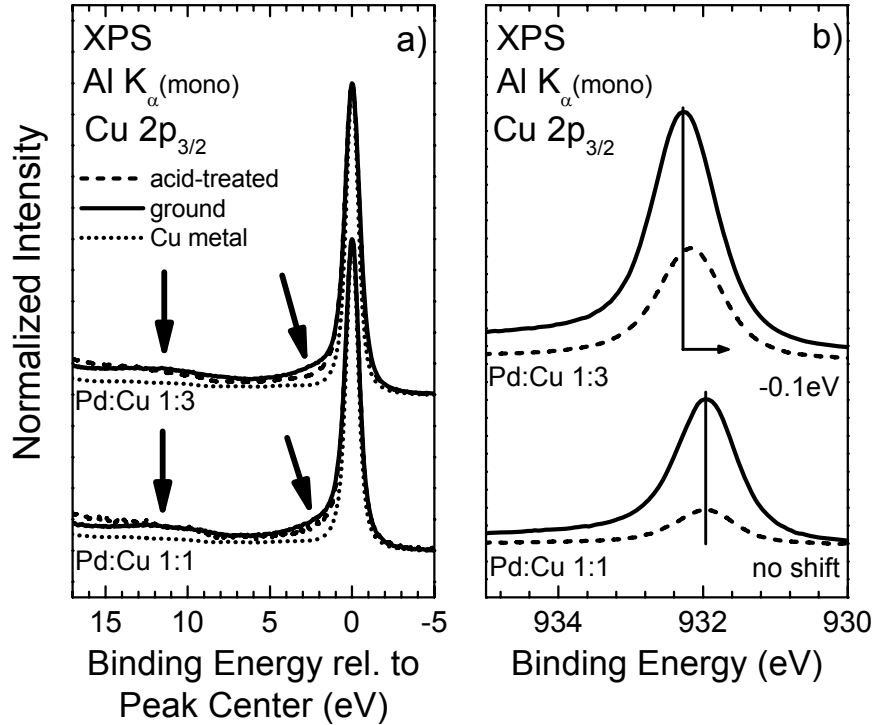
Fig. 5.8: XPS detail spectra of the Cu 2p region of the alloy foils after mechanical cleaning ("ground") and immersion in 0.1M $HClO_4$ for 1h. Variations of the peak shape can be monitored in a), while chemical shifts and intensity variations can be followed in b).

For the 1:1 alloy foil, the peak position is found to be constant, while the 1:3 alloy foil shows a slight shift of 0.1 eV towards lower binding energies. Referring back to the study by Mårtensson et al. [91] quoted earlier, this is a further indication for the preferential leaching of Cu during acid treatment that results in Pd-enrichment of the surface layers. In addition to the core-level changes of Pd and Cu discussed above, the VBS in Fig. 5.9 provide a visual representation of the Pd-enrichment. The 1:1 alloy and especially the 1:3 alloy VBs exhibit a distinct increase in intensity at the Fermi energy that must be directly related to an enhancement of Pd on the surface.
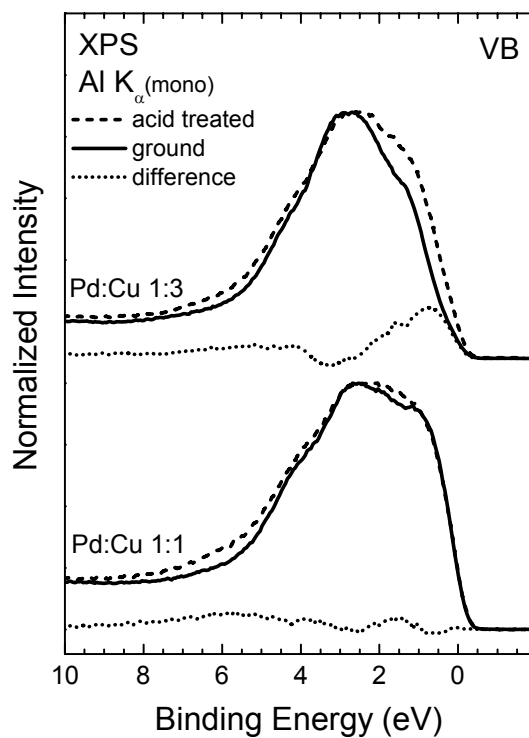
Fig. 5.9: XPS valence band of the Pd:Cu 1:3 alloy foil (top) and Pd:Cu 1:1 alloy foil (bottom) after mechanical cleaning ("ground", solid line) and after acid treatment (dashed line), together with their difference spectra (dotted line) to emphasize the spectral changes.

The CV curve shown in Fig. 5.2 is most comparable to the VB of the acid-treated alloy foils, as it was acquired under the same experimental conditions (after 1h exposure to 0.1M $HClO_4$). Comparison of the acid-treated VBs among each other reveals a closer resemblance than the "ground" samples, which in turn explains the very similar results of ORR activity (since the 1:3 sample will have lost a significant amount of Cu from the surface before the actual ORR measurement). This illustrates that the measurement of the ORR activity of a true Pd:Cu 1:3 ratio requires the electrochemical characterization to be performed almost immediately after exposure to the acidic testing environment.

Section 5-5

Influence of Annealing on the Electronic Structure

In this section, the possibility of surface enrichment of Pd or Cu through annealing was investigated. It is generally known that the chemical composition at the surface differs from the bulk ratio for certain alloys, i.e., that one of the alloy components may be enriched at the surface (commonly referred to as surface segregation) [28]. As explained in Chapter II, the choice of Pd and Cu as noble- and base-metal was initially guided by surface segregation energies calculated by Ruban et al. [28], which indicate a moderate propensity of Pd to segregate in the presence of Cu. In order to test this theory, the Pd:Cu 1:1 and 1:3 alloy foils were annealed for 1h in UHV at temperatures up to 934°C and then measured after cool-down at room temperature (RT).

If surface segregation of Pd takes place, one would expect a pronounced attenuation of the Cu signal and an increase of the Pd signal. This should be most pronounced for the Cu 2p signal, as it is most surface-sensitive. In order to assess the intensity variation of Cu relative to Pd, the Cu $2p_{3/2}$ intensity was evaluated and normalized to the integrated Pd $3d_{5/2}$ area of each sample. The result is shown in Fig. 5.10a, together with an analysis of the observed core level shifts in Fig. 5.10b.

For the Pd:Cu 1:1 foil, the Cu intensity first increases (up to 270 °C), i.e., hinting towards a slight Cu surface enrichment, then abruptly decreases after annealing at 405 °C, and increases again (slightly) after annealing at higher temperatures. The pronounced change in concentration for the 1:1 alloy after annealing at 405°C and 532°C is accompanied by a significant shift of the Cu 2p core level to lower binding energies and a

strongly modified VB (see discussion of Fig. 5.11b below). This could be due to a disorder-order transition as discussed later in this section.

In the case of the Pd:Cu 1:3 foil, the Cu intensity also first increases for lower temperatures and then decreases for higher temperatures, but never falls below the initial value at RT.
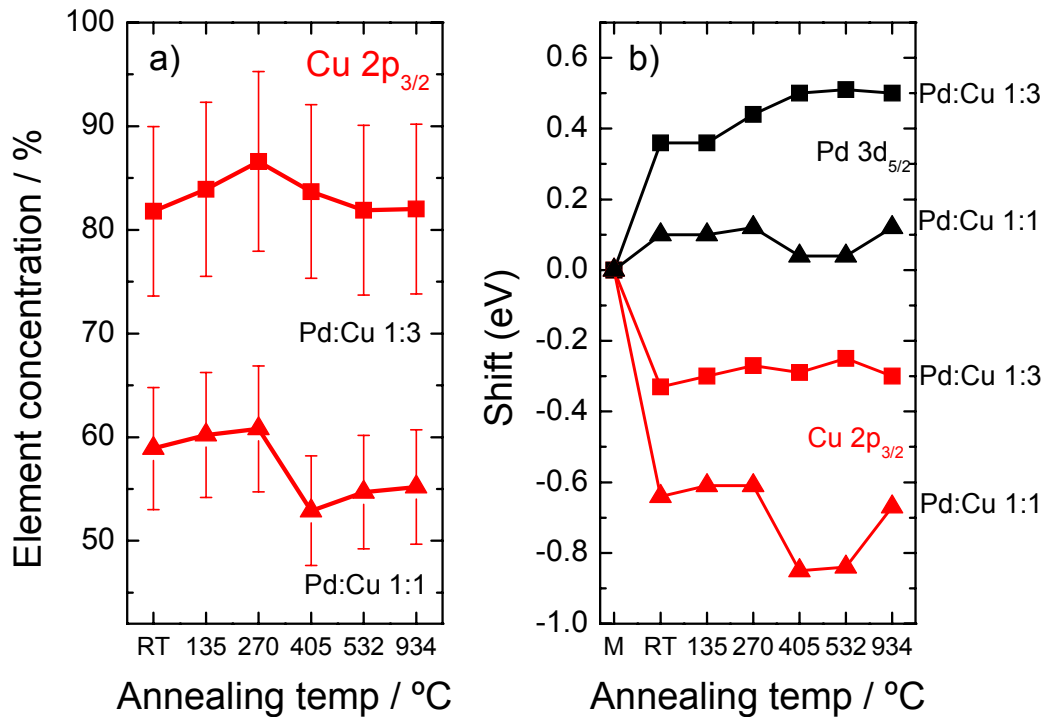
Fig. 5.10: a) Variation in Cu concentration of alloy foils as a function of annealing temperature (RT = room temperature). b) Relative energy shift of Pd and Cu core levels versus annealing temperature, referenced to the value for the pure metals (M).

As mentioned, Fig. 5.10b) depicts the peak shifts of the Pd $3d_{5/2}$ and Cu $2p_{3/2}$ core-levels after the various annealing steps (referenced to the binding energy of the core levels in the pure metals). It is evident that all alloy samples exhibit modified core level positions compared to the pure metal references, and that only rather minor shifts are observed with increasing annealing temperature (with the exception of the 405°C and

532°C annealing steps of the 1:1 alloy). Again, we speculate that this exception might be due to a disorder-order transition, to be discussed below.
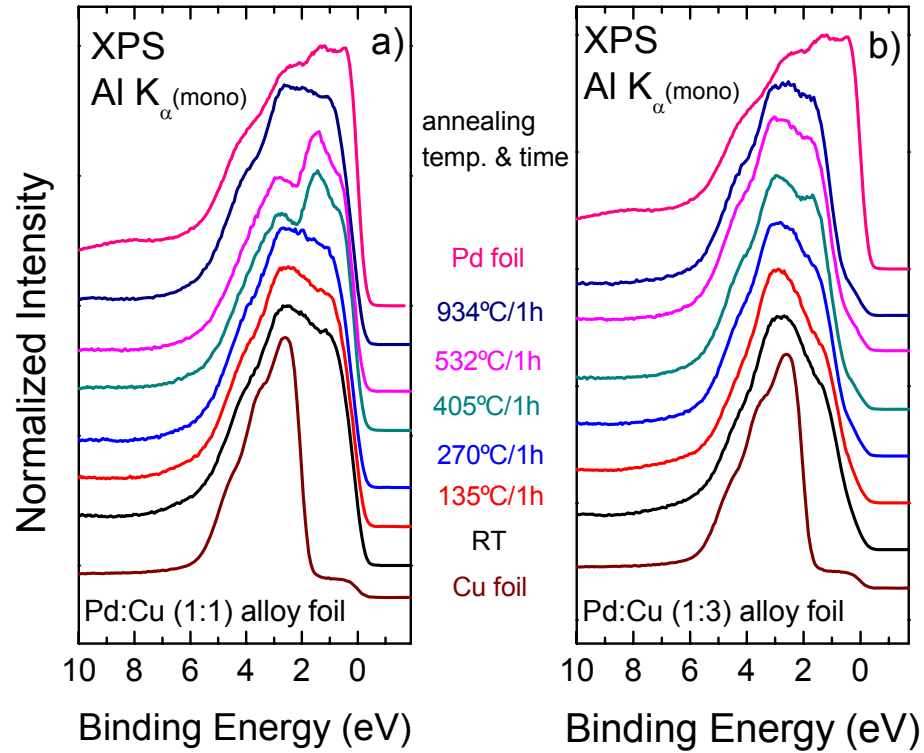
Fig. 5.11: XPS valence band spectra of a) Pd:Cu 1:1 and b) Pd:Cu 1:3 upon annealing.

Aside from the core-level studies, the changes in the VBs of the alloy foils give valuable information about the various processes occurring during annealing. The VB spectra are presented in Fig. 5.11. The VB of the 1:1 alloy does not change significantly upon annealing up to temperatures of 270°C. As mentioned earlier, it changes significantly after annealing to 405 °C and 532 °C. This change, which entails the most pronounced core-level shifts, could be an indication of a change in crystal structure. According to the Pd-Cu phase diagram published in [96], a Pd:Cu solid solution with an

element ratio in the range of 35-50 at.% Pd can undergo a transformation from a disordered Pd-Cu solid solution to an ordered CsCl-type (body-centered cubic structure where one atom of one sort sits in the base structure surrounded by eight atoms of the other kind). According to the phase diagram, the onset of this transformation occurs at temperatures of about 260 °C. Beyond 600 °C, the crystal structure reverts to a disordered solid solution [96]. This is consistent with the XPS results, namely that the VB is unchanged when the sample is annealed at 270 °C, shows strong variations when annealed at 405 °C and 532 °C, and becomes similar to its original structure (before annealing) when annealed at 934 °C.

The VBS of the Pd-Cu 1:3 alloy, on the other hand, slightly loses intensity near E_F after the first heat treatment at 135°C. The subsequent annealing steps restore and further increase the spectral intensity at E_F. For the VB after the 405°C treatment, a broad peak emerges at ~1.7 eV, and becomes stronger and broader for the last two treatments. These changes are possibly due to ordering of the crystal structure and could indicate the formation of a long-period superlattice [96]. In order to verify the formation of a CsCl structure in the 1:1 alloy and to shed more light on a possible ordering process in the 1:3 alloy, XRD studies are needed.

Section 5-6

Summary and Conclusions

In summary, the electronic structure of disordered Pd-Cu alloys was studied before and after acid- and heat-treatments. The results of electrochemical testing demonstrated a superior ORR activity of the alloy foils as compared to pure Pd. The alloy foils were

investigated by XPS and showed a unique VB structure that cannot be described by a simple superposition of Pd and Cu VBs. The Pd:Cu 1:1 VB exhibits more intensity near E_F as compared to Pd:Cu 1:3, in agreement with the theoretical DOS calculations. Acid-treatment leads to leaching of both metals with a preferential release of Cu. This leads to an increase in the Pd:Cu ratio, which is evidenced not only by the increased intensity of the core-levels, but also by the more Pd-like VB, the increase in Pd asymmetry, and the core-level shifts. These results are also in good agreement with the observed ORR activities, which are performed in the same acidic environment as the here-described leaching experiments.

Contrary to theoretical predictions, annealing of the alloy foils does not lead to a significant Pd enrichment on the surface, but rather (presumably) leads to changes of the alloy structure. For the Pd:Cu 1:1 alloy, distinct VB changes above annealing temperatures of 400°C suggest a change to the CsCl structure. This change is accompanied by an increase of the Pd intensity by ~5%. Further experiments would be necessary to find out if these effects are beneficial for the ORR activity. Overall, when excluding the effects of changes in the alloy structure, no evidence for Pd surface segregation was found, in agreement with a study on Pd-Cu alloys by K. Christmann [97].

CHAPTER VI

THIN FILM BIMETALLIC SYSTEMS

Model systems consisting of thin Pd (Cu) metal films deposited in-situ under ultra high vacuum (UHV) onto polycrystalline Cu (Pd) metal foils have been studied to gain deeper insight into the electronic changes occurring when Pd and Cu are brought together. The results of Pd thin films deposited on Cu at room temperature are discussed in Section 6-1. The following annealing study presented in Section 6-2 focuses on the modification of the electronic structure and morphological changes upon alloy formation. Section 6-3 and Section 6-4 are structured analog to 6-1 and 6-2, but examine the deposition of Cu thin films onto a Pd foil and the implications of heat treatment.

Section 6-1

Pd Deposition on Cu – Electronic Structure and Morphology

In this section we present the results from a deposition series of Pd thin films onto a sputter-cleaned Cu-foil. The employed techniques of e-beam evaporation for deposition and Ar^+-ion sputtering for surface cleaning are described in Chapter III. The study's purpose is to elucidate the electronic interaction when Pd atoms are deposited on a Cu substrate. In particular the changes occurring in the core levels and the valence band (VB) are examined. The relationship to the VBs of pure metal and alloy foils will be presented. Pd thin films of various thicknesses ranging from sub-monolayers to several nm were deposited onto a clean Cu foil. Table 6.1 displays the deposition parameters used and links them to the resulting "effective" Pd layer thickness.

Table 6.1: Deposition parameters and layer thickness of Pd thin films on Cu.

deposition	flux rate/nA	deposition time	layer thickness/nm
1	2.75	10 min	0.2
2	10.2	10 min	0.8
3	20.2	10 min	1.9
4	20.0	10 min	2.8
5	20.0	20 min	4.5
6	100.0	20 min	7.0
7	336.0	10 min	7.4

The gradual growth of Pd on Cu with deposition time can be followed by the increasing core-level (Pd 3d, Pd 3p) and Auger (Pd MVV) line intensities in the XPS survey spectra shown in Fig. 6.1. At the same time, the Cu bulk PES signal represented by the Cu 2p and Cu LMM Auger line decrease due to the attenuation caused by the Pd overlayer. The dotted lines indicate the common binding energy positions of the C 1s and O 1s that, if present, would indicate surface contamination (but are absent here).
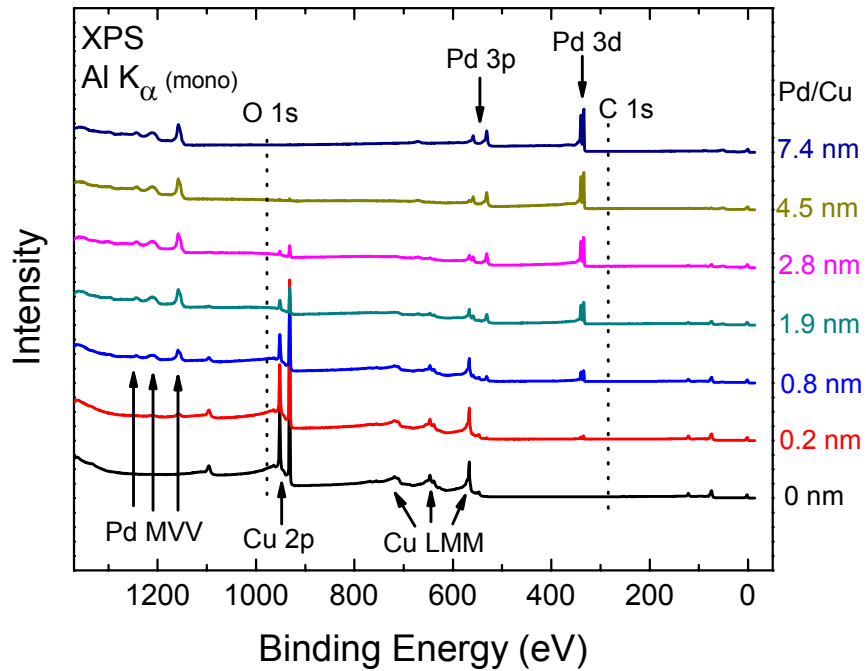
Fig. 6.1: XPS survey spectra taken after various Pd deposition steps onto Cu.
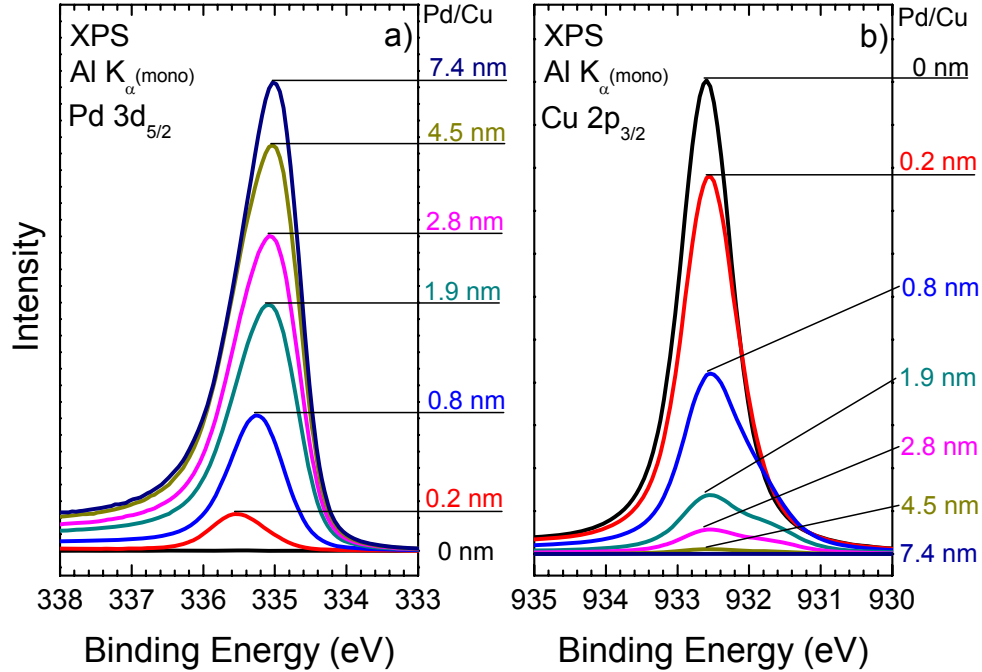
Fig. 6.2: a) XPS core-level spectra depicting the growth of the Pd $3d_{5/2}$ core-level while the simultaneous decrease in Cu 2p intensity is shown in b).

The exact evolution of the Pd and Cu core level intensity is shown in Fig. 6.2. With increasing deposition time the Pd $3d_{5/2}$ line in Fig. 6.2a increases in intensity, while, in parallel, we find a gradual decrease in Cu $2p_{3/2}$ intensity (Fig. 6.2b). The layer thickness was calculated using the attenuation of the Cu $2p_{3/2}$ photoemission line (Fig. 6.2b), an inelastic mean free path (IMFP) of $\lambda=1.074$ nm (at 554 eV kinetic energy) [98], and Eq. 4 in Chapter III (which gives the correct film thickness for a homogenous layer-by-layer growth, and an "effective" film thickness for an island-type growth). Fig. 6.3 shows the data used for this analysis. We find a signal attenuation that can be described by a single exponential decay, allowing a direct determination of the effective film thickness of the Pd overlayer.
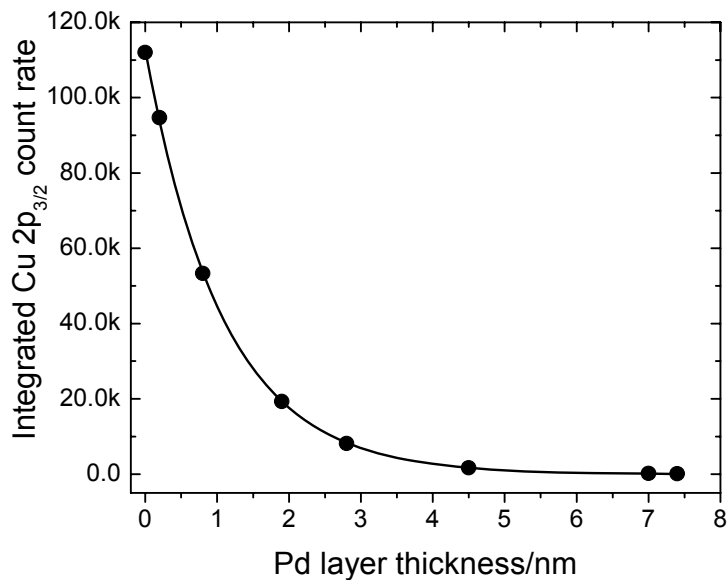
Fig. 6.3: Exponential decay of Cu $2p_{3/2}$ peak intensity as a function of Pd layer thickness.

Fig. 6.4 shows Cu $2p_{3/2}$ (a) and Pd $3d_{5/2}$ (b) core levels, normalized to the peak maximum and aligned to the individual peak centers to elucidate changes in the chemical environment. Upon deposition of Pd, the Cu 2p line develops a distinct shoulder at lower binding energies that reaches a constant intensity above a Pd layer thickness of about 1.9 nm. While the main peak is representative for the Cu atoms in the bulk and uncovered surface of the substrate, the shoulder apparently describes the chemical environment of the Cu atoms in the interface region between the Cu bulk and the Pd adlayer. Thus, the observation of the interfacial shoulder and its saturation above 1.9 nm layer thickness indicates that the first complete Pd overlayer is formed at this effective film thickness.

The Pd $3d_{5/2}$ peak shape shows an asymmetry at higher binding energy, as described in the previous chapter, and apparently exhibits a strong increase in asymmetry once the vicinity of the deposited Pd atoms becomes Pd rich. The degree of asymmetry of pure Pd metal (dotted line in Fig. 6.4b) is reached between 1.9 nm and 4.5 nm, again suggesting island-type growth below 1.9 nm.
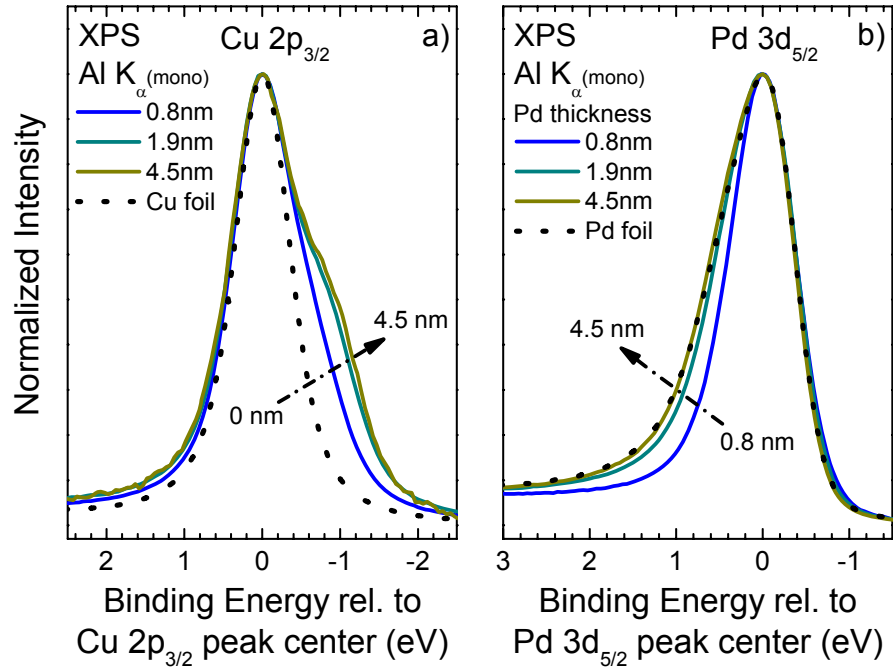
Fig. 6.4: XPS detail spectra of a) Cu 2p$_{3/2}$ and b) Pd 3d$_{5/2}$ core-levels, normalized to the peak maximum. The spectra show the formation of an interfacial Cu species and the increasing asymmetry of the Pd 3d line with increasing Pd thickness.
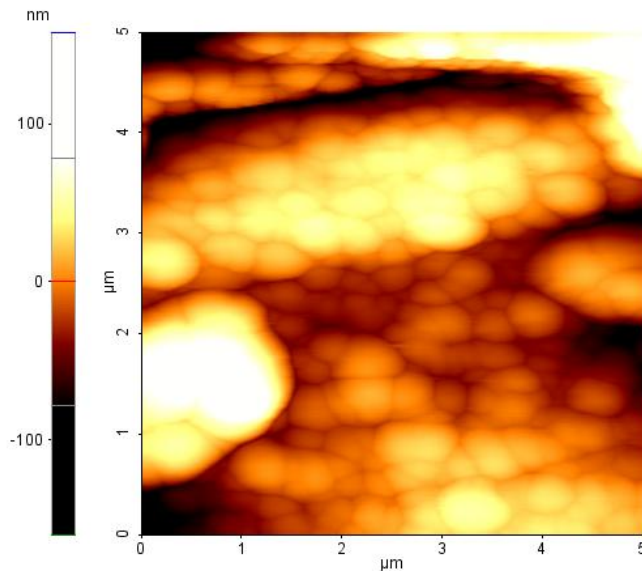
Fig. 6.5: AFM image of a 4.7 nm Pd film deposited on a Cu foil at RT, showing Pd islands forming a closed layer on the Cu substrate.

To ascertain the model of an island-type growth start, we have investigated a sample that was grown in the same way as the Pd/Cu thin film discussed above, using atomic force microscopy (AFM). The result is shown in Fig. 6.5 and clearly suggests an island-like structure of the Pd overlayer. These results are in agreement with an STM study of Pd growth on Cu(111), which found that Pd nucleates on brims, terraces, and islands [99].

We now discuss the observed changes in the VB when Pd is deposited on the Cu substrate. While the VB spectra in the range of 2.5eV – 5.5eV in Fig. 6.6a do not change significantly in shape, pronounced spectral changes can be observed between E_F and ~2.5eV as a function of Pd deposition.
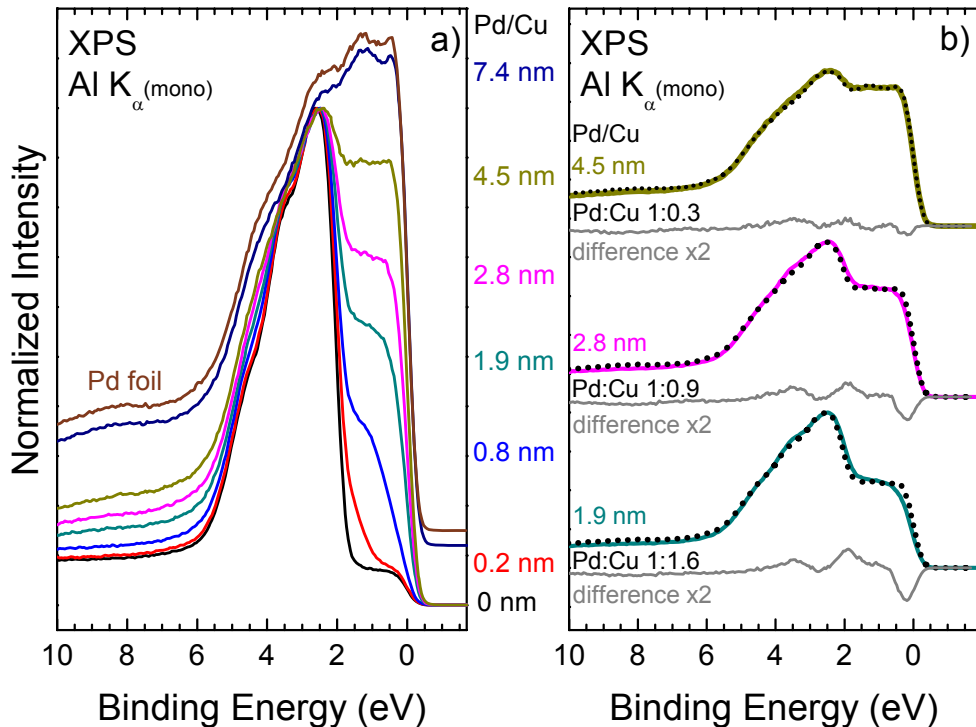
Fig. 6.6: a) Evolution of the Cu VB with Pd deposition. b) Comparison of XPS (solid lines), superimposed valence bands (dotted lines), and their difference (black solid line).

As expected, the Pd d-band states continuously fill up this region until the VB resembles that of the Pd reference foil (compare the 7.4 nm Pd/Cu and Pd foil spectra in Fig. 6.6a.

We find that the bimetallic VB stays within the energy range of the pure Pd and Cu VBs and appears to be a simple superposition of the two. To investigate this hypothesis, we have attempted to match the experimental VB spectra by adding reference spectra of Pd and Cu metal foils with suitable weight factors. The success of this approach is displayed in Fig. 6.6b, which exemplarily demonstrates the analysis for the VB spectra of 1.9 nm, 2.8 nm, and 4.5 nm Pd on Cu. As is shown, these spectra can be reproduced as superpositions of the Pd and Cu VB in the ratio of 1:1.6, 1:0.9, and 1:0.3, respectively. The difference spectra (grey solid lines) between the experimental VB spectra (dotted lines) and the calculated superpositions (black solid lines) reveal a good agreement throughout the spectra, which even improve with Pd thickness. The most pronounced differences are found in the energy region near E_F (~0.2 eV), where the experimental VB spectrum shows less intensity, and around 1.9 eV, where the experimental spectra show slightly more intensity. The minor variations observed most likely date from the altered electronic structure of the interface region, which is expected to more closely resemble that of a Pd-Cu alloy. This would also explain why the observed differences abate at higher Pd thickness. The fact that the bimetallic VBs can be described in such good detail by superposition suggest that, apart from the interface region, little to no modification of the individual Pd and Cu electronic structure is taking place.

As stated in the previous chapter, alloying significantly improves the ORR activity of Pd-Cu. This process is obviously not spontaneous and requires the system to overcome an

activation barrier. The following section will thus examine the impact of annealing on the Pd-Cu bimetallic system.

Section 6-2

Pd Deposition on Cu – Influence of Annealing

In order to facilitate the alloying of Pd and Cu, the bimetallic system discussed in Section 6-1 was annealed under UHV at various temperatures. For all samples the temperature was ramped until the set point given in Table 6.2 was reached and then held constant for the indicated amount of time. As mentioned in Chapter III, the actual sample temperature is higher than that recorded at the thermocouple. The sample temperature denoted in Table 6.2 is thus the maximal temperature read by the thermocouple mounted on the manipulator head, adjusted by a linear correction function. After annealing, samples were allowed to cool down to room temperature prior to XPS analysis.

Table 6.2 Annealing parameters of Pd deposited on Cu substrate

annealing step	time at setpoint/h	setpoint/°C	sample temperature/°C
1	1.75	150	200 ± 50
2	1	300	400 ± 50
3	1	450	600 ± 30
4	1	600	800 ± 30

The most striking effect after the first annealing step is the consolidation of the previously discussed two Cu species (Cu bulk and Cu at the Pd/Cu interface) into a single Cu $2p_{3/2}$ peak (Fig. 6.7a) and a substantial shift to lower binding energy (as indicated by the short black lines in Fig. 6.7b). This suggests that the previously dominant Cu bulk species becomes a minority species, and that the Cu species associated with Cu-Pd bonds

becomes dominant. This suggests that the Pd islands on the Cu substrate change morphology on the surface upon annealing, which is characterized by an increased number of Cu atoms in a Pd-containing environment.
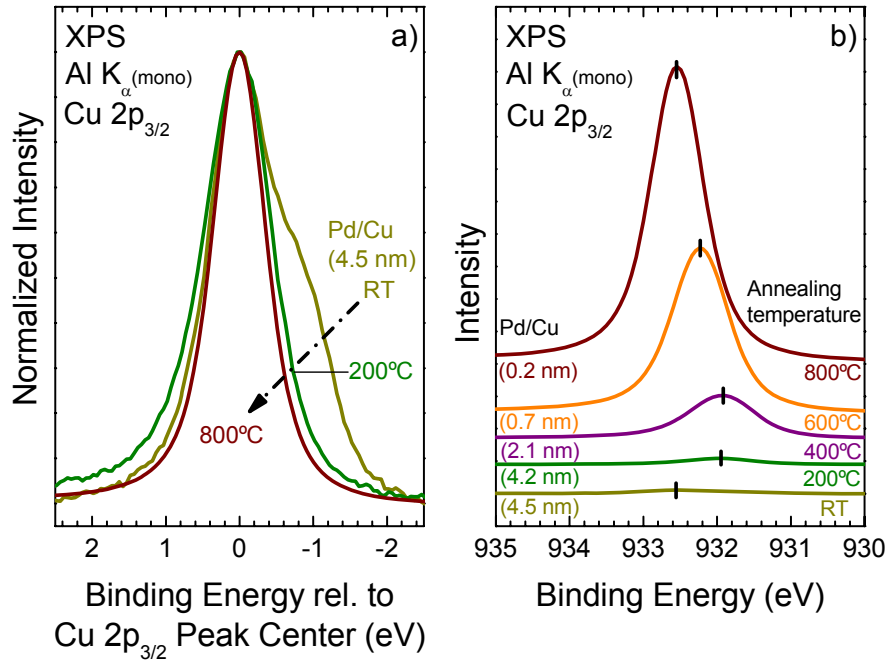
Fig. 6.7: Cu $2p_{3/2}$ core-level of Pd/Cu thin-film normalized to peak maximum to emphasize chemical changes with respect to a) annealing temperature and b) normalized to measurement time as a function of annealing temperature. The nominal Pd/Cu layer thicknesses are given in parentheses as reference.

At higher annealing temperatures (400°C and above), the Cu $2p_{3/2}$ intensity increases significantly (Fig. 6.7b). At 600°C and above, the line position furthermore shifts back towards higher binding energies. In agreement with the room-temperature Pd deposition series, in which an additional shoulder formed due to Cu-Pd interactions, we speculate that the annealing series can also be described as a superposition of bulk-like Cu atoms and Cu atoms in a Pd-containing environment, and that the relative abundance of the latter significantly decreases after annealing at high temperatures.
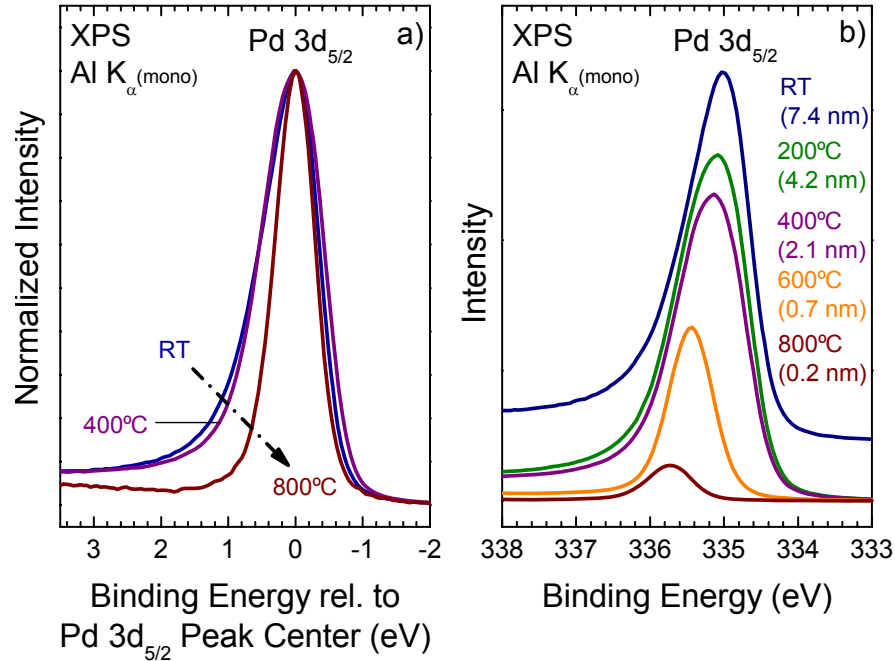
Fig. 6.8: a) Variation of Pd $3d_{5/2}$ line shape and b) intensity and line position with annealing temperature. The nominal Pd/Cu layer thicknesses are given in parentheses as reference.

The Pd 3d line shape as depicted in Fig. 6.8a furthermore supports this picture as the asymmetry of Pd is greatly diminished at 600 and 800°C. The Pd 3d peak slowly shifts towards higher binding energies over the course of the annealing steps. The most pronounced shifts (~0.3 eV) occur after the treatment at 600 and 800 °C (Fig. 6.8b). As can be seen from the intensity and nominal layer thickness of 0.7 and 0.2 nm, respectively, most of the Pd is removed from the surface at this point, either by evaporation or by diffusion in the bulk (which will be discussed in detail below). As in the case of the Cu core levels, we speculate that the Pd line shape can be described by two components, namely Pd atoms in a Pd metal environment (dominant in the RT spectrum), and Pd atoms in a Cu-containing environment (dominant in the 800 °C spectrum).
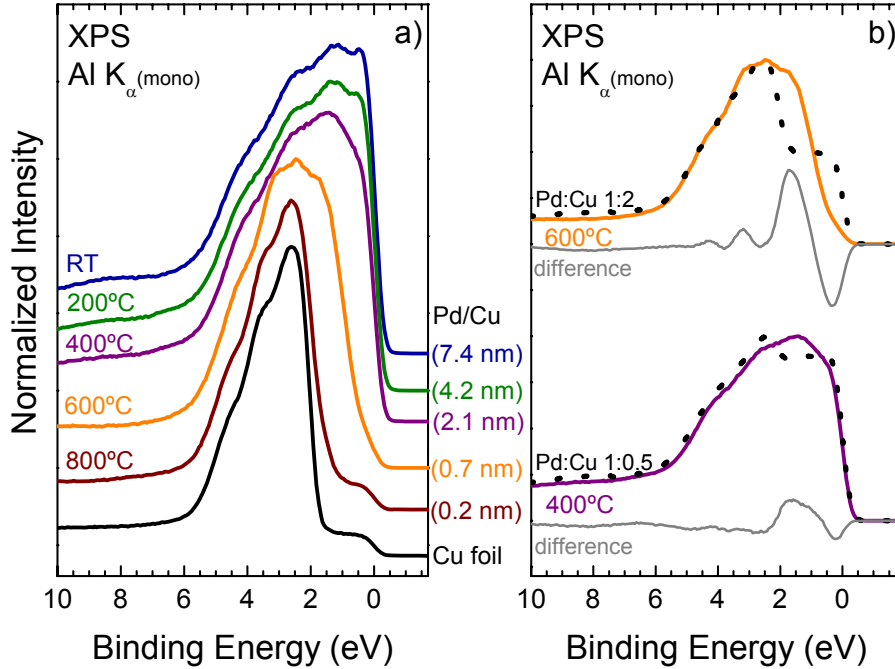
Fig. 6.9: a) Evolution of valence band structure of Pd-Cu thin-film with annealing temperature. b) Comparison of superimposed (dotted lines) and experimental valence bands (solid) lines. The difference spectra are plotted as gray lines. The nominal Pd/Cu layer thicknesses are given in parentheses as reference.

Lastly, the VB as a function of annealing temperature is presented in Fig. 6.9a. At 600 °C and above, the VB shows a strong decline of intensity near E_F and becomes comparable to pure Cu at 800 °C (albeit with some minor contributions from Pd, in agreement with the intensity and position of the Pd $3d_{5/2}$ peak discussed above). This again points towards a removal of Pd from the surface.

The continuous increase of the overall Cu $2p_{3/2}$ intensity, the decrease of the Pd $3d_{5/2}$ intensity, and the reduction of spectral weight near the Fermi energy in the VB spectra could be due to intermixing of Pd and Cu (i.e., the diffusion of Pd into the Cu bulk), Pd desorption from the surface, and/or the formation of Pd islands (dewetting of the Pd cover layer). The latter is in contradiction to the observed VB spectra after annealing at high temperatures, because we find a clear indication for the formation of an alloy. As

84

shown in Fig. 6.9a, annealing at 200 °C results in a VBS very closely related to the one at RT (but with a slight decline in intensity at E_F). In contrast, the VBS found at 400°C and 600°C clearly differ from the VB of the pure metals. Both cannot be described by simple superpositions of Pd and Cu VBs, as demonstrated exemplarily in Fig. 6.9b. Apparently, an alloy is formed, exhibiting a modified VBS, similar to our findings for the alloy foils in Chapter V.

Due to the high Pd melting point of 1554.8°C [55] and relatively low vapor pressure (e.g., $8.27 \cdot 10^{-9}$ Pa at 1000 K (727 °C) [55]), Pd desorption is also not considered to be the major cause of the increase in Cu intensity and the reduction of the Pd signal, even at the elevated annealing temperatures of 600 and 800°C.

Thus, all experimental evidence suggests that, upon annealing, Pd diffuses into the Cu bulk at higher temperatures, forming an alloy. This explains both the peak shift and intensity behavior of Cu $2p_{3/2}$ and Pd $3d_{5/2}$ as well as the observed changes in the VBS – with increasing annealing temperature, the Cu intensity increases and the line shifts towards the metallic position, while the Pd intensity decreases and shifts away from the metallic position towards the presumed alloy position. Likewise, the VBS changes from a (metallic)Pd-like structure to a (metallic) Cu-like structure with some residual Pd contribution, with intermediate VB spectra clearly resembling those of the alloy foils (and failing to be explained by a simple superposition of Cu and Pd VB spectra).

At an above 400 °C, the VBS changes are most pronounced, which suggests a lower temperature boundary between 200 °C and 400 °C to initiate the in-diffusion of Pd. A study by Aaen et al. [99] on submonolayer growth of Pd on Cu(111) revealed signs of the formation of a surface alloy upon heating to ~160°C. Further experiments would be

needed to find the temperature region upon which alloying sets it. Nevertheless, it is clear that the Pd:Cu surface ratio can be modified by variation of the annealing temperature. Annealing of the Pd/Cu bimetallic sample at 400°C results in a Pd-dominated VBS, while heat treatment at 600°C results in a strong increase in Cu surface content and leads to a more Cu-like VB. Therefore, it should be possible to tailor the surface electronic structure of alloys deliberately by choosing a specific annealing temperature. When combined with electrochemical characterization, a link between the observed ORR activity and the electronic structure and therefore the finding of an ideal VBS for the Pd/Cu system becomes feasible.

Section 6-3

Cu Deposition on Pd – Electronic Structure and Morphology

In this section, the "reverse" case of Cu thin films deposited onto a sputter-cleaned polycrystalline Pd substrate is described. In addition to examining the electronic interaction when Cu is deposited on Pd, the study was also performed to identify a potential surface segregation of Pd. We present the changes occurring in the core levels and VBs and compare these to the findings for pure metal and alloys foils.

Table 6.3: Deposition parameters and layer thickness of Cu thin films on Pd

deposition	flux rate/nA	deposition time	layer thickness/nm
1	29.6	10 min	0.3
2	29.9	10 min	0.9
3	29.9	10 min	1.6
4	30.1	10 min	2.4
5	29.9	30 min	4.6
6	30.3	60 min	7.7

Cu was deposited on a sputter-cleaned Pd foil substrate using the deposition parameters given in Table 6.3. The layer thickness was calculated as described in detail in Section 6.1, using the attenuation of the Pd $3d_{5/2}$ core level (E_{kin}=1151.5 eV, λ=1.55 nm [32]). The step-wise deposition of Cu on Pd can be followed by the increasing Cu 2p core-level and Auger line (Cu LMM) intensities displayed in the XPS survey spectra in Fig. 6.10.
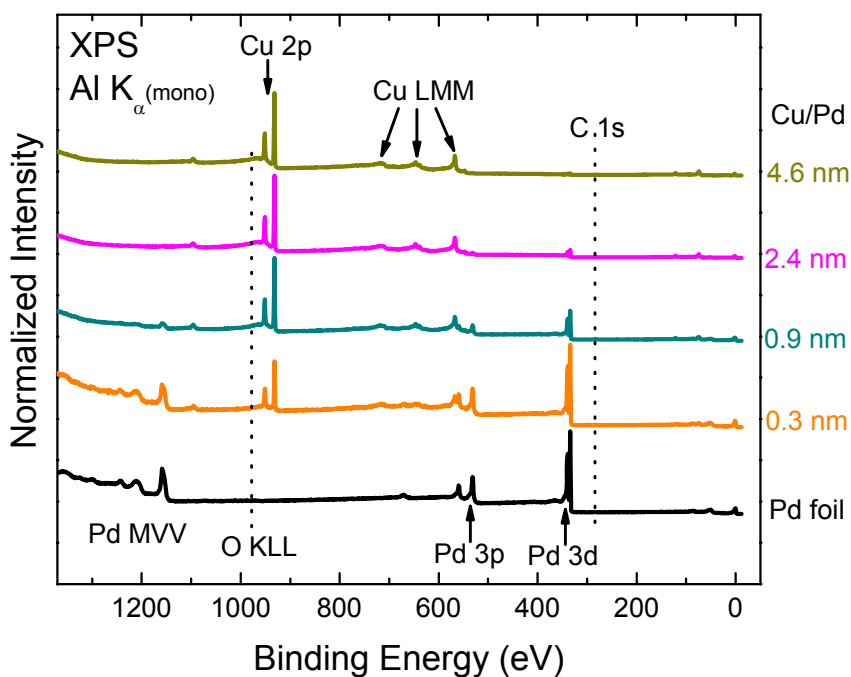
Fig. 6.10: XPS survey spectra taken after various Cu deposition steps onto a sputter-cleaned Pd foil.

While the Cu PES signal increases, the intensity of the Pd 3d core level and Pd MVV Auger lines decrease due to the attenuation in the Cu overlayer. The dotted lines indicate the common binding energy positions of the C 1s and O 1s lines that, if present, would indicate surface contamination.
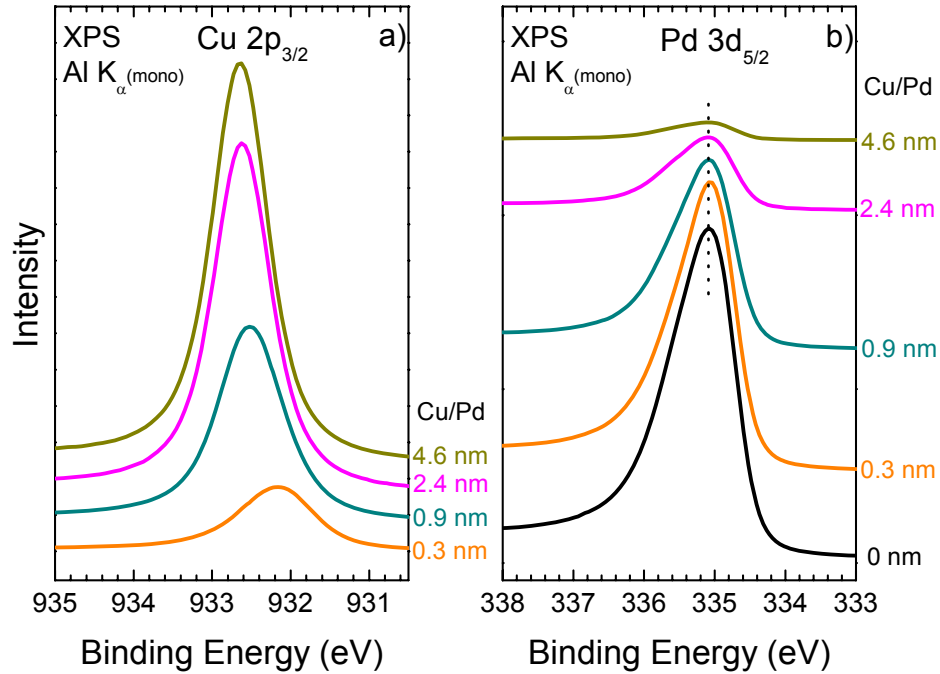
Fig. 6.11: a) Cu $2p_{3/2}$ and b) Pd $3d_{5/2}$ core level as a function of Cu deposition on a sputter-cleaned Pd foil.

Similar (but reverse) to Section 6.1, where we studied Pd growth on a Cu substrate, the Cu core levels increase in intensity (Fig 6.11a) and the Pd core levels (Fig. 6.11b) exhibit an exponential decay of intensity with Cu layer thickness. Also, the Cu $2p_{3/2}$ is first found at lower binding energy (similar to the position for the Pd/Cu interface in the previous section) and then shifts to higher binding energy, i.e., to the value for metallic Cu, with increasing Cu deposition. Contrary to our previous results, the host (Pd) does not form a noticeable shoulder, representative of Pd atoms at the interface, nor does the peak shift more than the experimental error of $\pm$ 0.05 eV (see vertical line in Fig. 6.11b). We ascribe this finding to a combination of effects. First, we note that the kinetic energies for the Cu and Pd lines are quite different and lead to a more surface-sensitive information in the case of Cu. Second, we expect the Pd overlayer (in the previous

section) to exhibit a higher inelastic scattering probability (compared to the Cu overlayer) due to a higher DOS near the Fermi energy. Again, this would increase the surface/interface sensitivity of the Cu spectra in the Pd/Cu case. Finally, the potentially present additional shoulder of an interface species in the Pd spectrum of the Cu/Pd case would be expected in the asymmetric tail at higher binding energies. The expected increase in this tail might be counterbalanced by the expected intensity reduction due to reduced inelastic scattering in the Cu overlayer (compared to the Pd/Cu case). Thus, in summary, we believe that, based on the evidence of the Cu spectrum, an interfacial Pd-Cu bond is indeed formed and that, for the reason discussed above, the signature of this bond is suppressed in the Pd spectrum in Fig. 6.11b. Note that Cu was reported to grow in a pseudomorphic layer-by-layer mode on Pd for Cu/Pd(100) [100], Cu/Pd(110) [101, 102], and Cu/Pd(111) [103, 104].

The valence band spectra for the Cu/Pd deposition series are shown in Fig. 6.12a. Analogous (inverse) to the results in Section 6.1, the intensity between ~1.8 eV and E_F continuously decreases until the VB resembles that of pure Cu (Pd in Section 6.1). As displayed in Fig. 6.12b, it is again possible to describe the observed VBSs by superposition of pure Pd and Cu VBs with suitable weights. The differences between the experimental and calculated spectra are indicated by black solid lines in Fig. 6.12b and are quite small, indicating that there is no significant alloying occurring for Cu deposited on Pd at RT (apart from, possibly, at the interface).
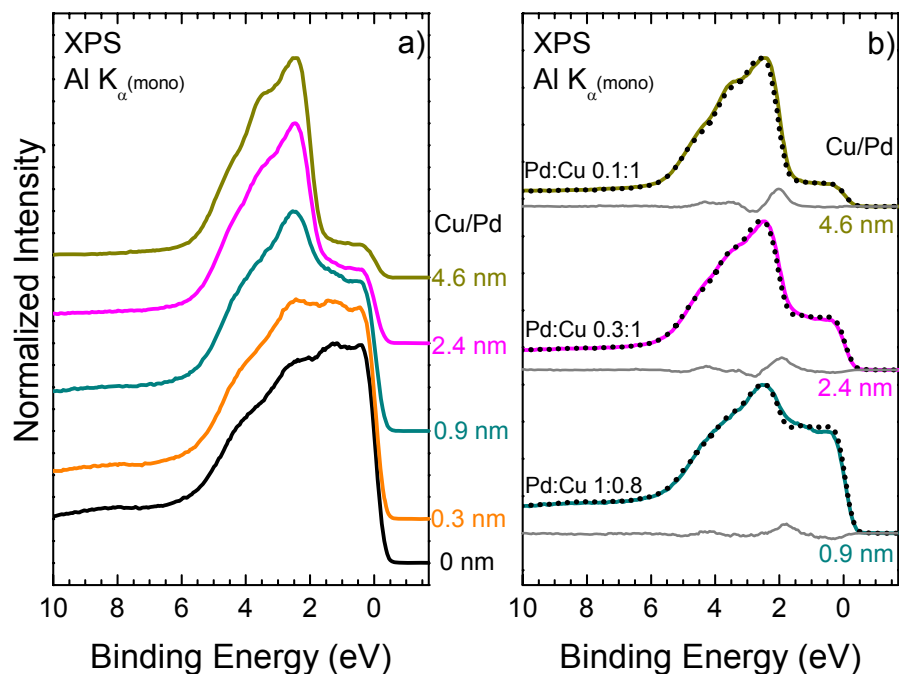
Fig. 6.12: a) Evolution of the VB with gradual deposition of Cu onto a sputter-cleaned Pd foil, and b) comparison of the experimental VBS with calculated superpositions of Pd and Cu reference spectra.

Section 6-4

Cu Deposition on Pd – Influence of Annealing

After the last deposition step, a 7.7 nm Cu/Pd sample was step-wise annealed under UHV at increasing temperatures to study alloy formation and potential surface segregation tendencies. For each annealing step, the temperature was ramped until the thermocouple set point given in Table 6.4 was reached and then held constant for the indicated amount of time. After annealing, samples were allowed to cool down to room temperature prior to XPS analysis.

Table 6.4 Annealing parameters of 7.7 nm Cu/Pd interface sample

annealing step	time at set point/min	set point/°C	sample temperature/°C
1	1.1	100	135 ± 50
2	1.1	200	270 ± 50
3	1.0	300	405 ± 50
4	1.3	400	535 ± 30
5	1.1	500	670 ± 30

Fig. 6.13 presents the evolution of the (a) Cu $2p_{3/2}$ and (b) Pd $3d_{5/2}$ core levels as a function of temperature, along with the corresponding nominal Cu layer thickness on Pd. While the Pd $3d_{5/2}$ line increases with temperature, the Cu $2p_{3/2}$ signal decreases until only trace amounts are detected at 670°C. Both core levels shift towards lower binding energies upon annealing.
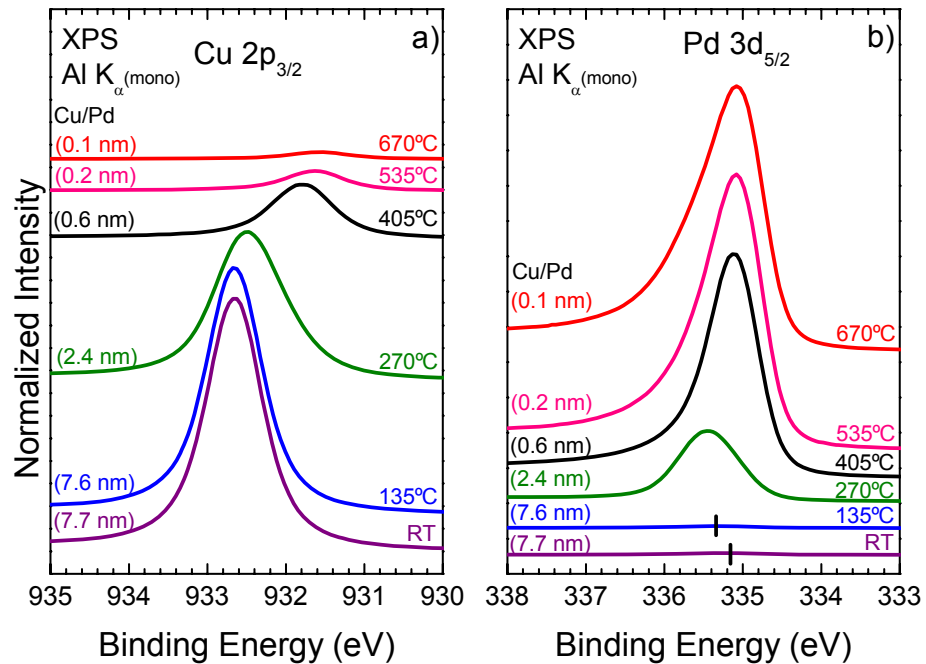
Fig. 6.13: a) Cu $2p_{3/2}$ and b) Pd $3d_{5/2}$ core level as a function of annealing temperature. The nominal Cu/Pd thicknesses are given in parentheses for reference.

The diminishing Cu signal with annealing temperature could be due to diffusion of Cu into the Pd bulk or Cu desorption. As in the case of Pd/Cu, the "desorption hypothesis" seems rather unlikely since the highest annealing temperature of 670°C is still far below the melting point of Cu at 1084.6 °C [55], and the vapor pressure of Cu (e.g., $1.53 \cdot 10^{-6}$ Pa at 1000 K (727 °C) [55]) is too low. Thermal desorption experiments in [103] detected no desorption of Cu thin films deposited on Pd(111) and attribute the loss of Cu intensity to diffusion into the bulk of Pd.

Consistent with the previous findings for the Pd/Cu system and the alloy formation at higher annealing temperatures, the large shift observed for the Cu $2p_{3/2}$ line to lower binding energies is interpreted as an increasing relative contribution of Cu atoms in a Pd-rich environment.

Analyzing the employed temperatures, we find that the onset of Cu in-diffusion for the Cu/Pd system requires a temperature between 135 °C and 270 °C. For Cu thin films on Pd(111), a minimum temperature of 177 °C (450 K) required for alloying was reported [103]. Due to the permeation of Cu into the bulk, the Pd 3d intensity shown in Fig. 6.13b rises continuously with temperature. We find the Pd peaks to first shift towards higher binding energy (during the alloy formation) and then back towards lower binding energies, approaching the binding energy value of metal Pd at 405 °C as the concentration of Cu atoms in the alloy decreases.
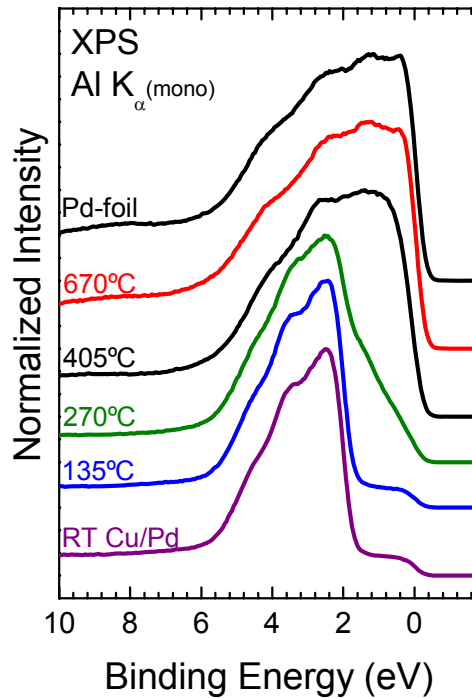
Fig. 6.14: Valence band spectra of a Cu/Pd interface sample as a function of annealing temperature.

Finally, the valence band spectra of the Cu/Pd annealing series are shown in Fig. 6.14. At 135 °C, the VB looks identical to the one at RT because the temperature threshold for alloying is not yet reached. After annealing at 270 °C, Cu atoms have diffused into the bulk and have created a Cu-dominated VB that, again, cannot be described by a simple superposition of Pd and Cu VB spectra.

Further annealing at 405 °C and 670 °C leads to a depletion of Cu within the first few surface layers. Thus, the VB becomes very similar to the VB of metallic Pd (at 405 °C and above), albeit with slightly reduced spectral weight near the Fermi energy (presumably due to some residual alloy contribution). In summary, this shows that a threshold temperature exists for the Cu/Pd interface system upon which alloying sets it. Already at room temperature, we find evidence for an alloy-like character directly at the

interface, but the vast majority of Cu overlayer atoms is in a metallic until the alloying threshold is reached. Once sufficient thermal energy is available, Cu diffuses into the Pd bulk, forming an alloy with decreasing Cu concentration as the annealing temperature is increased.

Further experiments would be necessary to pinpoint the exact temperature upon which Cu atoms diffuse into the Pd bulk. Through deliberate control of the annealing temperature, the diffusion depth and therefore the resulting alloy VBS of the surface-near layers partaking in catalysis could be tailored. This way, a Pd-Cu alloy surface layer with controlled Cu content could be formed. Since Pd is one of the catalytic materials with the highest stability in acidic conditions, Pd surface layers of a Pd-Cu thin-film system should exhibit a comparable stability in acid, and thus a Pd-enriched surface should be beneficial for the overall stability of the catalyst, in particular against leaching of Cu atoms.

Section 6-5

Summary and Conclusions

In this chapter, the growth and annealing behavior of Pd/Cu and Cu/Pd thin film interfaces was studied. In both cases, the valence bands observed after room temperature deposition can be described well by superimposed spectra of Pd and Cu reference metal valence bands, while only small contributions from alloy-like bonds at the interface are found. The subsequent annealing study revealed that alloy formation takes place only upon reaching a threshold temperature. Once the temperature barrier is overcome, the adlayer atoms diffuse into the bulk, forming a unique VB structure that cannot be

94

explained by a simple superposition of the metal Pd and Cu VBs. The fact that the creation of a surface alloy is independent of the deposition order (i.e., whether the Pd/Cu or Cu/Pd system is studied), suggests that it is not energetically favorable to form a segregated layer of one component only, but that rather alloy formation is preferred. This is most likely due to an entropy-related energy minimization, which overrides the thermodynamical considerations of total energy minimization for segregated systems.

Further experiments are required to precisely quantify the onset temperature of alloying for the two systems, in particular whether it depends on the deposition order. In the case of catalysts, a low onset temperature is preferred, since the nanoparticle size increases with annealing temperature (see Chapter VII). Our results indicate that, by deliberate control of the annealing temperature, the VBS of the surface layers can be taylored and optimized for the ORR in a fuel cell environment, focusing both on the electronic structure as well as the stability in electrolyte.

CHAPTER VII

NANOPARTICLE CATALYSTS

In this chapter the results of a detailed analysis of actual nanoparticle catalysts, synthesized by our collaborators at the Argonne National Lab (ANL), will be presented. The catalysts were prepared using three different processes that will be briefly described in Section 7.1. Due to the different synthesis routes and treatments performed, the electronic structure of the catalysts varies significantly. In Section 7.2, the electronic levels of selected catalysts are compared to the ones found in pure metals, alloys, bimetallic thin films, and commercial catalysts. The results indicate that alloying is as crucial for the ORR activity of catalysts as in the case of bulk alloys discussed in Chapter V. To ensure durability, catalysts need to be stable in the highly acidic environment found in proton exchange membrane fuel cells. In order to shed light on the degradation processes of the catalysts, a long-term acid-treatment study was performed. The results of this study are outlined in Section 7.3. Finally, a summary of the outcome of the experiments on nanoparticle catalysts is given in Section 7.4.

Section 7-1

Synthesis Methods and Properties

Pd/Cu nanoparticles were prepared at ANL using co-impregnation ("impreg.") [105] and colloidal techniques ("colloidal" or "coll." and "alternative colloidal" or "alt. coll.") [106]. In the colloidal technique, the metal precursors are dissolved in a solution containing a reducing agent and organic ligands which "cap" the metal nanoparticles as

they are formed; this prevents particle growth via agglomeration above a certain particle size [107]. The capped metal nanoparticles are then dispersed on a high-surface area carbon support (Cabot XC-72R) and the organic ligands are removed by annealing in a reducing gas (either 3.8% H_2 in He or pure H_2 was used). Details of the synthesis and treatment parameters of the catalyst are listed in Table 7.1.

Table 7.1: Parameters of investigated nanoparticle catalysts

sample	nom. ratio	state	XPS ratio	T_{anneal} °C	red. gas	mass act. mA/(mg Pd)	area act. μA/cm²	size nm
Alt. Coll.	Pd:Cu 1:3	UT	1:3.4	500	Regen	306	1420	3-10
Impreg.	Pd:Cu 1:1	UT	1:7.3	550	Regen	118	1281	21
Coll.	Pd:Cu 1:1	UT	1:1.4	500	H_2	756	1063	10
Coll.	Pd:Cu 1:1	AT	1:0.7	500	H_2	880	1076	11
Coll.	Pd:Cu 1:3	UT	1:5.1	500	H_2	592	796	7
Coll.	Pd:Cu 1:3	AT	1:0.4	500	H_2	247	396	9
Pd/C	Pd 1:0	UT	1	-	-	296		7
Pt/C	Pt 1:0	UT	1	-	-	1424	2396	2
Pt₃Co/C	Pt:Co 3:1	UT	1:2.7	-	-	1259	5010	N/A

(UT=untreated, AT=acid-treated, regen=3.8% H_2 in He)

An alternative colloidal technique was also used in which a viscosity modifier is used to control the diffusion and particle aggregation in the reducing medium. This modifier is used to enhance viscosity which leads to smaller particles, controlled size distribution and very well dispersed colloidal suspensions. In contrast, co-impregnated nanoparticles are prepared by mixing the metal precursors and by impregnation onto XC-72R without the use of capping agents [105]. It was found that co-impregnated nanoparticles have a much larger particle size and wider particle size distribution compared to catalysts synthesized by the colloidal techniques [107]. Furthermore, colloidal nanoparticles show a higher level of atomic-level mixing of the alloy constituent precursors prior to the reduction step

[105]. This is supported by studies on the effect of annealing temperature on the crystal structure, which find that alloying of Pd and Cu sets in at lower temperatures and is more complete for samples synthesized by the colloidal techniques [14, 105, 107].

In these studies, x-ray diffraction (XRD) was used to monitor the degree of alloying by evaluating the change in lattice constant with annealing temperature. In particular, the linear decrease of the lattice constant with increasing Cu content can be used as evidence that a Pd-Cu solid solution has formed [105]. Especially at higher Cu concentrations, the lattice constant of the impregnated samples deviates significantly from the lattice constant expected for an alloy with a certain copper content, indicating the presence of unalloyed (pure) Cu phases. In Section 7.2 we will demonstrate that the valence band (VB) spectrum of an impregnated catalyst can be well described by a superposition of the pure Pd and Cu VB spectra, supporting the view that the sample is primarily a mixture of pure (unalloyed) phases. In contrast, all samples synthesized by the colloidal techniques exhibited alloy-like VB spectra (i.e., spectra that could not be explained by a simple superposition). The investigation of real-life samples is a very important complement to the study of model systems, because findings can be directly applied to the production process. Nevertheless it also imposes a significant challenge on the analysis as the samples themselves are not well defined. Stemming from a wet-chemical process, we expect contamination, e.g., adsorption or precipitation of carbon and oxygen species on (to) the surface of the catalysts that potentially influence our results. Fig. 7.1 exemplarily shows the XPS survey spectrum of an alternative colloidal catalyst with a nominal Pd:Cu ratio of 1:3.
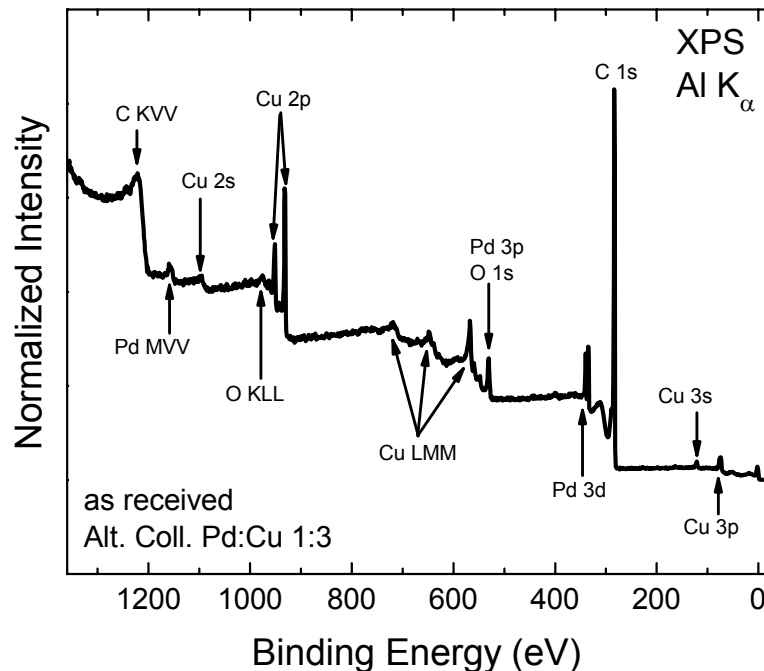
Fig. 7.1: Exemplary XPS survey spectrum of an as-received nanoparticle catalyst ("Alt. Coll." with a nominal Pd:Cu ratio of 1:3).

Due to the generally low metal loading (on the order of 10-20 weight percent), the signal from the carbon support (and, to a lesser degree, from carbon contaminations) dominates the spectrum. Additionally, a moderate amount of oxygen, probably due to exposure to residual amounts of oxygen during packing of the catalyst, is found on the surface of most samples. Please note that the O 1s signal in Fig. 7.1 is superimposed with the Pd $3p_{3/2}$ peak which has a similar binding energy value, so that the most direct evidence for the presence of oxygen is the O KLL Auger line. No other impurities were found for any of the catalyst samples described in this dissertation.

Post-treatment contamination by carbon and oxygen was minimized by packing the samples under inert conditions, as described in Chapter III.
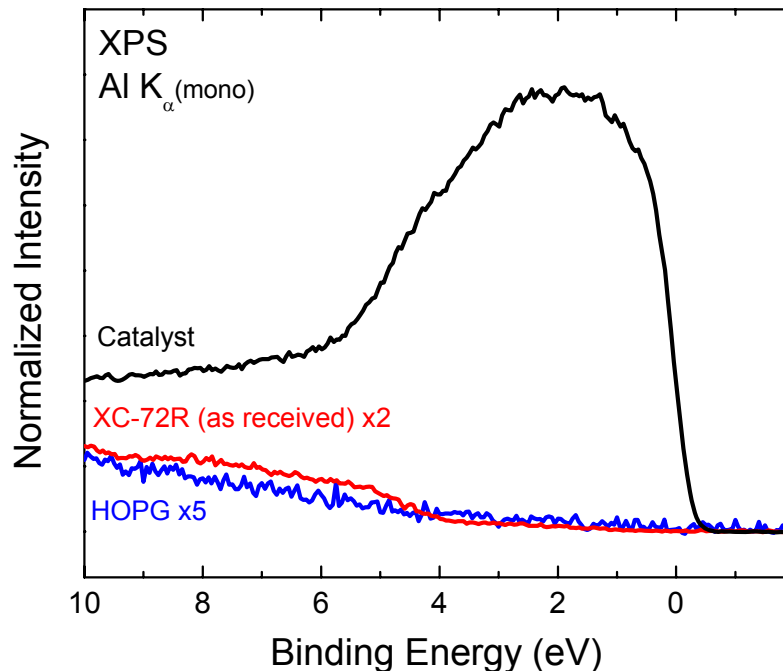
Fig. 7.2: XPS spectra showing a featureless and flat valence band region for the carbon support (XC-72R) and HOPG, as well as a typical catalyst (Pd/C) valence band spectrum.

In order to investigate a potential contribution of the carbon support to the valence band spectrum, the spectral valence band region of the carbon support (XC-72R) and (for comparison) of highly-ordered pyrolytic graphite (HOPG) was measured (see Fig. 7.2).

The VB spectrum of both samples is flat and featureless, with a slight increase at higher binding energies. Due to the lack of structure, a potential contribution to the VB of the nanoparticle catalysts is considered to be small, and will be removed by simple subtraction of the support reference spectrum. Table 7.1 summarizes the catalysts investigated in this Chapter and outlines their nominal composition ratio ("nom. ratio"), prior treatment ("state"), the elemental ratio as determined by XPS ("XPS ratio"), the temperature during annealing at ANL (T_{anneal}), the type of reducing gas used ("red. gas"), the mass activity ("mass act."), area activity ("area act."), and average particle size ("size") as determined by transmission electron microscopy (TEM).

100

In the following section we present the electronic structure of various nanoparticle catalysts and compare them to metal references, superposed valence band structures from deliberate addition of Pd and Cu VBs, alloys, and commercial catalysts.

Section 7-2

Electronic Structure of Pd-Cu Nanoparticle Catalysts

The electronic structure of catalysts prepared by the colloidal (Coll.), alternative colloidal (Alt. Coll.), and impregnation (Impreg.) technique are shown in Fig. 7.3.
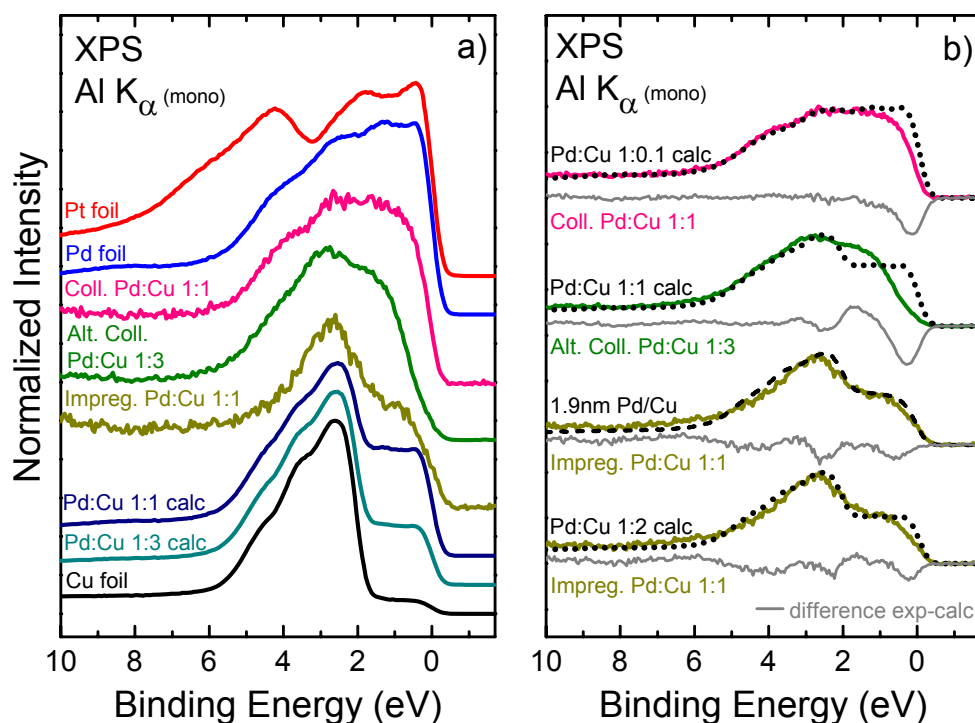
Fig. 7.3: a) Valence band spectra of nanoparticle catalysts, compared to metal foils and Pd:Cu 1:1 and 1:3 superpositions ("calc"), as well as b) superpositions with specifically chosen ratios (dotted lines) and Pd/Cu thin film (1.9 nm Pd/Cu) (dashed line) to fit the experimental curves (solid lines).

The valence bands of all catalysts exhibit a unique structure that clearly differs from the VB of their constituents Pd and Cu. The background of the catalyst spectra is consistently higher than those of clean metal references. This can be attributed to inelastic scattering of electrons in a surface contamination layer arising from the wet chemical process, which most likely covers a certain fraction of the metal surfaces with carbon species. Besides the above mentioned differences, the VB of the catalysts stays within the energy region (between ~5.5 eV and E_F) in which the Pd and Cu VB DOS is found. This finding agrees with our earlier results on the VB of alloy foils and bimetallic Pd-Cu thin film systems and shows that the chemical environment of the nanoparticles does not shift the DOS to higher binding energies as one would expect from theoretical predictions [27]. Additionally, some of the structural features found in the catalyst VBs reveal signs of contributions of the pure Pd and Cu VBs. For example, all three catalysts show a broad hump around 2.7 eV, which is energetically close to the main peak, and a shoulder due to the Cu 3d band at 2.5 eV and 2.8 eV (features 1 and 2 in Fig. 4.6) respectively, as well as a pronounced shoulder from the Pd VB at 2.4 eV (feature 3 in Fig. 4.5). The conservation of these contributions suggests that alloying does not lead to a pronounced redistribution of states for these regions. Close to E_F, the influence of the Pd VB dominates the catalyst spectra due to the lower intensity of the Cu spectrum in this regime.

Both colloidal catalysts exhibit more Pd-contribution to the VB than one would expect from a simple Pd:Cu 1:1 and 1:3 superposition of Pd and Cu reference spectra (see Pd:Cu (1:1) calc and Pd:Cu (1:3) calc in Fig. 7.3a. In contrast, the impregnated sample features a VB that resembles the calculated VBs. In order to test whether these observed spectral differences are due to different degrees of alloying (as described in Chapter VI),

we have tested, whether the catalyst VBs can be described by superpositions of the Pd and Cu VBs. As described for the annealing studies of Pd-Cu thin-films, an "alloyed VB structure" can most easily be distinguished from an "unalloyed VB structure" by evaluating the energy region between E_F and ~2.5 eV. A comparison of the catalyst samples to VBs created by specifically chosen ratios of Pd and Cu VBs in order to achieve the best fit to the experimental spectrum can be seen in Fig. 7.3b. For all catalyst samples in Fig. 7.3b, the background due to the influence of the support was removed by subtraction of the support VB presented in Fig. 7.2 (details of this procedure are described in Chapter III). In addition to the calculated VBs (dotted lines), the experimental spectrum of an unalloyed Pd/Cu thin-film system presented in Chapter VI is also included (dashed line). Furthermore, the difference between the experimental and the calculated VBs is displayed (gray lines). For the samples synthesized by colloidal techniques, various Pd and Cu VB ratios were tested but no satisfactory fit to the experimental spectrum could be achieved. In particular, the distinct variations close to E_F and around 1.7 eV demonstrate that the Pd and Cu contributions to the VB are not independent of each other and must therefore originate from a mixed Pd/Cu environment. In contrast, the impregnated sample, although annealed at a higher temperature than the colloidal samples (see Table 7.1), can be approximated fairly well by a Pd:Cu 1:2 superposition, which points towards an incompletely alloyed material. This view is further supported when comparing the VB of the impregnated sample to the VB of a Pd thin film deposited on Cu (dashed line in Fig. 7.3b), which resembles the nanoparticle VB very well. Thus, our XPS results support the results presented in [105] and [107] that found that higher annealing temperatures are required for the impregnated samples, and

103

that the alloying process is not as complete as compared to the nanoparticles synthesized by the colloidal techniques. All samples investigated presented here have been heat-treated at ANL at a temperature, duration, and reducing atmosphere that, for the particular synthesis method, has been empirically found to be the best compromise between activity and size. For all catalysts it was found that the particle size increases with increasing annealing temperature, thus reducing the available surface area for catalysis. At the same time, the degree of alloying increases with temperature, which is beneficial for the ORR activity [14, 105]. A minimum heat treatment temperature around 250 °C is needed in any case in order to completely reduce the metal precursors and for the colloidal catalysts to remove the organic capping agents used to restrict particle growth [105, 107]. In order to monitor the electronic changes occurring at the VB during annealing at various temperatures, future experiments could be conducted to heat-treat the as-synthesized catalysts in UHV and under partial hydrogen atmosphere in HV to more accurately correlate the electronic structure of a sample and its ORR activity. As many factors that cannot be distinguished unambiguously contribute to the ORR activity, we tentatively ascribe the low mass activity of the impregnated sample (see Table 7.1) to its incomplete formation of an alloy (with the associated consequences for the VB structure) and to its larger particle size (in particular the presence of "inactive" Pd atoms in the "bulk" of the nanoparticle that are included in the mass activity calculation).

The best-performing samples in terms of mass activity presented here are the colloidal samples with 1:1 and 1:3 Pd to Cu ratio. Although these samples exhibit a much larger particle size (about three times higher than a commercial Pt catalyst), their mass

and area activities reach approximately 50% of that of a commercial Pt catalyst and are about 2-3 times higher than those of a commercial Pd catalyst (see Table 7.1).

Fig. 7.4 compares the VB of the above-mentioned samples to the VB of metal and alloy foils investigated in Chapter IV and V.
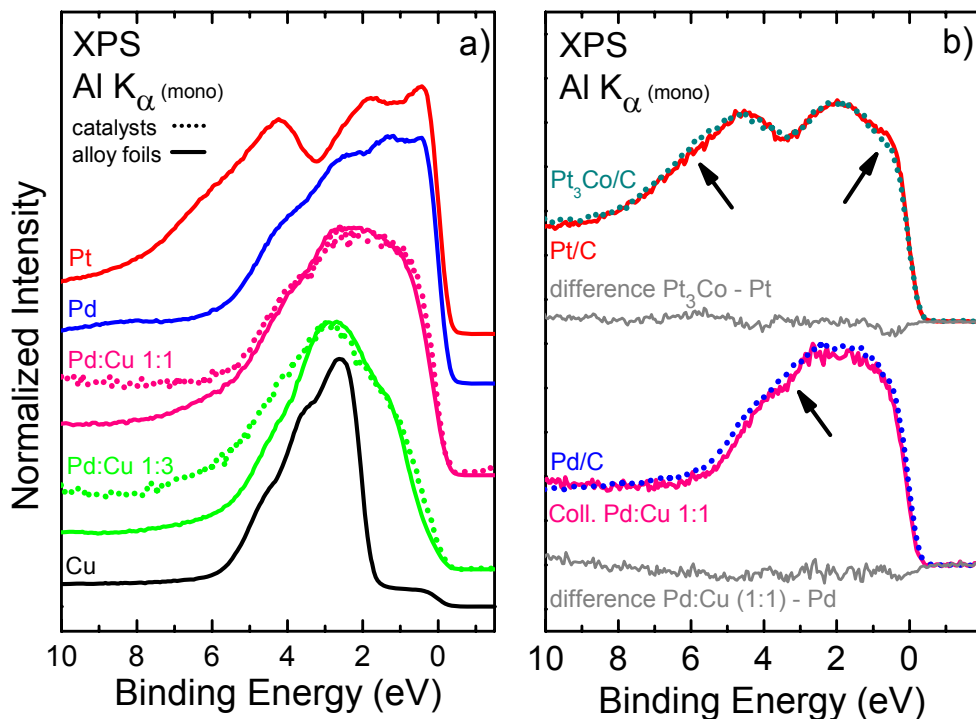
Fig. 7.4: a) XPS valence band structure of colloidal nanoparticles (dotted lines) and alloy foils (solid lines) with 1:1 and 1:3 Pd to Cu ratio, compared to metal references. b) Comparison of the VBs of Pt versus Pt_3Co (top) and Pd versus Pd:Cu 1:1 catalyst particles (bottom)

A clear trend towards an enhanced spectral weight near E_F with increasing Pd content can be seen. The VBs of the catalysts resemble those of the alloy foils of the same nominal composition, especially within the first 3 eV below E_F. This is corroborated by a study on supported small metal clusters by Mason, which found that the photoemission spectra of alloys and metal clusters dispersed on weakly interacting substrates (like

carbon) are virtually identical [108]. The observed similarities demonstrate that the electronic structure of real-life nanoparticle catalysts, might be correlated qualitatively to alloy and thin-film systems as long as nano-size effects are not dominant. In such a case the evolution of electronic structure could be studied more reliably as alloy foil and thin-film systems are much better defined (e.g., their configuration and morphology can be controlled more easily).

This demonstrates the need of model systems to search for the optimal electronic and crystal structures that lead to maximized ORR activity. One would then try to mimic the ideal conditions achieved for macroscopic systems and use the advantage of the high surface-to-bulk ratio of nanoparticles to maximize the available surface area and therefore the catalytic activity.

In Fig. 7.4b we compare the VBs of a pure Pt and Pd catalyst with that of a Pt/Co and a Pd/Cu nanoparticle catalyst. The Pt, Pd, and Pt_3Co catalysts are commercial samples, the Pd:Cu 1:1 catalyst is a colloidal catalyst synthesized by ANL. The most striking finding is that there is very little difference in the VBs of $Pt - Pt_3Co$ and $Pd - Pd:Cu$ 1:1. The difference spectra displayed as gray solid lines show only marginal differences for these samples (indicated by arrows in Fig. 7.4b), although their activity differs by a factor of 2 to 3 (see Table 7.1). In the following, possible influences are discussed that could lead to the seemingly uncorrelated relationship between the electronic structure and the ORR activity. For nanoparticle catalysts, many factors beyond the (optimized) electronic structure contribute to the ORR activity, since the here-employed spectroscopic techniques, albeit surface sensitive, probe a different volume than that involved in the catalytic activity. Furthermore, we note that our spectra are normalized to the maximum

in the spectral range of interest and thus do not present *absolute* quantitative information about the valence band density of states. In order to shed more light on understanding the electronic structure – ORR activity relationship, one promising approach is to first focus on the study of well-defined model systems. Furthermore, differential changes in the electronic structure before and after testing, can shed additional insights. In the following section, we thus turn our attention to durability tests performed under conditions relevant to the environment in a fuel cell, with primary focus on learning about the degradation behavior of Pd-Cu nanoparticles, but also to further understand the variations in the VB structure to correlate them with the decreased ORR activity after degradation.

Section 7-3

Stability in Acid – Influence of Acid-Treatment

In this section, we address a second important requirement for a PEMFC catalyst – stability under its highly acidic working environment (pH ~ -1 to 1 [109]). Among the catalytic materials, Pd is among those with the highest stability in strongly acidic conditions [25]. Cu, however, is more susceptible to acid, but can be partially stabilized by the formation of an alloy with Pd [36]. Nevertheless, it is expected that Cu, like any other non-noble base metal in a noble-base metal alloy, will be dissolved out of the alloy lattice over time [36].

In order to minimize degradation, a core-shell structure with the noble-metal catalyst forming a protective skin on the outer surface, is most desirable (see Chapter II).

However, no core-shell structure was found for any of catalysts studied in this dissertation. Bimetallic catalysts with a core-shell structure have been reported by Tao et al. [110] for rhodium-palladium (Rh-Pd) and platinum-palladium (Pt-Pd) nanoparticles.

To test the effects of prolonged exposure to acid, the two colloidal catalysts with nominal 1:1 and 1:3 Pd to Cu ratios (described in Section 7-2), were exposed to a 0.6M $HClO_4$ solution for three days. The most prominent effect for the 1:1 catalyst is a strong decline of the overall metal content from a total of about 4.8 % to about 1.0 % (see Table 7.2).
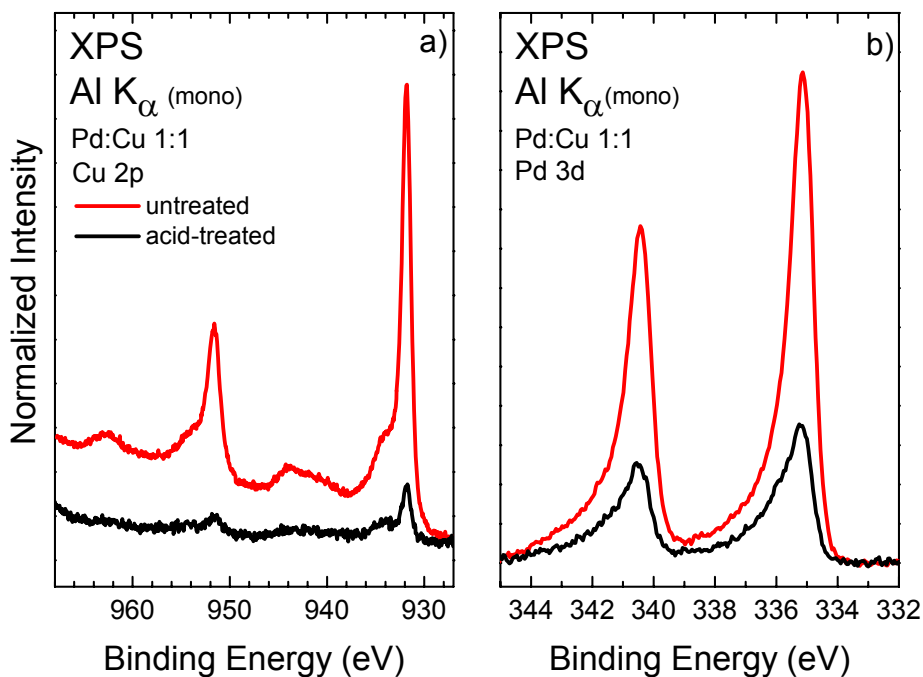
Fig. 7.5: a) Cu 2p and b) Pd 3d core level spectra of the Pd:Cu 1:1 colloidal catalyst before and after acid-treatment. Spectra are normalized to absolute intensity, such that the area under the peaks is directly proportional to elemental concentration.

This can be seen in Fig. 7.5, which presents the Cu 2p and Pd 3d core-level spectra, normalized to acquisition time. The intensities of the peaks are directly related to the

amount of metal atoms present and show that the Cu intensity is reduced more strongly as compared to Pd, presumably due to its lesser stability in acid. Table 7.2 furthermore quantifies this effect through the results of an elemental analysis: the acid treatment reduces the Pd to Cu ratio from initially 1:1.4 to 1:0.7.

Table 7.2: XPS-based elemental analysis of Pd:Cu 1:1 catalyst. All concentrations are given in at%

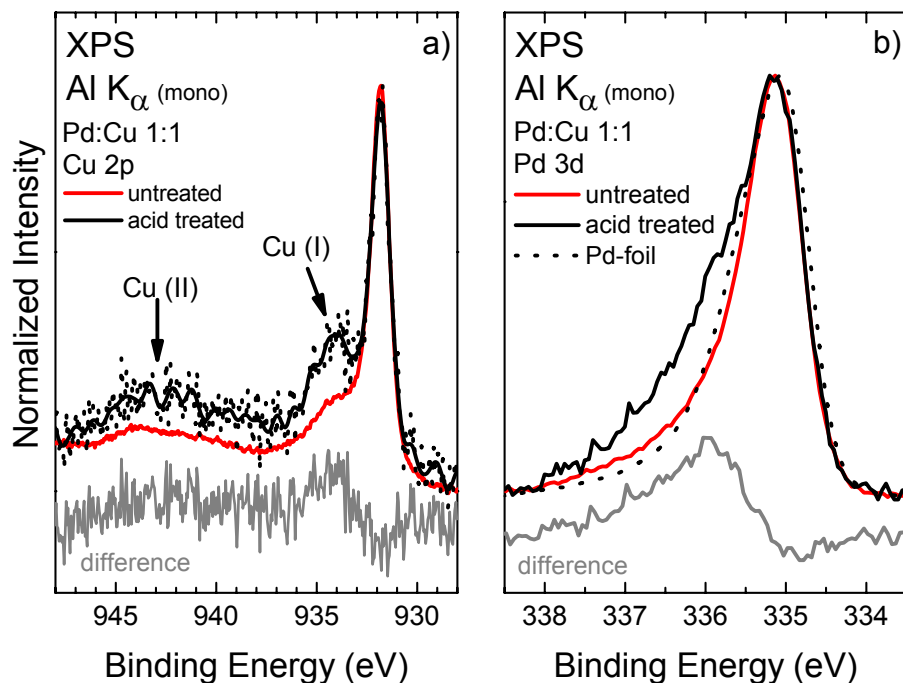| Pd:Cu 1:1	C	O	Cu	Pd	Pd to Cu ratio
untreated	85.8 ± 10.0	9.4 ± 10.0	2.8 ± 10.0	2.0 ± 10.0	1:1.4
acid-treated	88.1 ± 10.0	10.9 ± 10.0	0.4 ± 10.0	0.6 ± 10.0	1:0.7

Fig. 7.6: a) Cu 2p and b) Pd $3d_{5/2}$ core level spectra of the Pd:Cu 1:1 colloidal catalyst before and after acid-treatment. For Pd the difference spectrum (treated minus untreated) is also shown to illustrate the additional spectral contributions. The satellites marked with arrows in a) result from Cu atoms in +1 and +2 oxidation state.

The remainder of the metal particles exhibits an altered chemical environment after the treatment. To illustrate this, Fig. 7.6 shows the same Cu 2p and Pd $3d_{5/2}$ spectra, but normalized to the peak maximum. For both Pd an Cu, the difference spectrum bringing out the spectral differences is plotted in grey below the PES spectra.

Due to its low intensity, the Cu 2p spectrum in Fig. 7.6a (represented by black dots) was smoothed by a FFT-filter (Fast Fourier Transform) (solid line). We find a strong increase in the Cu satellite structures (particularly at ca. 934 and 943 eV), which are indicative of Cu in the +1 and +2 oxidation states (see arrows). We ascribe the change in oxidation state to Cu compounds formed through a reaction with the acid. The Pd $3d_{5/2}$ develops a pronounced shoulder on the high binding energy side, which is much larger than the asymmetric peak of metallic Pd and thus most likely indicates the formation of an oxidized species as well. In terms of peak positions, no significant shift was observed for the main peak of Cu or Pd (but, of course, for center of gravity of the entire line). This can be seen as an indication that the dominant chemical environment of the Pd/Cu solid solution does not change significantly.

The VBs of the colloidal Pd:Cu 1:1 catalyst before and after the stability test are displayed in Fig. 7.7. The lower spectra show the experimental data (after subtraction of the carbon support reference spectrum), while the upper spectra have additionally been smoothed by a 10-point adjacent averaging function.

The difference spectra (gray lines) show a small decline of intensity near E_F and an increase of intensity around 3.5 eV after the acid treatment. Most of the initial electronic valence structure, however, appears to have been preserved.
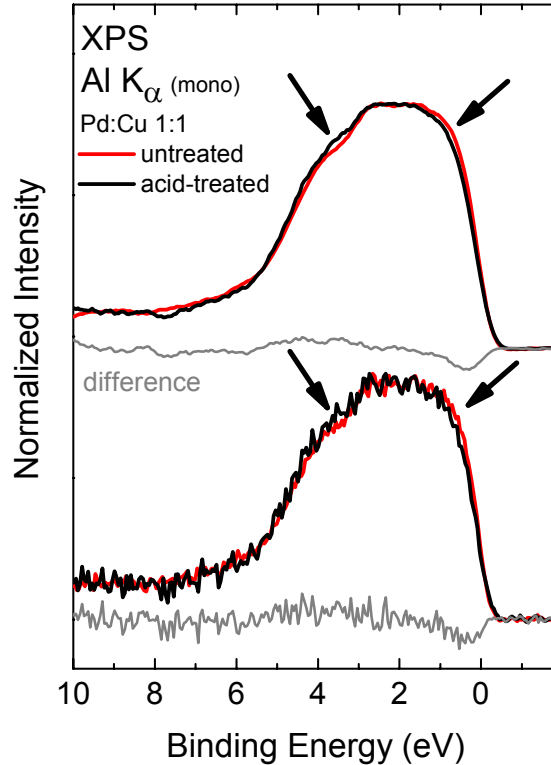
Fig. 7.7: Electronic valence structure of the colloidal Pd:Cu 1:1 catalyst before (red) and after (black) acid treatment. The spectra on the bottom represent the spectra as measured, while the top spectra were smoothed by a 10-point average. The difference spectra (treated minus untreated) are also shown.

Despite the huge loss in metal content, which could be due to dissolution of the metal particles from the support, the relatively unchanged VBs of the Pd:Cu 1:1 catalyst indicates that the local electronic environment of the remaining nanoparticle catalysts remains relatively unchanged under acidic conditions.

Similar to the 1:1 catalyst, the Pd:Cu 1:3 colloidal catalyst also experiences a substantial loss in metal content. Although the initial Cu content of the 1:3 catalyst is much higher than that of the 1:1 catalyst, the Cu signal after the acid treatment is barely visible (see the small peak at 931 eV in Fig. 7.8a. Apparently (and not unexpectedly), the stabilization of Cu is less pronounced in the 1:3 catalyst as compared to the 1:1 catalyst.

Fig. 7.8: a) Cu 2p and b) Pd 3d core levels of the Pd:Cu 1:3 colloidal catalyst before and after acid-treatment. The spectra were normalized to show their absolute intensity.

Furthermore, unalloyed Cu is found for the 1:3 catalyst using XRD, which is removed by the acid since it is not stabilized [14]. The absolute decline of the Pd signal of the 1:3 sample is also more pronounced than for the 1:1 sample. Expressed in numbers, the overall metal content diminishes from initially 14.5% to about 0.4%. After the treatment, almost all Cu has vanished (99% loss), and Pd has experienced a loss of 87.5%. The absolute elemental concentrations, derived from an elemental analysis of the samples are given in Table 7.3.

Table 7.3: XPS-based elemental analysis of Pd:Cu 1:3 catalyst. All concentrations are given in at%.

Pd:Cu 1:3	C	O	Cu	Pd	Pd to Cu ratio
untreated	69.9 ± 10	15.6 ± 10	12.1 ± 10	2.4 ± 10	1:5.1
acid-treated	86.3 ± 10	13.2 ± 10	0.1 ± 10	0.3 ± 10	1:0.4

Fig. 7.9a shows the Cu 2p spectrum (the original data is represented by dots) smoothed by a FFT-filter (Fast Fourier Transform) (solid line). Similar to the 1:1 sample, the Cu satellite structures (indicative of Cu +1 and +2) increase due to the acid treatment. The Pd $3d_{5/2}$ exhibits a 0.43 eV shift of the Pd $3d_{5/2}$ level to higher binding energies after the treatment, in agreement with the evolution of a high-binding energy shoulder in the case of the 1:1 sample.
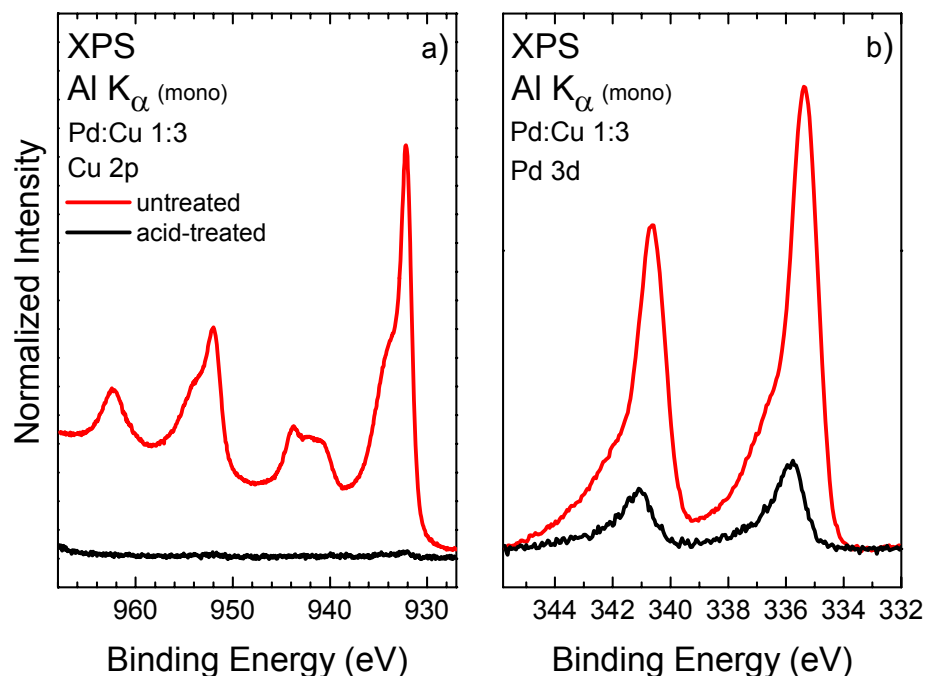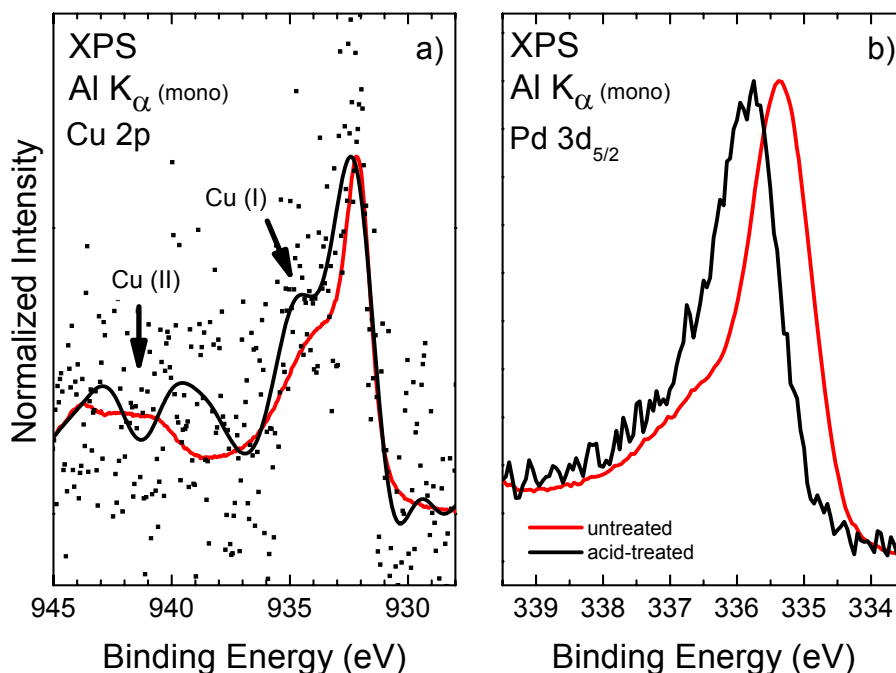

Fig. 7.9: a) Cu 2p and b) Pd $3d_{5/2}$ core level spectra of the Pd:Cu 1:3 colloidal catalyst before and after acid-treatment. Spectra were normalized to maximum count rate.

XRD results show that the Cu loss is accompanied by an increase of the lattice spacing. After the acid treatment, the average particle size increases, which leads to a variation of the local chemical environment of a large fraction of the Pd atoms. Furthermore, size-dependent effects (e.g., the screening of the photo-hole in the final state) might contribute.
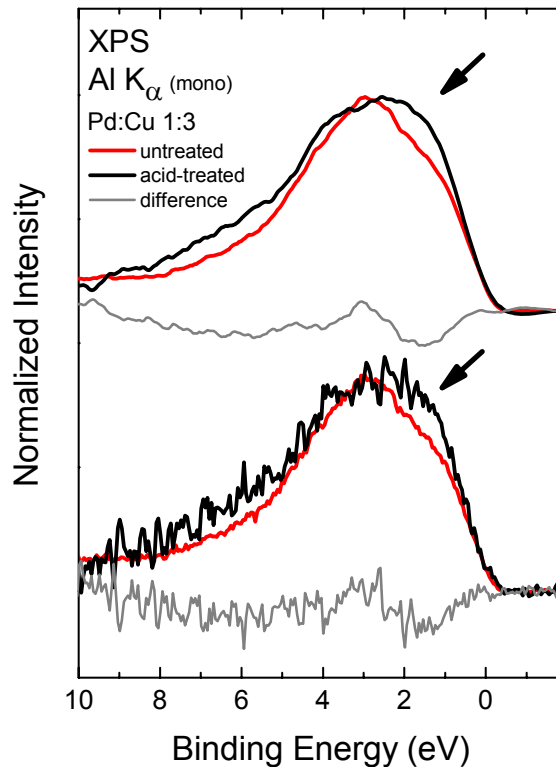
Fig. 7.10: Electronic valence structure of the Pd:Cu 1:3 catalysts before (red) and after (black) acid treatment. The curves on the bottom represent the spectra as measured, while the top spectra were smoothed by a 15-point average.

The VB spectra of the 1:3 catalyst before and after the acid treatment are shown in Fig. 7.10. The lower spectra show the experimental data (after subtraction of the support reference spectrum), while the upper spectra have additionally been smoothed by a 10- and 15-point adjacent averaging function for the untreated sample and treated sample, respectively.

Contrary to the relatively unchanged VB structure of the 1:1 sample (before and after treatment), the 1:3 catalyst shows a strong variation in spectral weight distribution, e.g., a significant increase of intensity between 0.7 and 2.7 eV (shown by the arrow in Fig. 7.10). As expected from the almost complete removal of Cu, the VB structure becomes

114

very Pd-like, indicating that the 1:3 catalyst is far more susceptible to degradation in acidic environments than the 1:1 catalyst.

Section 7-4

Summary and Conclusions

Pd-Cu nanoparticle catalysts prepared by various methods were analyzed by XPS. The valence band structure of the catalysts is found to be unique. Our results support the XRD-derived findings that alloying sets in at different temperatures depending on the synthesis route used. Furthermore, we can demonstrate that thin-film model systems behave similar to catalysts and can thus be used to help in the search for the optimal electronic structure for ORR. Stability in acidic environment was tested for a 1:1 and 1:3 Pd to Cu colloidal catalyst. Durability constitutes a major barrier for both catalysts as most of the metal content is found to be removed after the test. For the remaining nanoparticles, the VB of the 1:1 catalyst is almost preserved, while we find a strong modification towards a Pd-like VB of the 1:3 catalyst.

CHAPTER VIII

SUMMARY

Within the framework of this dissertation, the electronic structures of Pd-Cu bimetallic systems were studied. Besides the elucidation of the intrinsic electronic structure, particular focus lay on investigating the influence of annealing and acid-treatments. Furthermore, a first step towards the correlation of electronic structures with electrochemically determined activities was undertaken. Many factors like particle size, crystal structure, and the degree of alloying strongly influence the electronic structure and thus constitute a multidimensional parameter space that has to be investigated by a multitude of experimental methods for a detailed understanding of such systems. The large number of accessible parameters, especially in the case of nanoparticle catalysts, also constitutes a tremendous potential for Pd-Cu nanoparticles. In particular the tunability of the electronic structure and particle size through different synthesis methods and post-treatments, together with a potential cost advantage, make the Pd-Cu system a promising candidate to replace Pt as a catalyst.

The experiments presented in this study were geared towards the understanding and correlation of the electronic structure of pure metal foils, alloy foils, bimetallic thin-film systems, and bimetallic nanoparticles. It was shown that the best approach to study the ground state electronic structure is to use x-ray photoelectron spectroscopy (XPS) with monochromatized Al K_α radiation, as opposed to approaches using UV or soft x-ray excitation. This is due to a multitude of reasons, including because the fact that the excitation energy used in XPS is high enough to sample the entire Brillouin zone, and

that final state effects have less impact on such measurements. Furthermore, valence band structures determined with UV excitation are furthermore readily influenced by adsorbates and other surface contamination.

The XPS valence bands (VBs) of metals were compared to theoretical density of state calculations by our collaborators at Caltech. For Pt, Pd, and Cu, the d states make up almost the entire valence band, especially at the top of the band, which is the most catalytically active. The calculations furthermore demonstrate that a variation of photoionization cross-section with energy, differences in the transition matrix-element for various wave function symmetries, hybridization, and spin-orbit splitting influence the valence band structure measured by XPS. Therefore, these factors need to be considered for accurate analysis and comparison of VBs from experimental and theoretical studies.

When Pd and Cu atoms are randomly distributed over the lattice, as in the case of the disordered alloys, annealed bimetallic thin films, and colloidal catalysts, the electronic structure becomes unique and cannot be understood as a simple superposition of valence band structures of the pure metal references. In contrast, unheated Pd-Cu bimetallic films and incompletely alloyed nanoparticles can be well described by superposed spectra of Pd and Cu metal valence bands. For the bimetallic thin films and alloys, it was found that a threshold temperature exists at and above which alloying sets in. In the case of the nanoparticles, this temperature is furthermore dependent on the synthesis method used. In general, synthesis methods that require lower annealing temperatures are preferred, as the size of the nanoparticles increases with annealing temperature, leading to a decrease of active surface area.

Through electrochemical characterization at ANL, it was demonstrated that this symbiosis of the Pd and Cu valence band structures in alloys and nanoparticles leads to a significant increase in ORR activity as compared to pure Pd. Exposure of alloys and nanoparticles to a highly acidic environment, comparable to a real PEMFC environment, leads to leaching of both metals with a preferential release of Cu due to its lesser stability in acid. Durability is a major barrier for Pd-Cu catalysts, as most of the metal content of colloidal 1:1 and 1:3 catalysts was removed after the prolonged acid treatment. Analysis of the remaining nanoparticles showed that the VB of the 1:1 catalyst is almost preserved, while a strong shift towards a Pd-like VB was found for the 1:3 catalyst. The results demonstrate that particles with a 1:1 Pd:Cu ratio are more durable under a PEMFC working environment. In order to preserve the electronic structure, ways need to be found to minimize the overall metal loss and especially to stabilize the Cu in such acid environment.

Theoretical calculations that suggest that Pd will segregate on the nano-particle surface and form a pure Pd layer, thus protecting the nano-particle structure and composition, were also tested in this dissertation. No significant surface segregation of Pd (or Cu) was found experimentally upon annealing the alloy foils and bilayer systems at various temperatures. Likewise, no indications of a core-shell structure or surface segregation were found for the nanoparticles examined thus far. In contrast, we find that the annealing of bilayer systems leads to alloy formation, regardless of the specific substrate/overlayer choice (i.e., Pd/Cu or Cu/Pd).

These findings indicate that, by deliberate control of the annealing temperature, the VB of the surface layers can be adjusted so that it potentially becomes more suitable for

ORR. In the case of Cu deposited on Pd, Pd-enriched surface layers can be created by controlled diffusion of Cu into the Pd lattice. Such structure should exhibit a favorable stability in acid due to the protective Pd surface layer.

In this dissertation, it was demonstrated that the electronic structure of thin-film model systems behaves similar to the ones of nanoparticle catalysts. Thus, thin-film systems can be used as model systems to find the optimal electronic structure for ORR. This approach will be used in future experiments to guide the synthesis of nanoparticles and provide an even deeper understanding of their electronic structure, its dependency on annealing (and the annealing environment), and finally its relationship to ORR activity. With improved ORR activity and stability in electrolyte, alternative nanocatalyst materials carry the promise to reduce costs and increase lifetimes of operating polymer electrolyte membrane fuel cells, thus making an important contribution to the global energy portfolio of the future.

BIBLIOGRAPHY

[1]   F. Barbir, *PEM Fuel Cells: Theory and Practice*, Academic Press, (2005).

[2]   W. Vielstich, A. Lamm, and H. A. Gasteiger, *Handbook of Fuel Cells: Fundamentals, Technology, Applications*, Wiley, (2003).

[3]   Ballard Power Systems Inc., Demonstration programs, http://www.ballard.com, (2009).

[4]   E. Carlson, P. Kopf, J. Sinha, S. Sriramulu, and Y. Yang, PEM Fuel Cell Cost Status, Fuel Cell Seminar, Palm Springs, CA, 2005, Abstract No. 392, (2005).

[5]   B. James and J. Kalinoski, Mass Production Cost Estimation for Direct H2 PEM Fuel Cell System for Automotive Applications, DOE Hydrogen Program Review, (2008).

[6]   J. W. Döbereiner, *Schweigg. J* **39,** 78 (1823).

[7]   G. B. Kauffman, *Platinum Metals Rev.* **43,** 122 (1999).

[8]   J. J. Berzelius, *Jahres-Bericht* **14,** 237 (1835).

[9]   W. Ostwald, *Phys. Z* **3,** 313 (1902).

[10]   G. Ertl, *Angew. Chem., Int. Ed.* **47,** 3524 (2008).

[11]   W. T. Grubb and L. W. Niedrach, *J. Electrochem. Soc.* **107,** 131 (1960).

[12]   L. J. Nuttall and J. F. McElroy, *Int. J. Hydrogen Energy* **8,** 609 (1983).

[13]   P. Costamagna and S. Srinivasan, *J. Power Sources* **102,** 242 (2001).

[14]   D. Myers, email correspondence, (2009).

[15]   U.S. Department of Energy, PEM Fuel Cell, http://www1.eere.energy.gov/hydrogenandfuelcells/fuelcells/fc_types.html, (2009).

[16]   S. Srinivasan, E. A. Ticianelli, C. R. Derouin, and A. Redondo, *J. Power Sources* **22,** 359 (1988).

[17]   I. D. Raistrick, Electrode assembly for use in a solid polymer electrolyte fuel cell, US Patent No. 4,876, 115, (1989).

[18]   E. A. Ticianelli, C. R. Derouin, and S. Srinivasan, *J. Electroanal. Chem.* **251,** 275 (1988).

[19]   M. S. Wilson, J. A. Valerio, and S. Gottesfeld, *Electrochim. Acta* **40,** 355 (1995).

[20]   V. Stamenkovic, T. J. Schmidt, P. N. Ross, and N. M. Markovic, *J. Phys. Chem. B* **106,** 11970 (2002).

[21]   P. Ross, New Electrocatalysts for fuel cells, DOE Hydrogen Program Review, (2004).

[22]   B. Hammer and J. K. Norskov, *Adv. Catal.* **45,** 71 (2000).

[23]   H. A. Gasteiger, S. S. Kocha, B. Sompalli, and F. T. Wagner, *Appl. Catal., B* **56,** 9 (2005).

[24]   B. S. Mun, M. Watanabe, M. Rossi, V. Stamenkovic, N. M. Markovic, and P. N. Ross, *J. Chem. Phys.* **123,** (2005).

[25]   A. J. Bard, R. Parsons, and J. Jordan, *Standard Potentials in Aqueous Solution*, International Union of Pure and Applied Chemists, New York, USA (1985).

[26]   D. K. Kinoshita, *Electrochemical Oxygen Technology*, Wiley-Interscience, (1992).

[27]   A. Ruban, B. Hammer, P. Stoltze, H. L. Skriver, and J. K. Norskov, *J. Mol. Catal. A: Chem.* **115,** 421 (1997).

[28] A. V. Ruban, H. L. Skriver, and J. K. Norskov, *Phys. Rev. B* **59,** 15990 (1999).

[29] S. Hüfner, *Photoelectron Spectroscopy*, Springer, (2003).

[30] D. Briggs, *Practical Surface Analysis: Auger and X-Ray Photoelectron Spectroscopy*, John Wiley & Sons Ltd, (1990).

[31] J. H. Scofield, *J. Electron Spectrosc. Relat. Phenom.* **8,** 129 (1976).

[32] S. Tanuma, C. J. Powell, and D. R. Penn, *Surf. Interface Anal.* **20,** 77 (1993).

[33] K. S. Birdi, *Scanning Probe Microscopes: Applications in Science and Technology*, CRC, (2003).

[34] E. Meyer, H. J. Hug, and R. Bennewitz, *Scanning Probe Microscopy: The Lab on a Tip*, Springer, (2003).

[35] P. T. Kissinger and W. R. Heineman, *J. Chem. Educ.* **60,** 702 (1983).

[36] D. Myers, Non-platinum Bimetallic Cathode Electrocatalysts, project proposal narrative, (2007).

[37] D. A. Shirley, J. Stohr, P. S. Wehner, R. S. Williams, and G. Apai, *Phys. Scr.* **16,** 398 (1977).

[38] J. Stohr, F. R. McFeely, G. Apai, P. S. Wehner, and D. A. Shirley, *Phys. Rev. B* **14,** 4431 (1976).

[39] P. J. Feibelman and D. E. Eastman, *Phys. Rev. B* **10,** 4932 (1974).

[40] G. K. Wertheim, D. N. Buchanan, N. V. Smith, and M. M. Traum, *Phys. Lett. A* **A 49,** 191 (1974).

[41] P. S. Wehner, J. Stohr, G. Apai, F. R. McFeely, R. S. Williams, and D. A. Shirley, *Phys. Rev. B* **14,** 2411 (1976).

[42] J. W. Cooper, *Phys. Rev. Lett.* **13,** 762 (1964).

[43] U. Fano and J. W. Cooper, *Rev. Mod. Phys.* **40,** 441 (1968).

[44] J. J. Yeh and I. Lindau, *Atom Data Nucl. Data* **32,** 1 (1985).

[45] J. W. Rabalais, T. P. Debies, J. L. Berkosky, J. T. J. Huang, and F. O. Ellison, *J. Chem. Phys.* **61,** 516 (1974).

[46] M. P. Seah and G. C. Smith, *Surf. Interface Anal.* **15,** 751 (1990).

[47] D. A. Shirley, *Phys. Rev. B* **5,** 4709 (1972).

[48] S. Tougaard and B. Jorgensen, *Surf. Sci.* **143,** 482 (1984).

[49] V. S. Sundaram, M. B. Demoraes, J. D. Rogers, and G. G. Kleiman, *J. Phys. F: Met. Phys* **11,** 1151 (1981).

[50] J. B. Miller, C. Matranga, and A. J. Gellman, *Surf. Sci.* **602,** 375 (2008).

[51] Omicron, *EFM3 - UHV evaporator - instruction manual*.

[52] J. Kuppers, H. Conrad, G. Ertl, and E. E. Latta, *Jpn. J. Appl. Phys.* 225 (1974).

[53] H. Conrad, G. Ertl, J. Kuppers, and E. E. Latta, *Faraday Discuss.* **58,** 116 (1974).

[54] T. Gustafsson, E. W. Plummer, D. E. Eastman, and J. L. Freeouf, *Solid State Commun.* **17,** 391 (1975).

[55] D. R. Lide, *CRC Handbook of Chemistry and Physics, 89th Edition*, CRC, (2008).

[56] R. M. Lambert and G. Pacchioni, *Chemisorption and Reactivity on Supported Clusters and Thin Films:: Towards an Understanding of Microscopic Processes in Catalysis (NATO Science Series E)*, Springer, (2007).

[57] J. K. Norskov, J. Rossmeisl, A. Logadottir, L. Lindqvist, J. R. Kitchin, T. Bligaard, and H. Jonsson, *J. Phys. Chem. B* **108,** 17886 (2004).

[58] G. Santarossa, A. Vargas, M. Iannuzzi, C. A. Pignedoli, D. Passerone, and A. Baiker, *J. Chem. Phys.* **129,** 234703 (2008).

[59] A. Kokalj and M. Causa, *J. Phys.: Condens. Matter* **11,** 7463 (1999).

[60] C. Heske, R. Treusch, F. J. Himpsel, S. Kakar, L. J. Terminello, H. J. Weyer, and E. L. Shirley, *Phys. Rev. B* **59,** 4680 (1999).

[61] L. Weinhardt, O. Fuchs, E. Umbach, C. Heske, A. Fleszar, W. Hanke, and J. D. Denlinger, *Phys. Rev. B* **75,** 165207 (2007).

[62] Y. Baer, P. F. Heden, J. Hedman, M. Klasson, C. Nordling, and K. Siegbahn, *Phys. Scr.* **1,** 55 (1970).

[63] J. M. Ziman, *The Physics of Metals: 1. Electrons*, Cambridge University Press, (1969).

[64] T. A. Clarke, I. D. Gay, and R. Mason, *Chem. Phys. Lett.* **27,** 172 (1974).

[65] Kowalczy.S, R. Pollak, D. A. Shirley, and L. Ley, *Phys. Lett. A* **A 41,** 455 (1972).

[66] B. V. Crist, *Handbook of Monochromatic XPS Spectra, The Elements of Native Oxides*, Wiley, (2000).

[67] N. E. Christensen, *J. Phys. F: Met. Phys* **8,** L51 (1978).

[68] N. V. Smith, G. K. Wertheim, S. Hufner, and M. M. Traum, *Phys. Rev. B* **10,** 3197 (1974).

[69] L. F. Mattheiss and R. E. Dietz, *Phys. Rev. B* **22,** 1663 (1980).

[70] O. K. Andersen, *Phys. Rev. B* **2,** 883 (1970).

[71] A. H. MacDonald, J. M. Daams, S. H. Vosko, and D. D. Koelling, *Phys. Rev. B* **23,** 6377 (1981).

[72] L. Weinhardt, Dissertation, Universität Würzburg (2005).

[73] S. Hüfner, G. K. Wertheim, and D. N. Buchanan, *Chem. Phys. Lett.* **24,** 527 (1974).

[74] S. Hüfner, G. K. Wertheim, and D. N. Buchanan, *Solid State Commun.* **14,** 1173 (1974).

[75] P. Legare, L. Hilaire, G. Maire, G. Krill, and A. Amamou, *Surf. Sci.* **107,** 533 (1981).

[76] D. Chandesris, G. Krill, G. Maire, J. Lecante, and Y. Petroff, *Solid State Commun.* **37,** 187 (1981).

[77] J. F. Janak, D. E. Eastman, and A. R. Williams, *Solid State Commun.* **8,** 271 (1970).

[78] V. V. Nemoshkalenko, M. G. Chudinov, V. G. Aleshin, Y. N. Kucherenko, and L. M. Sheludchenko, *Solid State Commun.* **16,** 755 (1975).

[79] S. Hüfner, G. K. Wertheim, M. M. Traum, and N. V. Smith, *Solid State Commun.* **11,** 323 (1972).

[80] V. V. Nemoshkalenko, V. G. Aleshin, Kucheren.Yn, and Sheludch.Lm, *Solid State Commun.* **15,** 1745 (1974).

[81] N. J. Shevchik, *Phys. Rev. B* **13,** 4217 (1976).

[82] H. Hochst, S. Hufner, and A. Goldmann, *Phys. Lett. A* **57,** 265 (1976).

[83] V. V. Nemoshkalenko, V. G. Aleshin, Y. N. Kucherenko, and L. M. Sheludchenko, *J. Electron Spectrosc. Relat. Phenom.* **6,** 145 (1975).

[84] L. Hodges, H. Ehrenreich, and N. D. Lang, *Phys. Rev.* **152,** 505 (1966).

[85] P. Steiner, S. Hufner, A. J. Freeman, and D. S. Wang, *Solid State Commun.* **44,** 619 (1982).

[86] H. Conrad, G. Ertl, J. Küppers, and E. E. Latta, *Surf. Sci.* **65,** 245 (1977).

[87] K. Y. Yu, W. E. Spicer, I. Lindau, P. Pianetta, and S. F. Lin, *Surf. Sci.* **57,** 157 (1976).

[88] W. Pfeiler, *Alloy Physics: A Comprehensive Reference*, Wiley-VCH, (2007).

[89] R. W. Cahn, *The Coming of Materials Science, Volume 5*, Pergamon, (2001).

[90] ACI alloys Inc, http://www.acialloys.com/, (2009).

[91] N. Martensson, R. Nyholm, H. Calen, J. Hedman, and B. Johansson, *Phys. Rev. B* **24,** 1725 (1981).

[92] Z. W. Lu, S. H. Wei, and A. Zunger, *Phys. Rev. B* **45,** 10314 (1992).

[93] H. Winter, P. J. Durham, W. M. Temmerman, and G. M. Stocks, *Phys. Rev. B* **33,** 2370 (1986).

[94] S. Hüfner, G. K. Wertheim, and J. H. Wernick, *Solid State Commun.* **17,** 417 (1975).

[95] N. J. Shevchik, *Phys. Rev. Lett.* **33,** 1336 (1974).

[96] P. R. Subramanian, *J. Phase Equilibria* **12,** 231 (1991).

[97] K. Christmann, *Thin Solid Films* **46,** 249 (1977).

[98] C. J. Powell and A. Jablonski, *J. Phys. Chem. Ref. Data* **28,** 19 (1999).

[99] A. B. Aaen, E. Laegsgaard, A. V. Ruban, and I. Stensgaard, *Surf. Sci.* **408,** 43 (1998).

[100] E. Hahn, E. Kampshoff, N. Walchli, and K. Kern, *Phys. Rev. Lett.* **74,** 1803 (1995).

[101] C. Barnes and M. Gleeson, *Surf. Sci.* **319,** 157 (1994).

[102] E. Hahn, E. Kampshoff, A. Fricke, J. P. Bucher, and K. Kern, *Surf. Sci.* **319,** 277 (1994).

[103] G. Liu, T. P. St Clair, and D. W. Goodman, *J. Phys. Chem. B* **103,** 8578 (1999).

[104] B. Oral, R. Kothari, and R. W. Vook, *J. Vac. Sci. Technol., A* **7,** 2020 (1989).

[105] X. P. Wang, N. Kariuki, J. T. Vaughey, J. Goodpaster, R. Kumar, and D. J. Myers, *J. Electrochem. Soc.* **155,** B602 (2008).

[106] H. Bonnemann and R. M. Richards, *Eur. J. Inorg. Chem.* 2455 (2001).

[107] X. Wang, N. Kariuki, S. Niyogi, M. C. Smith, D. J. Myers, T. Hofmann, Y. Zhang, M. Bar, and C. Heske, *ECS Trans.* **16,** 109 (2008).

[108] M. G. Mason, *Phys. Rev. B* **27,** 748 (1983).

[109] P. Zelenay, email correspondence, (2009).

[110] F. Tao, M. E. Grass, Y. Zhang, D. R. Butcher, J. R. Renzas, Z. Liu, J. Y. Chung, B. S. Mun, M. Salmeron, and G. A. Somorjai, *Science* **322,** 932 (2008).

VITA

Graduate College
University of Nevada, Las Vegas

Timo Hofmann

Degrees:
Diplom-Ingenieur Nanostrukturtechnik (2005), Universität Würzburg, Würzburg, Germany

Awards:
Nowak-Notre Dame Award (2007-2008), presented to the most outstanding graduate student for excellence in chemistry, given by the UNLV Department of Chemistry

Publications:
1. "Bimetallic Palladium-Base Metal Nanoparticle Oxygen Reduction Electrocatalysts", X. Wang, N.N. Kariuki, S. Niyogi, M. Smith, D.J. Myers, T. Hofmann, Y. Zhang, M. Bär, and C. Heske, Proceedings of the Electrochemical Society (ECS), 2008 Fall Meeting, Honolulu, HI. ECS Transactions 16, 109-119 (2008).
2. "SALSA - a soft x-ray spectroscopy endstation with a novel flow-through liquid cell", M. Blum, L. Weinhardt, O. Fuchs, M. Bär, Y. Zhang, M. Weigand, S. Krause, S. Pookpanratana, T. Hofmann, W. Yang, J. Denlinger, E. Umbach, and C. Heske, Rev. Sci. Instrum., in print.

Dissertation Title:
Spectroscopic Investigation of Pd-Cu Bimetallic Systems for PEM Fuel Cell Catalysts

Dissertation Examination Committee:
Chairperson, Clemens Heske, Dr. rer. nat.
Committee Member, Dennis Lindle, Ph.D.
Committee Member, Dong-Chan Lee, Ph.D.
Graduate Faculty Representative, Adam Simon, Ph.D.